UNIVERSITA' DELLA CALABRIA

Facoltà di Scienze Matematiche, Fisiche e Naturali

Dottorato di Ricerca in Fisica
XXIII Ciclo
(settore disciplinare Fis/04)

Search for a light U boson in $e^+e^- \to \mu^+\mu^-\gamma$ channel with the KLOE experiment at DAΦNE collider at LNF and application of the GEM technology for the KLOE-2 Inner Tracker

Dr. Gianfranco Morello

Supervisore
Prof. Marco Schioppa

Coordinatore
Prof. Giovanni Falcone

Tutors
Dr. Giovanni Bencivenni

Dr. Graziano Venanzoni

Anno Accademico 2009/2010

Dedicated to all the people who in these years patiently sustained me

Contents

Introduction

The KLOE experiment at Laboratori Nazionali di Frascati collected during the period 2002-2005 an integrated luminosity of $\int \mathcal{L}\ dt \sim 2.5\ fb^{-1}$ at the DAΦNE ϕ-factory, an e^+e^- collider operating at the centre-of-mass energy of 1020 MeV, corresponding to the mass of the ϕ meson. The experiment achieved several important results in kaon and hadronic physics. An upgrade of the KLOE apparatus with new subdetectors installed has been approved and KLOE-2 will start data taking at the beginning of 2011. The KLOE-2 physics program will focus on neutral kaon interferometry, study of the decays of K_S, η and η' and searches for exotics and new light gauge boson predicted in some extensions of the Standard Model.
In the first chapter the physics program of the neutral kaon interferometry is reported and it is introduced the motivation for a search of Dark Matter in KLOE and KLOE-2 experiments. This search has a simple signature (a muon pair with associated photon) that will be described at the end of the chapter.
The main features of the KLOE detector (Drift Chamber, Electromagnetic Calorimeter and Trigger System) will be given in the second chapter.
The KLOE-2 program will be introduced in the third chapter, focusing the attention on the new subdetectors to be installed and on their impact on the physics measurements.
The fourth chapter will be devoted to the GEM technology chosen to realize one of the new subdetectors of KLOE-2: the Inner Tracker. Here, the main advantages and features of this technology will be described in detail.
The measurements of detection efficiency and spatial resolution of the Inner Tracker prototype (GEM technology) will be reported in the fifth chapter. The end of this chapter will be centered on planar GEM study in magnetic field. The test chamber was equipped with the final IT readout system.
In the last chapter will be discussed in detail the analysis for the search of a light boson (U) in the $\mu\mu\gamma$ events and will be presented a deepened study to improve the background rejection mainly due to $\pi\pi\gamma$ events.

Introduzione

L'esperimento KLOE ai Laboratori Nazionali di Frascati ha accumulato una luminosità integrata di $\int \mathcal{L}\ dt \sim 2.5\ fb^{-1}$ (nel periodo 2002-2005) alla ϕ-factory DAΦNE, un acceleratore e^+e^- con energia nel centro di massa di 1020 MeV corrispondente alla massa del mesone ϕ. L'esperimento ha fornito molteplici misure di precisione nella fisica dei kaoni e degli adroni. Un upgrade del rivelatore KLOE con nuovi rivelatori è stato approvato e KLOE-2 inizierà la presa dati in pochi mesi (inizio del 2011). Il programma di fisica di KLOE-2 si focalizzerà sull'interferometria dei kaoni neutri, sugli studi dei decadimenti del K_S, η e η' e su un nuovo bosone di gauge previsto in alcune estensioni del Modello Standard.
Nel primo capitolo troviamo una sintesi della fisica dell'interferometria dei kaoni neutri e sono introdotte le ragioni per ricerche di Dark Matter a KLOE e KLOE-2. Questa ricerca ha una semplice segnatura (una coppia di muoni con fotone associato) che sarà descritta in dettaglio nell'ultima parte del capitolo.
La descrizione dell'apparato sperimentale KLOE sarà data nel secondo capitolo: le caratteristiche della Camera a Deriva, del Calorimetro e del sistema di Trigger saranno riportate.
Il programma KLOE-2 sarà introdotto nel terzo capitolo, con una descrizione dei nuovi rivelatori previsti nell'apparato. In particolare, l'inserimento di un Tracciatore Interno sarà presentato, oltre all'impatto sulle misure di fisica.
Nel quarto capitolo si discuterà della tecnologia (GEM) che è stata usata per realizzare il Tracciatore Interno. I principali vantaggi di questa tecnologia saranno spiegati, per finire con un breve sguardo sulle nuove tecniche in fase di sviluppo.
Il quinto capitolo si occuperà della contruzione del prototipo del Tracciatore Interno con la tecnologia GEM e delle misure fatte su di esso. La parte finale del capitolo sarà centrata sulla caratterizzazione del comportamento di una GEM planare in campo magnetico con il readout finale progettato per il TI.

Nell'ultimo capitolo si discuterà in dettaglio l'analisi per la ricerca di un bosone leggero (U) negli eventi $\mu\mu\gamma$ a sarà presentato un nuovo taglio che è stato sviluppato per migliorare la reiezione del fondo (principalmente eventi $\pi\pi\gamma$).

Chapter 1

Neutral Kaon Interferometry

1.1 Neutral Kaon system

A $\phi-$factory is a powerful tool to study the evolution of entangled kaons, decoherence and CPT violation effects. A neutral kaon system is generally described by a linear combination of $|K^0\rangle$ and $|\bar{K}^0\rangle$ [2], eigenstates of the strong interaction:

$$|K\left(t\right)\rangle = a\left(t\right)|K^0\rangle + b\left(t\right)|\bar{K}^0\rangle + \sum_j c_j\left(t\right)|f_j\rangle \tag{1.1}$$

where the f_js represent all the possible decay final states and the $a\left(t\right)$, $b\left(t\right)$ and $c\left(t\right)$ are time-dependent functions. In Wigner-Weisskopf approximation, the $a\left(t\right)$ and $b\left(t\right)$ obey the Schrödinger-like equation

$$i\frac{\partial}{\partial t}\begin{pmatrix} a\left(t\right) \\ b\left(t\right) \end{pmatrix} = \mathbf{H}\begin{pmatrix} a\left(t\right) \\ b\left(t\right) \end{pmatrix} \tag{1.2}$$

where the Hamiltonian $\mathbf{H}$ can be written as

$$\mathbf{H} = \begin{pmatrix} H_{11} & H_{12} \\ H_{21} & H_{22} \end{pmatrix} = M - i\Gamma = \begin{pmatrix} M_{11} & M_{12} \\ M_{21} & M_{22} \end{pmatrix} - i\begin{pmatrix} \Gamma_{11} & \Gamma_{12} \\ \Gamma_{21} & \Gamma_{22} \end{pmatrix} \tag{1.3}$$

with $\mathbf{M}$ and Γ Hermitian matrices with positive eigenvalues calles *mass* and *decay* matrices. The index 1 refers to K^0 instead the index 2 to the $\bar{K}^0$ (2). The true Hamiltonian is a sum of a term related to the strong and electromagnetic interactions (conserving strangeness) and a term describing weak interactions where strangeness is not conserved: $\mathcal{H} = \mathcal{H}_0 + \mathcal{H}_{wk}$ [1]. The

[1] $\mathcal{H}_0|K^0\rangle = M_0|K^0\rangle, \quad \mathcal{H}|\bar{K}^0\rangle = M_0|\bar{K}^0\rangle, \quad S|K^0\rangle = |K^0\rangle, \quad S|\bar{K}^0\rangle = -|\bar{K}^0\rangle$

relation between $\mathcal{H}_{wk}$ and $\mathbf{H}$ is

$$M_{ij} = M_0\delta_{ij} + \langle i|\mathcal{H}_{wk}|j\rangle + \mathcal{P}\sum_i\left(\frac{\langle i|\mathcal{H}_{wk}|f\rangle\langle f|\mathcal{H}_{wk}|j\rangle}{M_0 - E_f}\right) \quad (1.4)$$

$$\Gamma_{ij} = 2\pi\sum_f\langle i|\mathcal{H}_{wk}|f\rangle\langle f|\mathcal{H}_{wk}|j\rangle\delta\left(M_0 - E_f\right) \quad (1.5)$$

with $i, j = 1, 2$. $\mathcal{P}$ is the principal part and the states f correspond to virtual ($\mathbf{M}$) or real ($\mathbf{\Gamma}$) decay states. The matrix $\mathbf{H}$ has 8 real parameters, but under the assumption of CPT invariance we can write[2]

$$H_{11} = H_{end} \quad \text{for } CPT \text{ conservation,} \quad (1.6)$$

$$|H_{12}| = |H_{21}| \quad \text{for } T \text{ conservation,} \quad (1.7)$$

$$H_{11} = H_{22} \quad \text{and } |H_{12}| = |H_{21}| \text{ for } CP \text{ conservation.} \quad (1.8)$$

The eigenvalues are

$$\lambda_S = m_S - i\Gamma_S/2 \quad (1.9)$$

$$\lambda_L = m_L - i\Gamma_L/2 \quad (1.10)$$

which permit us to define

$$\Delta m = m_L - m_S \quad (1.11)$$

$$\Delta\Gamma = \Gamma_S - \Gamma_L > 0 \quad (1.12)$$

$$\tan\phi_{SW} = \frac{2\Delta m}{\Delta\Gamma} \quad (1.13)$$

where the last term is called *superweak* phase. The eigenstates of $\mathbf{H}$ are the short- and long-lived states, usually written as:

$$|K_S\rangle = \frac{1}{\sqrt{2\left(1 + |\epsilon_S|^2\right)}}[\left(1 + \epsilon_S\right)|K^0\rangle + \left(1 - \epsilon_S\right)|\bar{K}^0\rangle] \quad (1.14)$$

$$|K_L\rangle = \frac{1}{\sqrt{2\left(1 + |\epsilon_L|^2\right)}}[\left(1 + \epsilon_L\right)|K^0\rangle - \left(1 - \epsilon_L\right)|\bar{K}^0\rangle]. \quad (1.15)$$

with $\epsilon_{S,L}$ small complex parameter describing CP impurities in physical states. Defining

$$\bar{\epsilon} \equiv \left(\epsilon_S + \epsilon_L\right)/2, \qquad \delta \equiv \left(\epsilon_S - \epsilon_L\right)/2, \quad (1.16)$$

[2]If CP conservation is imposed, all the element of the matrix are invariant under the exchange of indices $1 \leftrightarrow 2$

we can express these terms in function of elements of **H** (ignoring negligible quadratic term):

$$\bar{\epsilon} = \frac{H_{12} - H_{21}}{2\left(\lambda_S - \lambda_L\right)} = \frac{-i\Im M_{12} - \frac{1}{2}\Im\Gamma_{12}}{\Delta m + i(\Delta\Gamma)/2} \tag{1.17}$$

$$\delta = \frac{H_{11} - H_{22}}{2\left(\lambda_S - \lambda_L\right)} = \frac{\frac{1}{2}\left(M_{22} - M_{11} - \frac{i}{2}\left(\Gamma_{22} - \Gamma_{11}\right)\right)}{\Delta m + i(\Delta\Gamma)/2}. \tag{1.18}$$

Since $\bar{\epsilon}$ is phase dependent, one can choose the phase such as $\arg(\Gamma_{12}) = 0$ or $\arg(\Gamma_{12}) \ll 1$. In this case we have

$$\frac{|H_{12}|^2 - |H_{21}|^2}{|H_{12}|^2 + |H_{21}|^2} \simeq 4\Re\bar{\epsilon} \tag{1.19}$$

1.2 Correlated kaons

If neutral kaons are produced in the decay of a neutral unflavored vector (i.e. ϕ with $J^{PC} = 1^{--}$), we have the strangeness zero cases:

$$\begin{array}{l} |K^0(+\vec{p})\rangle|\bar{K}^0(-\vec{p})\rangle \\ |\bar{K}^0(+\vec{p})\rangle|K^0(-\vec{p})\rangle \end{array} \tag{1.20}$$

where the momenta are specified in the decaying meson rest frame. If the kaon system has a well defined angular momentum L, it is an eigenstate of C with eigenvalue $(-1)^L$. Since in the decay of a vector meson we have $L = 1 (C = P = -1)$, the kaon state is antisymmetric:

$$|i\rangle = \frac{1}{\sqrt{2}}|K^0(+\vec{p})\rangle|\bar{K}^0(-\vec{p})\rangle - |\bar{K}^0(+\vec{p})\rangle|K^0(-\vec{p})\rangle \tag{1.21}$$

$$= \frac{N}{\sqrt{2}}|K_S(+\vec{p}\rangle|K_L(-\vec{p})\rangle - |K_L(+\vec{p})\rangle|K_S(-\vec{p})\rangle \tag{1.22}$$

with

$$N = \frac{\sqrt{\left(1 + |\epsilon_S|^2\right)\left(1 + |\epsilon_L|^2\right)}}{\left(1 - \epsilon_S\epsilon_L\right)} \simeq 1 \tag{1.23}$$

1.3 Kaon interferometry

This state is copiously produced at a $\phi-$factory in the reaction $e^+e^- \to \phi \to K^0\bar{K}^0$. The decay amplitude for this state into final states $f_{1,2}$ produced in

the $+\vec{p}$ and $-\vec{p}$ directions at the kaon proper times $t_{1,2}$ can be written as

$$\begin{aligned} A(f_1,t_1;f_2,t_2) &= \frac{N}{\sqrt{2}}\{\langle f_1|T|K_S(t_1)\rangle\langle f_2|T|K_L(t_2)\rangle \\ &\quad -\langle f_1|T|K_L(t_1)\rangle\langle f_2|T|K_S(t_2)\rangle\} \qquad (1.24) \\ &= \frac{N}{\sqrt{2}}\Big\{\langle f_1|T|K_S\rangle\langle f_2|T|K_L\rangle e^{-i\lambda_S t_1}e^{-i\lambda_L t_2} \\ &\quad -\langle f_1|T|K_L\rangle\langle f_2|T|K_S\rangle e^{-i\lambda_L t_1}e^{-i\lambda_S t_2}\Big\} \qquad (1.25) \end{aligned}$$

from which we can compute the double differential decay rate into final states f_1 and f_2 at proper times t_1 and t_2

$$\begin{aligned} I(f_1,t_1;f_2,t_2) = C_{12}\Big\{&|\eta_1|^2 e^{-\Gamma_L t_1-\Gamma_S t_2}+|\eta_2|^2 e^{-\Gamma_S t_1-\Gamma_L t_2} \\ &-2|\eta_1||\eta_2|e^{-\frac{\Gamma_S+\Gamma_L}{2}(t_1+t_2)}\cos\left[\Delta m\,(t_1-t_2)+\phi_2-\phi_1\right]\Big\} \qquad (1.26) \end{aligned}$$

with

$$\eta_i \equiv |\eta_i|e^{i\phi_i} = \frac{\langle f_i|T|K_L\rangle}{\langle f_i|T|K_S\rangle} \qquad (1.27)$$

$$C_{12} = \frac{|N|^2}{2}|\langle f_1|T|K_S\rangle\langle f_2|T|K_S\rangle|^2. \qquad (1.28)$$

After the integration in (t_1+t_2), at a fixed $\Delta t = t_1 - t_2$ we obtain

$$\begin{aligned} I(f_1,f_2;\Delta t\geq 0) = \frac{C_{12}}{\Gamma_S+\Gamma_L}\Big\{&|\eta_1|^2 e^{-\Gamma_L\Delta t}+|\eta_2|^2 e^{-\Gamma_s\Delta_t} \\ &-2|\eta_1||\eta_2|e^{-\frac{\Gamma_s+\Gamma_L}{2}\Delta t}\cos\left[\Delta m\Delta t+\phi_2-\phi_1\right]\Big\} \qquad (1.29) \end{aligned}$$

For $\Delta t \leq 0$, the substitutions $\Delta t \to |\Delta t|$ and $t_1 \to t_2$ must be applied. In 1.29 we have a time depending interference term that gives rise to a characteristic correlation between the two kaon decays. Choosing different final states, many parameters of the kaon system can be extracted.

1.3.1 The four π states

If we choose $f_1 = \pi^+\pi^-$ and $f_2 = 2\pi^0$, the η_i parameters are so defined:

$$\begin{aligned} \eta_{+-} &\equiv |\eta_{+-}|e^{i\phi_{+-}} = \epsilon+\epsilon' \\ \eta_{00} &\equiv |\eta_{00}|e^{i\phi_{00}} = \epsilon-2\epsilon' \qquad (1.30) \end{aligned}$$

deriving from

$$\epsilon = \bar{\epsilon} - \delta + i\frac{\Im A_0}{\Re A_0} + \frac{\Re B_0}{\Re A_0} \quad (1.31)$$

$$\epsilon' = \frac{1}{\sqrt{2}} e^{i(\delta_2-\delta_0)} \frac{\Re A_2}{\Re A_0} \left[i\left(\frac{\Im A_2}{\Re A_2} - \frac{\Im A_0}{\Re A_0}\right) + \left(\frac{\Re B_2}{\Re A_2} - \frac{\Re B_0}{\Re A_0}\right)\right] \quad (1.32)$$

and the decay amplitudes of K^0 and $\bar{K}^0$ into $\pi\pi$ final states of definite isospin $I = 0, 2$ are written as

$$\begin{aligned} \langle \pi\pi; I|T|K^0\rangle &= (A_I + B_I)\, e^{i\delta_I} \\ \langle \pi\pi; I|T|\bar{K}^0\rangle &= (A_I^* + B_I^*)\, e^{i\delta_I} \end{aligned} \quad (1.33)$$

with δ_I the $\pi\pi$ strong interaction phase shift for channel of total isospin I. In the case of $f_1 = f_2 = \pi^+\pi^-$ the shape of the distribution in eq. 1.29 is sensitive only to kinematical quantities Γ_S, Γ_L and Δm, as shown in Fig. 1.1(a).

1.3.2 Double semileptonic decays

The semileptonic decays can be parametrized as

$$\begin{aligned} \langle \pi^- l^+ \nu|T|K^0\rangle = a + b, \qquad \langle \pi^+ l^- \bar{\nu}|T|\bar{K}^0\rangle = a^* - b^* \\ \langle \pi^+ l^- \bar{\nu}|T|K^0\rangle = c + d, \qquad \langle \pi^- l^+ \nu|T|\bar{K}^0\rangle = c^* - d^* \end{aligned} \quad (1.34)$$

where a, b, c, d, are complex quantities with the following implications

- CPT invariance implies $b = d = 0$
- $\Delta S = \Delta Q$ implies $c = d = 0$
- T invariance implies $\Im a = \Im b = \Im c = \Im d = 0$
- CP invariance implies $\Im a = \Re b = \Im c = \Re d = 0$

then we can define three measurable parameters

$$y = -b/a, \quad x_+ = c^*/a, \quad x_- = -d^*/a \quad (1.35)$$

where $x_+(x_-)$ describes the violation of the $\Delta S = \Delta$ rule in CPT conserving (violating) decay amplitudes, while y parametrizes CPT violation for $\Delta S = \Delta Q$ transitions. In the case of $f_1 = \pi^- l^+ \nu$ and $f_2 = \pi^+ l^- \bar{\nu}$ we have the following η_i parameters

$$\begin{aligned} \eta_{l+} &\simeq 1 - 2\delta - 2x_+ - 2x_- \\ \eta_{l-} &\simeq -1 - 2\delta + 2x_+^* - 2x_-^* \end{aligned} \quad (1.36)$$

The decay intensity is shown in Fig. 1.1(b).

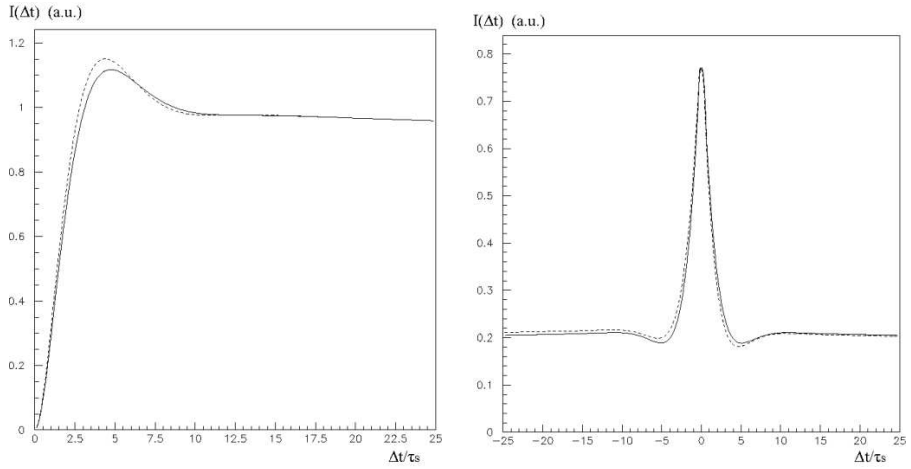

Figure 1.1: The $I(\pi^+\pi^-, \pi^+\pi^-; |\Delta t|)$ distribution as a function of $|\Delta t|$ (solid line) and the same distribution in the case of Δm + 10% (left). The $I(\pi^- l^+ \nu, \pi^+ l^- \bar{\nu}; \Delta t)$ distribution in the case of $\delta = x_+ = x_- = 0$ (solid line) and in the case $\Re\delta = 5 \cdot 10^{-4}, \Im\delta = 0.05, x_+ = x_- = 0$ (dashed line).

1.4 The entanglement of neutral kaons

As reported in 1.29, an interference term is present. A complete destructive interference makes the kaons not to decay into the same final state f at the same time t

$$I(f, t; f, t) = 0. \tag{1.37}$$

In this case the two kaons can be seen as free particles moving in opposite directions in the ϕ rest frame. But what really happens is that the behaviour of a meson depends on what the other kaon does. A direct mathematical way to describe this effect is to introduce a decoherence parameter ζ in the equation 1.29[3]

$$I(f_1, t_1; f_2, t_2; \zeta) = C_{12} \Big\{ |\eta_1|^2 e^{-\Gamma_L t_1 - \Gamma_S t_2} + |\eta_2|^2 e^{-\Gamma_S t_1 - \Gamma_L t_2}$$

[3]The decoherence parameter depends on the basis chosen to write the initial state. For a generic basis $|K_\alpha\rangle, |K_\beta\rangle$ we have

$$\begin{aligned} I(f_1, t_1; f_2, t_2; \zeta_{\alpha\beta}) \quad = \quad & \frac{|N'|^2}{2} \left\{ |\langle f_1|T|K_\alpha(t_1)\rangle\langle f_2|T|K_\beta(t_2)\rangle|^2 \right. \\ & + |\langle f_1|T|K_\beta(t_1)\rangle\langle f_2|T|K_\alpha(t_2)\rangle|^2 - 2\,(1 - \zeta_{\alpha\beta}) \\ & \left. \Re\left[\langle f_1|T|K_\beta(t_1)\rangle\langle f_2|T|K_\alpha(t_2)\rangle\langle f_1|T|K_\alpha(t_1)\rangle^*\langle f_2|T|K_\beta(t_2)\rangle^*\right] \right\} \end{aligned}$$

$$-2\left(1-\zeta\right)|\eta_1||\eta_2|e^{-\frac{(\Gamma_S+\Gamma_L)}{2}(t_1+t_2)}\cos\left[\Delta m\left(t_1-t_2\right)+\phi_2-\phi_1\right]\Big\} \quad (1.38)$$

If $\zeta = 0$ we are in the classical case (the *orthodox* quantum theory), while $\zeta = 1$ means total decoherence so the 1.26 can be written as (Furry's hypothesis):

$$\begin{aligned} I(f_1,t_1;f_2,t_2)_{Furry} &= \frac{|N|^2}{s}\Big\{|\langle f_1|T|K_S(t_1)\rangle\langle f_2|T|K_L/t_2)\rangle|^2 \\ &\quad +|\langle f_1|T|K_L(t_1)\rangle\langle f_2|T|K_S(t_2)\rangle|^2\Big\} \end{aligned} \quad (1.39)$$

A model which describes the decoherence mechanism can be introduced by a density matrix ρ that obeys a modified Liouville-von Neumann equation

$$\frac{d\rho}{dt} = -i\mathbf{H}\rho + i\rho\mathbf{H}^\dagger + i\delta\mathbf{H}'\rho \quad (1.40)$$

where $\mathbf{H}$ is the usual neutral kaon effective Hamiltonian and $\delta\mathbf{H}'$ induces deceherence in the system. If we describe the system in the orthonormal basis $|K_1\rangle = \frac{1}{\sqrt{2}}\left[|K^0\rangle + |\bar{K}^0\rangle\right]$ and $|K_2\rangle = \frac{1}{\sqrt{2}}\left[|K^0\rangle - |\bar{K}^0\rangle\right]$, the extra term can be written as a 4×4 matrix acting on ρ_μ

$$\delta\mathbf{H}'_{\mu\nu} = -2\begin{pmatrix} 0 & 0 & 0 & 0 \\ 0 & 0 & 0 & 0 \\ 0 & 0 & \alpha & \beta \\ 0 & 0 & \beta & \gamma \end{pmatrix} \quad (1.41)$$

where α, β and γ are real parameters which violate CPT symmetry and quantum mechanics, with the following requests: $\alpha, \gamma > 0$ and $\alpha\gamma > \beta^2$. The two parameters have mass dimension and are guessed to be at most $\mathcal{O}\left(m_K^2/M_{Planck}\right) \sim 2\cdot 10^{-20}\ GeV$. The formalism previously described is for single kaons. The assumption of complete positivity implies additional constraints on these parameters ($\alpha = \gamma$ and $\beta = 0$). According to some considerations on correlated kaon states, a loss of particle-antiparticle neutral kaon states can induce a breakdown of the correlation of state imposed by Bose statistics [5], [6]. The initial entangled state can be parametrized as

$$\begin{aligned} |i\rangle &= \frac{1}{\sqrt{2}}\Big\{\Big[|K^0\rangle|\bar{K}^0\rangle - |\bar{K}^0\rangle|K^0\rangle\Big] + \omega\Big[|K^0\rangle|\bar{K}^0\rangle + |\bar{K}^0\rangle|K^0\rangle\Big]\Big\} \\ &\propto \{[|K_S\rangle|K_L\rangle - |K_L\rangle|K_S\rangle] + \omega\left[|K_S\rangle|K_S\rangle - |K_L\rangle|K_L\rangle\right]\} \end{aligned} \quad (1.42)$$

with ω complex parameter describing a new CPT violation. The limit on this parameter is $|\omega| \sim \left[\frac{\left(m_K^2/M_{Planck}\right)}{\Delta\Gamma}\right]^{1/2} \sim 10^{-3}$ with $\Delta\Gamma = \Gamma_S - \Gamma_L$, so the best decay channel to have a look to such CPT violation is $f_1 = f_2 = \pi^+\pi^-$,

where the term CP violating are suppressed. A possible CPT violation can be given by spontaneous breaking of Lorentz symmetry. In the Standard Model Extension the CPT violation manifests by a parameter δ defined

$$\delta \approx i \sin\phi_{SW} e^{i\phi_{SW}} \gamma_K \left(\delta a_0 - \vec{\beta_K} \cdot \delta\vec{a}\right) / \delta m \tag{1.43}$$

where γ_K and β_K are the boost factor and velocity in the observer frame, and Δa_μ are four $CPT-$ and Lorentz-violating coefficients for the two valence quarks in the kaon.

1.5 Searches for Dark Matter in KLOE

Recent astrophyisical observations failed to find easy interpretations in terms of standard astrophysical and/or particle physics sources. A non exhaustive list of these observations includes the 511 keV gamma-ray signal from the galactic center observed by INTEGRAL satellite [8], the excess in the cosmic ray positrons (Fig. 1.2) reported by PAMELA [9], the total electron and positron flux measured by ATIC, Fermi and HESS and the annual modulation of the DAMA/LIBRA signal. These observations could suggest the existence of a WIMP (Weakly Interactive Massive Particle) dark matter particle belonging to a secluded gauge sector $U(1)_D$ under which the SM particles are uncharged. The abelian gauge field weakly interacts with the $U(1)_Y$ of the SM[4] by an invariant kinetic mixing term [7, 11]

$$\Delta\mathcal{L} = kF^{Y,\mu\nu}F_{D,\mu\nu} \tag{1.44}$$

The mixing parameter k is of the order of $10^{-4} - 10^{-2}$. The vector boson U has mass near the GeV scale. Annihilation of the Dark Matter (DM in the following) into the U boson, which decays into charged leptons and is light enough to kinematically forbid a decay that produces anti-protons, can explain the electron and/or positron excess (as observed by PAMELA experiment). The condition $m_U \ll m_{WIMP}$ implies an enhanced WIMP annihilation cross section in the galaxy. Moreover if the DM is charged under a non-abelian group, higgsed or confined near the GeV scale, its spectrum naturally implements an inelastic DM scenario, thereby explaining the annual modulation signal reported by DAMA/LIBRA. These hypothesis lead to the consequence that observable effects can be induced in $\mathcal{O}(GeV)$ energy e^+e^- colliders such DAΦNE or present and/or future B factories.

[4]This is true for any new Abelian gauge group $U(1)$.

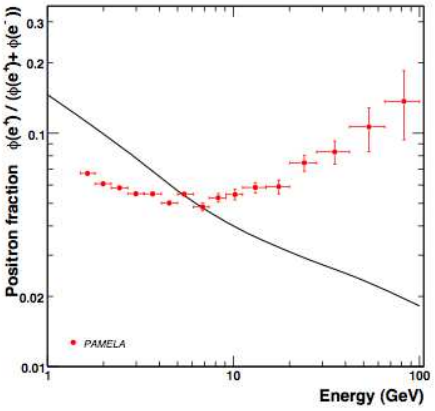

Figure 1.2: PAMELA positron fraction with theoretical models. The solid line shows a calculation by Moskalenko and Strong [10].

1.5.1 The Higgs sector of $U(1)_D$

A minimal implementation of the secluded $U(1)_D$ can be easily done adding a Higgs' field ϕ responsible for the sontaneous symmetry breaking. Assuming that all the additional particles (in particular the WIMP) are heavy with respect to the Higgs', we obtain [12]

$$\mathcal{L} = -\frac{1}{4}U_{\mu\nu}^2 - \frac{k}{2}F^{Y,\mu\nu}F_{D,\mu\nu} + |D_\mu\phi|^2 - V(\phi) \tag{1.45}$$

where $D_\mu = \partial_\mu + ie'U_\mu$ with $U(1)_D$ charge e'. The Higgs' potential is assumed to be of a form that spontaneously breaks the $U(1)_D$ symmetry: $V(\phi) = -\mu^2|\phi|^2 + \lambda|\phi|^4$. The vacuum expectation value of the Higgs' field is $\langle\phi\rangle = \nu'/\sqrt{2} = \sqrt{\mu^2/2\lambda}$. Expanding around this vacuum, $\phi = (\nu' + h')/\sqrt{2}$ we obtain

$$\mathcal{L} = -\frac{1}{4}U_{\mu\nu}^2 + \frac{1}{2}m_U^2U_\mu^2 + \frac{1}{2}\left(\partial_\mu h'\right)^2 - \frac{1}{2}m_{h'}^2h'^2 + \mathcal{L}_{int} \tag{1.46}$$

with $m_U = e'\nu'$ and $m_{h'} = \sqrt{s\lambda}\nu'$. The interaction terms are

$$\begin{aligned}\mathcal{L}_{int} \;=\; & \frac{k}{2}U_{\mu\nu}F^{\mu\nu} + \frac{m_U^2}{\nu'}h'U_\mu^2 + \frac{m_U^2}{\nu'^2}h'^2U_\mu^2 \\ & -\frac{m_{h'}^2}{2\nu'}h'^3 - \frac{m_{h'}^2}{8\nu'^2}h'^4\end{aligned} \tag{1.47}$$

The second term suggests the possibility for the U boson to produce Higgs-strahlung. The U and the h' can be seen at DAΦNE if their msses are

below 1020 MeV. The production cross-section scales as $1/s$ where s is the squared centre-of-mass energy. There are some scenarios with a confined secluded gauge group in which searches at DAΦNE are easier than at the B factories.

1.5.2 U-boson production

At e^+e^- colliders there are two important dark sector production modes: an off-shell U production which decays into a pair $X\bar{X}$ dark sector fields or the production of an on-shell U boson associated to a photon. For the off-shell production the cross-section is

$$\begin{aligned}\sigma_{\bar{X}X} &= N_c\frac{4\pi}{3}\frac{k^2\alpha\alpha_D}{E_{cm}^2}\left|1-\frac{m_U^2}{E_{cm}^2}-\frac{im_u\Gamma}{E_{cm}^2}\right|^{-2}\sum_{i=1}N_f q_i^2\sqrt{1-\frac{4m_{X_i}^2}{E_{cm}^2}}\left(1+\frac{2m_{X_i}}{E_{cm}^2}\right)\\ &\simeq 0.78\ fbN_c\left(\frac{k}{10^{-3}}\right)^2\left(\frac{\alpha_D}{\alpha}\right)\left(\frac{E_{cm}}{10.58\ GeV}\right)^{-2}\times N_f \qquad (1.48)\end{aligned}$$

where N_c is the number of colors in the dark sector gauge group, N_f is the number of dark sector particles X_i coupling to U with charges q_i while α_D is equal to $\frac{g_D^2}{4\pi}$ with g_D as U gauge coupling constant. This cross section is nonzero even for m_U much larger than E_{cm} as long as $m_X < E_{cm}/2$. The cross section of the on-shell U boson with a photon is

$$\frac{d\sigma_{U\gamma}}{d\cos\theta}=\frac{2\pi k^2\alpha^2}{E_{cm}^2}\left(1-\frac{m_U^2}{E_{cm}^2}\right)\frac{1+\cos^2\theta+\frac{4m_U^2/E_{cm}^2}{\left(1-m_U^2/E_{cm}^2\right)^2}}{(1+\cos\theta)(1-\cos\theta)} \qquad (1.49)$$

with a singularity as the photon becomes collinear with the initial-state electron or positron. Asking for $\cos\theta_{min} < \cos\theta < \cos\theta_{max}$ (geometrical acceptance of the photon) we have

$$\begin{aligned}\sigma &= \frac{2\pi k^2\alpha^2}{E_{cm}^2}\left(1-\frac{m_U^2}{E_{cm}^2}\right)\left[\left(1+\frac{2m_U^2/E_{cm}^2}{\left(1-m_U^2/E_{cm}^2\right)^2}\right)\Theta-\cos\theta_{max}+\cos\theta_{min}\right]\\ &\sim 2.4\ fb\left(\frac{k}{10^{-3}}\right)^2\left(\frac{E_{cm}}{10.58}\right)^{-2}\left(\log\frac{4}{\theta_{min}(\pi-\theta_{max})}-1\right) \qquad (1.50)\end{aligned}$$

with

$$\Theta\equiv\log\left(\frac{(1+\cos\theta_{max})(1-\cos\theta_{min})}{(1+\cos\theta_{min})(1-\cos\theta_{max})}\right)\approx 6 \qquad (1.51)$$

An estimation of the cross-section of the U boson production for DAΦNE as function of $\alpha_D k^2$ is shown in Fig. 1.5.2 with the constraints on the couplings

of a new $U(1)$ gauge group kinetically mixing with hypercharge from measurements of the muon anomalous magnetic dipole moment (shaded regions). The dotted lines correspond to the lower bounds of the range of couplings that could be probed by a search at LEP for rare Z-decays to various exotic final states, assuming that branching ratios as low as 10^{-5} can be probed.

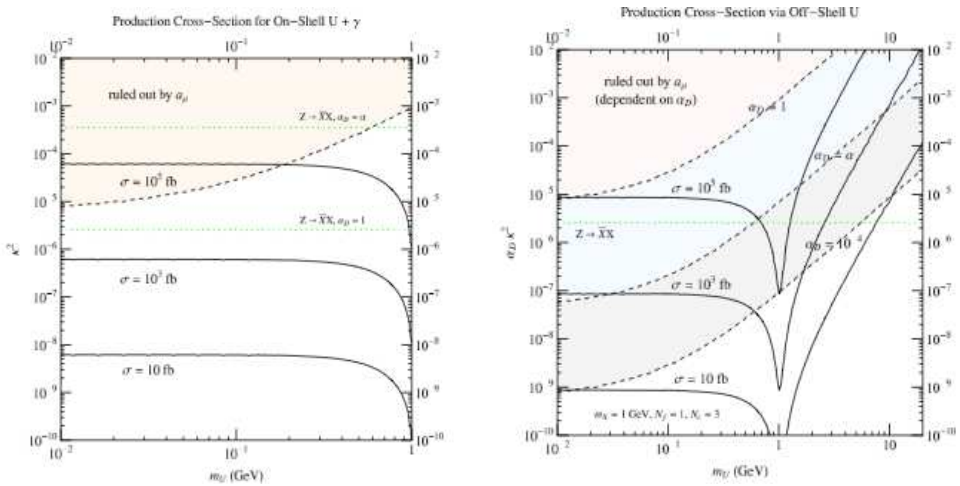

Figure 1.3: Cross-section at DAΦNE for the prodution of an on-shell (left) U-boson + photon and of an off-shell (right) U-boson as function of $\alpha_D k^2$.

1.5.3 Leptonic decay of U

A simple and interesting process to study is $e^+e^- \to U\gamma$. The expected cross section can be of the order of $\mathcal{O}(pb)$ at DAΦNE energies. The on-shell boson can decay into a lepton pair. So the signal $l^+l^-\gamma$ can be a signature of the U production. Denoting the rate of the signal process with σ_S, the QED process $e^+e^- \to \gamma\gamma$ has a rate $\sigma_0 \sim \sigma_S/k^2$. The main background (Fig. 1.4) in this case is the QED process $e^+e^- \to \gamma l^+l^-$ with the invariant mass of the lepton pair $m_{l^+l^-} \sim m_U$. The total rate for the QED background can be estimated as $\sigma_3 \sim (\alpha/\pi)\sigma_0 \log(E_{CM}/2m_l)$. The background rate in a window of size δm around $m_{l^+l^-} = m_U$ is [13]

$$\Delta\sigma_3 \sim \alpha\pi\sigma_0 \frac{\delta m}{m_U} = \frac{\alpha}{\pi}\frac{\sigma_S}{k^2}\frac{\delta m}{m_U} \tag{1.52}$$

Therefore, with a integrated luminosity $\mathcal{L}$ we have:

$$\frac{S}{\sqrt{B}} \sim \sqrt{\sigma_0\mathcal{L}}\frac{k^2}{\sqrt{\alpha/\pi}}\sqrt{\frac{m_U}{\delta m}} \times BR(U \to l^+l^-) \tag{1.53}$$

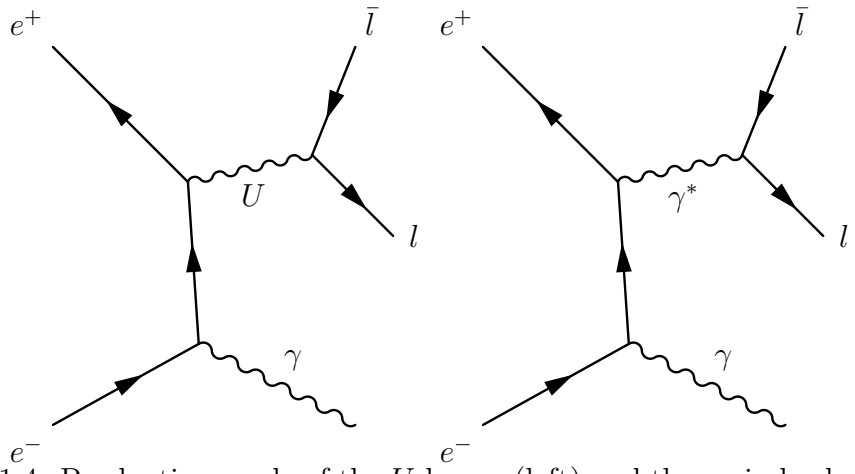

Figure 1.4: Production mode of the U-boson (left) and the main background contribution (right).

With the values of $\sigma_0 \sim 10^7\ pb$, $\int \mathcal{L}dt = 1\ ab^{-1}$ and $\delta m \sim 1\ MeV$ we can achieve a sensitivity $k \leq 10^{-4}$. The decay branching ratio into hadronic states can be extracted from the R-value. In eq. 1.53, the statistical sensitivity on k improves by a factor $\mathcal{L}^{1/4}$ with the increased luminosity. Therefore, a larger statistics can only extend the reach for the U-boson at colliders slowly. The BR of the $U \to l^+l^-$ process is

$$\Gamma_{U\to\bar{l}l} = \frac{1}{3}\alpha k^2 m_U \sqrt{1-\frac{4m_l^2}{m_U^2}}\left(1+\frac{2m_l^2}{m_U^2}\right) \tag{1.54}$$

Since m_U may overlap with hadronic resonances, the total decay width to hadrons can be directly related to the cross section $\sigma_{e^+e^-\to hadrons}$

$$\Gamma_{U\to\bar{l}l} = \frac{1}{3}\alpha k^2 m_U \sqrt{1-\frac{4m_\mu^2}{m_U^2}}\left(1+\frac{2m_\mu^2}{m_U^2}\right) R\left(s=m_U^2\right) \tag{1.55}$$

where as usual $R = \sigma_{e^+e^-\to hadrons}/\sigma_{e^+e^-\to\mu^+\mu^-}$ [14, 15].

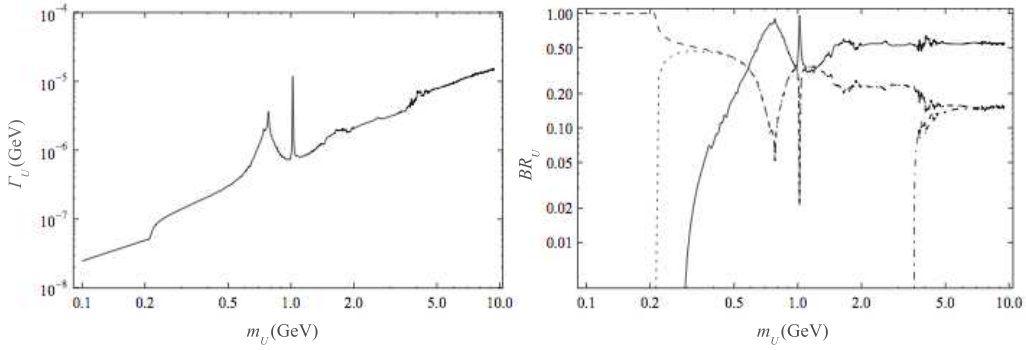

Figure 1.5: Total width Γ_U (GeV) (left) and branching ratios (right) for $U \to e^+e^-$ (dashed), $U \to \mu^+\mu^-$ (dotted), $U \to \tau^+\tau^-$ (dotted dashed) and $U \to hadrons$ (solid) for $k = 10^2$.

Chapter 2

DAΦNE and KLOE

2.1 The DAΦNE collider

DAΦNE (Double Annular Φ-factory for Nice Experiment) is a e^+e^- collider at LNF designed for high luminosity at the center of mass of the ϕ resonance. The nominal design luminosity is $5 \times 10^{32}\ cm^{-2}s^{-1}$. The collider is composed

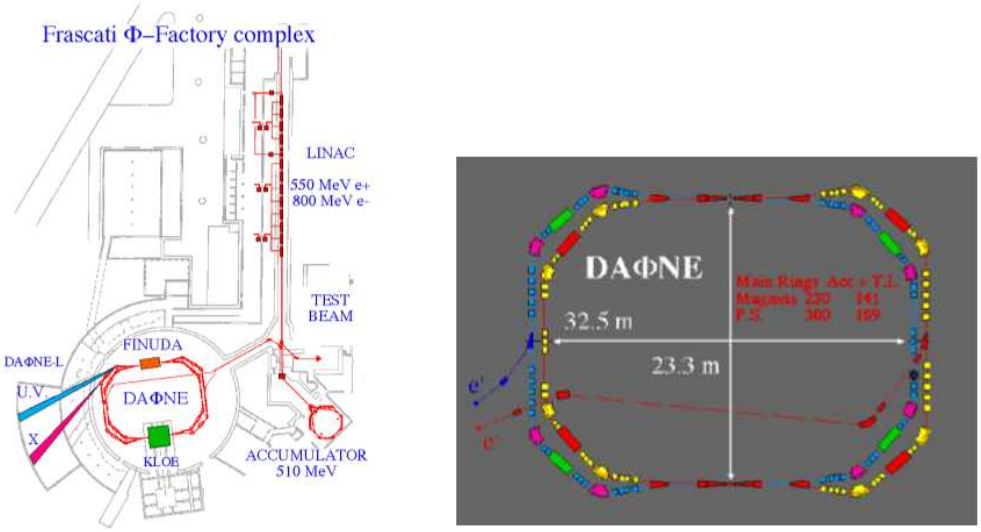

Figure 2.1: The DAΦNE complex (left) and the layout of the DAΦNE main rings (right).

by two separated rings: this layout allows to minimize the perturbation between the electron beam and the positron beam. The time separation for two consecutive bunches is 2.715 ns. The particles are injected at a energy

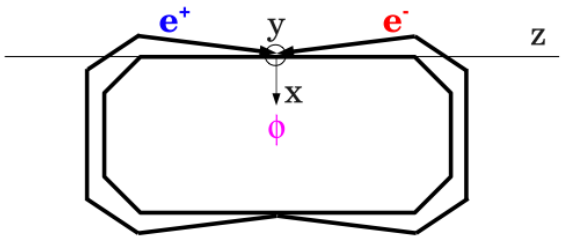

Figure 2.2: System of ccordinates in DAΦNE.

of $\sim$ 510 MeV and they collide with an angle of $(\pi - 0.025)$ radians: for this reason the ϕ meson is produced with a small momentum of 13 MeV/c along x axis (Fig. 2.2). The electrons are accelerated to the final energy in the Linac (Fig. 2.1), collected into the Accumulator and then transferred to the electron ring. The positrons require electrons to be accelerated up to 250 MeV to an intermediate station in the Linac, where positrons are produces; then they follow the same steps of the electrons and injected with another transfer line. The main parameters of DAΦNE are summarized in the following table:

Energy	0.51 GeV
Trajectory length	97.69 m
RF frequency	368.26 MHz
Harmonic number	120
Damping time, τ_E/τ_x	17.8/36.0 ms
Bunch length at full current e^+/e^-	2.8/2.2 cm
Beam currents e^+/e^-	2/1.4 A
Number of colliding bunches, n	108
σ_x	700 μm
σ_y	7 μm
σ_z	25 mm

Table 2.1: DAΦNE parameters during the 2004-2005 run period.

The ϕ production cross section is $\sigma\left(e^+e^- \rightarrow \phi\right) \simeq 3.1\ \mu b$. The dominant ϕ meson decays are shown in Tab. 2.2

Decay mode	Branching ratio
K^+K^-	$(48.9 \pm 0.5)\,\%$
$K_L^0 K_S^0$	$(34.2 \pm 0.4)\,\%$
$\rho\pi + \pi^+\pi^-\pi^0$	$(15.32 \pm 0.32)\,\%$
$\eta\gamma$	$(1.309 \pm 0.024)\,\%$
$\pi^0\gamma$	$(1.27 \pm 0.06) \times 10^{-3}$
e^+e^-	$(2.954 \pm 0.03) \times 10^{-4}$
$\mu^+\mu^-$	$(2.87 \pm 0.019) \times 10^{-4}$
ηe^+e^-	$(1.15 \pm 0.10) \times 10^{-4}$
$\pi^+\pi^-\gamma$	$(4.1 \pm 1.3) \times 10^{-5}$
$\mu^+\mu^-\gamma$	$(1.4 \pm 0.5) \times 10^{-5}$

Table 2.2: Decays mode of the ϕ meson [3].

2.2 The KLOE apparatus

The design of the detector apparatus obeys the requirements of a large acceptance for the K_L decays into charged and neutral particles, precise location of the decay vertices, good invariant mass resolution, γ-e-π identification and good self-calibrating capabilities [4]. The kaons produced in ϕ decays travel at approximately one fifth of the speed of light. The mean path of a K_L meson is about $\lambda_L = \beta\gamma c\tau = 3.4\ m$. The size of the apparatus is strongly dependent on this value. As shown in Fig. 2.3, the decay volume is mainly occupied by a Drift Chamber (DC), sorrunded by an Electromagnetic Calorimeter (EMC) and by the superconducting coil and the yoke of the magnet. The detector worked in $0.52\ T$ magnetic field along y coordinate (2.2), value chosen in order to optimize the acceptances, pattern recognition and momentum resolution.

2.2.1 The beam pipe

The K_S decay length is $\sim 0.6\ cm$ and the beam pipe inside the apparatus is designed such that all K_S mesons decay in vacuum. A sphere of 10 cm radius (Fig. 2.4) made of Be-Al alloy ($62\% - 38\%$) is welded on the beam pipe, in order to minimize nuclear interactions, photon absorption and kaon regeneration.

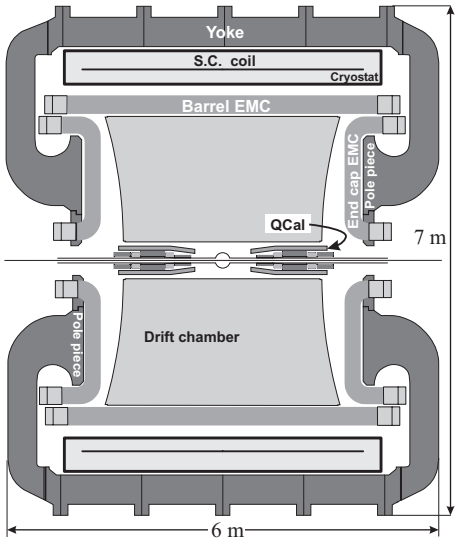

Figure 2.3: Cross section of KLOE apparatus

2.2.2 The Drift Chamber

The tracking chamber [16] must be as transparent as possible, since it should reconstruct all the charged secondary products from a decay, measuring their properties without affecting the performance of the calorimeter in the detection of neutral secondary products. The detector provides a spatial resolution of $\sim 200\ \mu m$ in the bending plane. The tracking chamber is a cylindrical drift chamber whose structure is made of carbon fibers, with low Z and low density material to minimize multiple Coulomb scattering, absorption of photons and $K_L \rightarrow K_S$ regeneration, that simulates CP violating decays. The DC is filled with a light gas mixture, 90% He and 10% iC_4H_{10}. The dimensions of the drift chamber are 2 m outer diameter, 25 cm inner diameter and 4 m length. The chamber has 12582 almost square drift cells with a ratio of field to sense wires of 3 : 1 arranged in 58 concentric cylinders inclined with alternated stereo angle that progressively increases with the radius. The almost square shape is due to the requirements of three-dimensional track reconstruction and a uniform efficiency throughout the chamber volume. This also implies that the cells are arranged into coaxial layers with alternating stereo angle. The stereo angle of the kth layer, ε_k, is the angle between the wires and the chamber axis (Fig. 2.5 left). The radial distance of a wire from the chamber axis changes along z direction: it reaches the maximum (R_k) at the end plates and the minimum (R_{k_0}) at the centre of the wire (Fig. 2.5 left). Choosing a constant value for the difference $\delta_k = R_k - R_{k_0}$ implies the

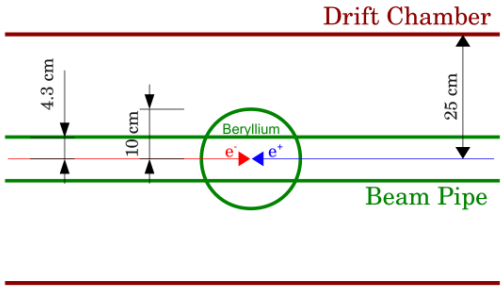

Figure 2.4: Beam pipe at the KLOE interaction region and regeneration surfaces.

most filling of the sensitive volume of the chamber. The kth stereo angle can be written as function of the δ_k:

$$\tan\varepsilon_k = \pm\frac{2\delta}{L_k}\sqrt{\frac{2R_{k_0}}{\delta} - 1}$$

with L_k the distance between the end plates of the kth layers. This allows us to fix a value for the δ_k starting from the request of a good resolution in the measurement of the z coordinate, since $\sigma_z = \sigma_{r\phi}/\tan\varepsilon$. Asking also for small stereo angle, the δ_k was chosen to be 1.5 cm, and the stereo angle can range between ± 60 $mrad$ and ± 150 $mrad$. The shape of the cells changes slowly along z direction in a periodic way. The wires at radius R_{k-1} are almost parallel ($\varepsilon_k \approx \varepsilon_{k-1}$) to the wires at R_k, while the wires at R_{k+1} have stereo angle $\varepsilon_{k+1} \approx -\varepsilon_k$. The difference between the number of cells in two consecutive layers is constant. Measurements with low and high energy particle beams showed that the size of the cells could be ~ 3 cm. Since the track density is higher for small radii, the cells size near the DC inner wall is smaller. In conclusion, the cells area is 2×2 cm^2 in the 12 innermost layers and 3×3 cm^2 in the other 48 layers (Fig. 2.6).

Wires The sense wires are made of gold-plated tungsten and they have a 25 μm diameter. The presence of these wires lows the radiation length of the chamber from $\sim$ 1300 m down to $\sim$ 900 m. The field wires are instead made of aluminium, whose low Z and low density result in a smaller load for the plates. Their diameter is 80 μm to limit field emission and gas amplification near the wire surface. Two layers of guard-field shaping are

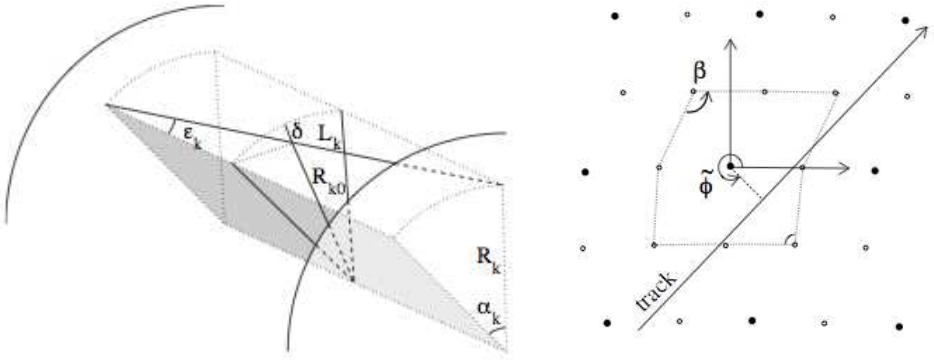

Figure 2.5: Wire geometry. ε_k is the stereo angle and α_k the difference in azimuth at the two ends fpr a wire of the kth layer (left). Definition of β and $\tilde{\phi}$ characterizing the shape of the cell and the angle of the incident track (right).

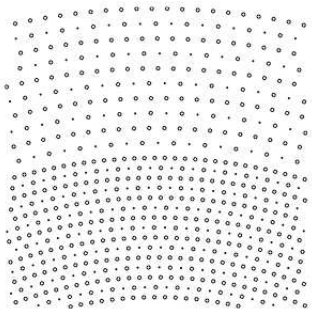

Figure 2.6: Drift cells configuration at $z = 0$. Small cells and big cells are shwon. Full dots represent the sense wires, open circle the field wires.

located at $R_{in} = 27.5$ and $R_{out} = 191.5$ cm. Wire properties are listed in the Tab. 2.3. Each wire is supported on both sides by a feedthrough inserted in the chamber end plate. The feedthrough hosts a pin which is crimped on the wire. The accuracy on the wire location is ≤ 30 μm.

Mechanical structure Two end plates close the ends of the chamber. They are shaped as spherical caps (9.76 m radius) with a 25 cm hole at the center and they are kept apart by 12 structs attached to the rim of the plates. Each rim (L-shaped) hosts 48 screws which apply a tangential pull to the plate. The combination of this force and the axial load due to the wire tensioning results in the spherical shape of the plates, reducing their deformation. The outer cylindrical wall is composed by 12 panels made of two layers of 1.5 mm intermediate modulus carbon fiber fabric glued on 3.6 cm honeycomb structure. The 12 structs have a hollow rectangular cross-section 5×3 $cm^2, 0.5$ cm thickness. They are designed in order to avoid bending instability. The inner wall of the chamber is made of 0.75 mm of the same modulus carbon fiber and is aluminated on both sides with a foil of 0.10 mm. The inner and outer walls are glued after the wire tensioning.

Wire material	**Sense (W+Au)**	**Field (Al5056+Ag)**
Diameter (μ)	25.0	81.4
Coating diameter (μm)	0.25	1.0
Linear density (mg/m)	9.3	16.5
X_0 (cm)	0.35	8.9
Elastic limit (g)	~ 100	~ 350
Ultimate tessile strength (g)	~ 160	~ 410

Table 2.3: Wire properties.

Gas mixture In order to minimize the multiple scattering and density, the gas mixture chosen is He:iC_4H_{10} 90 : 10. The properties of this mixture are listed in Tab. 2.4. Measurements with particle beams showed a spatial resolution of 130 μm for high momentum particles. The choice of Helium requires that the apparatus must be as tight as possbile, even if the He leaks more rapidly than any other gas. The gas system works in open mode since the chamber tightness is excellent, assuring a gas flow of 100 standard liters per minute.

Parameter	Value
N° primary clusters[1]	$12.3 \pm 0.2\ cm^{-1}$
N° of total clusters[1]	$\sim 19\ cm^{-1}$
Drift velocity, $E = 0.5 \div 1\ kV/cm$	$17 \div 23\ mm/\mu s$
α_L, $E = 0.5 \div 1\ kV/cm, B = 0.6\ T$	$0.2 \div 0.3\ rad$
Diffusion coeff., $E = 0.5 \div 1\ kV/cm$	$(3.2 \div 2.5) \times 10^{-4}\ cm^2/\mu s$
Radiation length	$\sim 1300\ m$

Table 2.4: Properties of the 90 : 10 He:isoC$_4$H$_{10}$.

Track reconstruction Three steps are adopted by the algorithm to reconstruct tracks in the chamber: pattern recognition, track fit and vertex fit. The *pattern recognition* works associating hits and reconstructing segments first in the $x - y$ plane, starting from the outermost layer towards the interaction point. The hits are detected and associated to form a chain. When three hits make a chain. a fourth hit is added if the curvature of the $n-2$, $n-1$, n hits and $n-1$, n, $n+1$ are consistent. To fix the left-right ambiguity, a χ^2 is computed choosing the lowest value. A track requires at least four hits in at least two wire layers. The track is then refitted and the parameters computed on the two sides of the chambers: the tracks are choosen combining the two views according to curvature values and geometrical compatibility. The z coordinate is then added to complete 3D reconstruction. The *track fit* minimizes the χ^2 function computing the difference between measured expected distance (from space-time relation) and the fit. The procedure is iterative since the cells response depends on track parameters. The track fit adds hits missed by pattern recognition, rejects the ones wrongly assigned to the track and joins the splitted tracks. The *vertex fit* computes a χ^2 for each track pair. The aim is to reconstruct primary and secondary vertices. A χ^2 function is computed starting from the distance of the closest approach between tracks and the extrapolation errors. In the extrapolation, the track momentum is corrected for energy loss in the beam pipe and in the drift chamber inner wall, while the multiple scattering is taken into account in the covariance matrix.

Spatial resolution Using Bhabha scattering events the resolution on beam parameters were measured. They are summarized in table 2.5.

Longitudinal beam-beam IP position (Δz)	$(12.9 \pm 0.1)\ mm$
Horizontal beam-beam IP position ($\|Deltax$)	$(1.20 \pm 0.005)\ mm$
ϕ transverse momentum	$(13.0 \pm 0.1)\ MeV$
Center of mass energy	$(1019.5 \pm 0.5)\ MeV$
Bem-beam energy spread	$(0.302 \pm 0.001)\ MeV$
Luminosity $\delta\mathcal{L}/\mathcal{L}$	0.6%

Table 2.5: Measurements of the beam-beam interaction parameters using Bhabha scattering events.

2.2.3 The Electromagnetic Calorimeter

The KLOE calorimeter [17] must provide a measurement of the energy and position of photons, copiously produced by the decays of neutral pions. Moreover the calorimeter measures the arrival time of particles. Determining the distance travelled by a K_L before it decays to π^0's is crucial to study CP violation. The requirements for energy scale is $\sim 5\%$ at 1000 MeV and this resolution is mantained thanks to continous calibration (using Bhabha scattering events). KLOE requires a very good time resolution, full solid angle and a small amount of dead material in front of the calorimeter. This led to choose lead-scintillating fiber samplig calorimeter, which have a good light trasmission up to $\sim 4.3\ m$ and let have a good hermeticity without dead material between the calorimeter and the outer wall of the drift chamber. 24 modules ($4.3\ m \times 23\ cm$ and trapezoidal cross-section with basis 52 cm and 59 cm) form the barrel, while the end caps are built with 32 vertical modules $0.7 - 3.9\ m$ long and 23 cm thick with rectangular cross section of variable width. The end caps are inserted into the barrel calorimeter. This overlap allows not to have inactive gaps. Each module is composed by a 1 mm diameter scintillating fibers sandwiched between 0.5 mm thick lead foils, glued together with a special exposy. Fibers are mostly orthogonal to the entering particles. The ratio of volumes lead:fiber:exposy is $42 : 48 : 10$. The average density is 5 g/cm^3 and the overall thickness of the calorimeter is ~ 15 radiation length, where a radiation length is $\sim 1.5\ cm$. The fibers run parallel to the axis of the detector in the barrel and vertically in the end caps. The attenuation length is between 3 and 5 m and the light yield is equivalent to $\sim 1\ photo-electron/mm$ of crossed fiber at 2 m distance from a photo-tube. The timing rms uncertainty is $\sigma_0/\sqrt{N_{pe}}$, with N_{pe} number of photoelectrons and σ_0 between $2.2 - 2.5\ ns$. The readout is on both sides of each module, with a light guide shaped as Winston cones. The quantum efficiency of the photocathode is $\sim 20\%$. The readout divides the calorimeter

into five planes in depth. Each plane is divided in the transverse direction into elements 4.4 cm wide. The readout segmentation gives a resolution of $\sim 1.3\ cm\left(4.4/\sqrt{12}\right)$.

Clustering For each cell (here defined as a calorimeter segment, where the segmentation is defined by light collection segmentation), the signals are read on both sides (let's say A and B). So two time signals $t^{A,B}$ and two amplitude signals $S^{A,B}$ are recorded. The longitudinal position of the energy deposit is computed as $t^A - t^B$. The particle arrival time t (the zero is at the fiber center) and its coordinate s are obtained as

$$t\ (ns) = \frac{t^A + t^B}{2} - \frac{t_0^A + t_0^B}{2} - \frac{L}{2v} \tag{2.1}$$

$$s\ (cm) = \frac{v}{2}\left(t^A - t^B - t_0^A + t_0^B\right) \tag{2.2}$$

where

$$t^{A,B} = c^{A,B} \times T^{A,B} \tag{2.3}$$

with $T^{A,B}$ in TDC counts and $c^{A,B}$ in ns/TDC counts. L and v are the cell length (cm) and the ligth velocity in the fibers (cm/ns). The energy signal E in each side of the i-th cell is computed as

$$E_i^{A,B}\,(MeV) = \frac{S_i^{A,B} - S_{0,i}^{A,B}}{S_{M,i}} \times k_E \tag{2.4}$$

$S_{o,i}$ is the zero-offset of the amplitude scale, $S_{M,i}$ is the response for a m.i.p crossing the calorimeter center. k_E gives the energy scale in MeV and it is obtained from showering of particles of known energy. In order to compute a response which is independent from the position, the cell energy formula is expressed

$$E_i\ (MeV) = \left(E_i^A A_i^A + E_i^B A_i^B\right)/2 \tag{2.5}$$

where $A_i^{A,B}$ are correction factors due to the attenuation length along the fiber. Once known the cells energy and times, the cluster energy is obtained as

$$E_{clu} = \sum_i E_i \tag{2.6}$$

while the cluster position and the cluster time are computed as

$$\vec{R}_{clu} = \frac{\sum_i E_i \vec{R}_i}{\sum_i E_i} \tag{2.7}$$

$$T_{clu} = \frac{\sum_i E_i t_i}{\sum_i E_i} \tag{2.8}$$

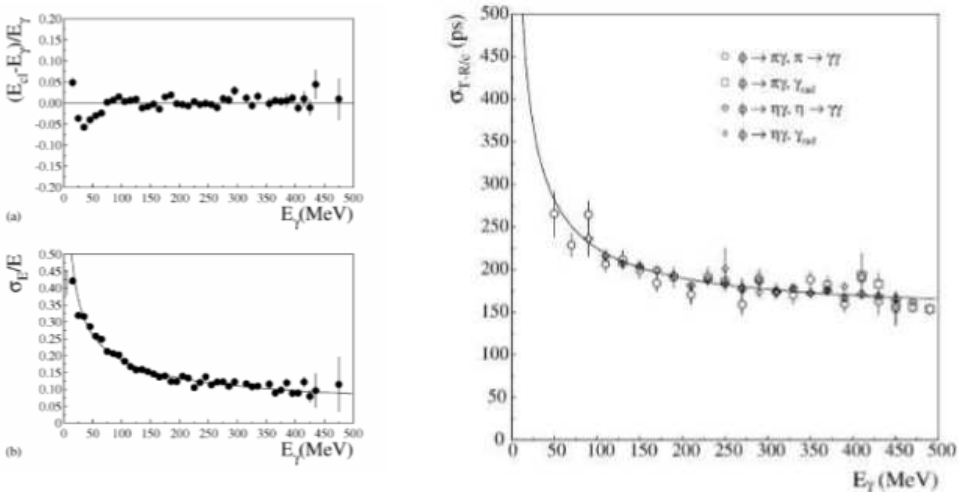

Figure 2.7: Energy linear response $(E_{clu}-E_\gamma)/E_\gamma$ vs E_γ (top left) and energy reolution vs E_γ (bottom left). Time resolution as function of energy (right).

with $\vec{R}_i = (x_i, y_i, z_i)$. z_i is the coordinate along the fiber, x_i and y_i the nominal position of the cell.

Spatial and time resolution Radiative Bhabha events can be used to study energy resolution and linearity of the calorimeter since the photons produced cover a wide energy and angular range. In each 10 MeV range, the distribution $E_{cl}-E_\gamma$ is fitted with a Gaussian to find the central value. In Fig. 2.7(a) (top) the $(E_{cl}-E_\gamma)/E_\gamma$ vs E_γ is shown. The linearity is better than 1% for $E_\gamma > 75\ MeV$, while it is at the $4-5\%$ level below. The energy resolution as function of photon energy is shown in Fig. 2.7(a) (bottom). The resolution is fitted with $a/\sqrt{E\,(GeV)}+b$, obtaining $a = 5.7\%$ and b negligible. Time resolution is computed starting from the difference $T_{clu}-R_{clu}/c$ for the two photons in $\phi \to \pi^+\pi^-\pi^0$ events. Fitting the distribution in Fig. 2.7(b), we obtain $\sigma_t = 54\ ps/\sqrt{E\,(GeV)} \oplus 140\ ps$.

2.2.4 QCAL

The KLOE experiment was designed to study the CP violation into the $K\bar{K}$ system through the double ratio $R(\varepsilon'/\varepsilon)$ measurement

$$R = \frac{\Gamma\left(K_L^0 \to \pi^+\pi^-\right)/\Gamma\left(K_L^0 \to \pi^0\pi^0\right)}{\Gamma\left(K_S^0 \to \pi^+\pi^-\right)/\Gamma\left(K_S^0 \to \pi^0\pi^0\right)} \tag{2.9}$$

The most important background source in these channels is represented by $K_L^0 \to 3\pi^0$ and to reduce it significantly the experiment was provided of a couple of calorimeters surrounding the two DAΦNE quadrupoles close to the IP. These calorimeters (QCAL) had cylindrical shape and they were made of 16/15 layers of 1.9 mm Pb and 1 mm scintillator tile (BC408). The light signal readout was made by 1 mm WLS fibers (Kuraray Y11-200) optically coupled with the tile in open air. The collected light was sent to standard PM. The calorimeters are characterized by low light response $1 \div 3$ $pe/mip/tile$ at 0 distance from PM due to coupling in air, long WLS fibres (2 m) and PM quantum efficiency (20%). Moreover the Z position is obtained by complicated time difference and the final resolution is about $12 \div 14$ cm. QCAL worked well on rejecting background losing just 1% of signal.

2.2.5 The Trigger

The need for precision measurements requires a very efficient trigger, taking into account the high DAΦNE luminosity (10^{32} $cm^{-2}s^{-1}$). The basic requirements is that the efficiency ϵ_T is identical for $\pi^+\pi^-$ and $\pi^0\pi^0$ decays of K_L and K_S. The trigger system must perform the following functions:

- Produce trigger for all ϕ events (300 Hz)
- Recognize Bhabha events and accept a downscaled sample at small angle (30000 Hz)
- Recognize cosmic rays events (3000 Hz) and pass a downscaled sample
- Reject background

The trigger rapidly recognizes event topologies and energy deposits. The threshold for most of the data was chosen 50 MeV in the barrel and 150 MeV in the endcaps. Events with only two trigger sectors in the same endcap are not accepted, because such as events are dominated by machine background. Events with charged particle give large number of hits in the DC. The trigger uses the information from groups of DC drift cells requiring at least 15 hits

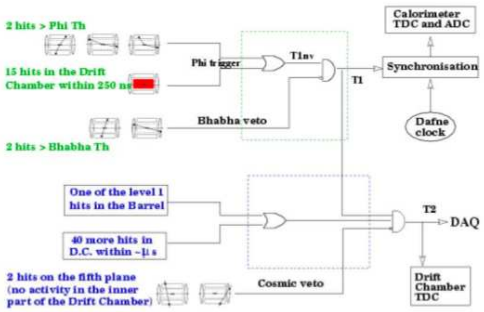

Figure 2.8: KLOE trigger logical scheme

within a time window of 250 ns from the beam crossing (Fig. 2.8). A first level trigger *T1* is produced with minimal delay and is synchronized with the DAΦNE master clock. The second level trigger *T2* uses more information (at least 120 hits from the DC) but less stringent time requirements (1.2 μs time window) and it is used to inizialize or to abort *T1*. Data conversion and readout is done in a fixed time of 2 μs following the *T1* signal. The trigger is able to flag cosmic ray events which are recognized by the presence of two energy deposits above 30 MeV in the outermost calorimeters layers. The trigger rate at a luminosity of 10^{32} $cn^{-2}s^{-1}$ is $\sim$ 2000 Hz. About 500 Hz are associated to ϕ decays and Bhabha scattering. Signals from KLOE subdetectors are recorded, digitized and fed by optical fibers to the computers. The event is reconstructed by a three-level scheme (Fig. 2.9), where

- **L1** level gathers event data within a single FEE crate
- **L2** level combines the informations from several crates
- the third level is responsible for final event building

The recostructed event is displayed in the Control Room. A background rejection filter (FILFO) was implemented taking only information on cluster and on DC cells counts. This allows to reject background events before the reconstruction in the drift chamber.

Bunch-crossing identification The bunch-crossing time is $T_{RF} = 2.715$ ns. For this reason the trigger is not able to identify the bunch crossing related to each event. The TDC starts as soon as the L1 trigger is phase-locked

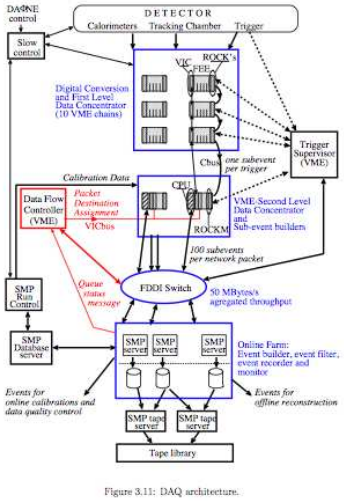

Figure 3.11: DAQ architecture.

Figure 2.9: KLOE DAQ architecture

to a replica of the RF frequency (the clock period is $4 \times 2.175\ ns$). This allows to obtain the T_{tof} from the T_{TDC} according to the following formula:

$$T_{tof} = T_{TDC} - \delta_C + N_{BC} T_{RF} \tag{2.10}$$

where δ_C is the overall electronic offset and cable delay and N_{BC} is the number of bunch-crossing before the TDC starts. δ_C and T_{RF} are determined for each data taking run with $e^+e^- \to \gamma\gamma$ events. The ditribution of $\Delta_{tof} = T_{clu} - R_{clu}/c$ (Fig. 2.10) reveals well separated peaks: each of them correspond to a different value of N_{BC}. The δ_C is defined as the position of the peak with the largest statistic. These values are determined with a precision of $\sim 4\ ps$. A time offset $t_{0,clu} \equiv \delta_C - N_{BC} T_{RF}$ must be subracted from the T_{clu} in order to match this value with the T_{tof}. $N_{BC} T_{RF}$ varies for each event. A value for N_{BC} can be chosen assuming that the earliest cluster in the event is generated by a prompt photon coming from the interaction point, so that $T_{tof} = R_{clu}/c$ for this cluster. The time offset can be so written

$$t_{0,evt} = \delta_C - Int\left[\frac{R_{clu}/c - T_{clu} + \delta_C}{T_{RF}}\right] T_{RF} \tag{2.11}$$

and $Int[\ ]$ means the nearest integer to the argument. It is also requested that the energy for this prompt cluster is $E_{clu} > 50\ MeV$.

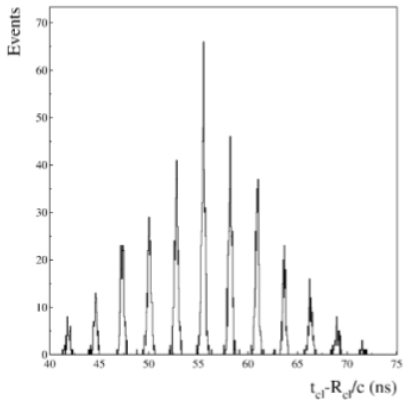

Figure 2.10: Δ_{tof} distribution for 2γ events. The separation of peaks is $T_{RF} = 2.715\ ns$.

2.2.6 Event classification

The classification algorithms divides the events according to the following list:

- generic background coming from beam, cosmic ray and Bhabhas
- large angle Bhabhas used to calibrate calorimeter and to evaluate luminosity
- K_L and K_S decays
- K^+ and K^- decays
- $\phi \rightarrow \pi^+\pi^-\pi^0$ decays
- two charged tracks (for example $\pi+\pi^-/\mu^+\mu^-$) and fully neutral $n\gamma$ final states

The analysis described in chapter 6 is focused on the events selected by this last stream condition.

Chapter 3

KLOE-2

KLOE experiment collected 2.5 fb^{-1} at the ϕ peak (1020 MeV) plus additional 250 pb^{-1} at 1 GeV. For the forthcoming run KLOE has been upgraded with new subdetectors (KLOE-2).

3.1 Upgrade of the KLOE apparatus

Here follows a brief description of the new detectors that will be installed in KLOE.

3.1.1 QCALT

To increase detection efficiency and to reduce the accidental losses, the KLOE-2 experiment will be provided with two new tile calorimeters around the quadrupoles of DAΦNE machine. Each calorimeter has dodecagonal structure (Fig. 3.1 (left)) (0.9 m length) made of 5 layers of 3.5 mm thick W, 5 mm thick BC408 scintillator tiles and 1 mm air gap for a total of 5.5 X_0 (4.75 cm depth) (Fig. 3.1 (right)) along the z axis each layer is segmented in 18 cells. The cells are individually readout by 1 mm diameter fibers (Saint Gobain MC) and the light sent to a SiPM (Hamamatsu MPPC400 pixel), for a total of 2160 electronic channels. The time resolution is about 750 ps and it has about 30 $pe/mip/tile$ and 1.5 cm spatial resolution along z axis. The tile uniformity tests and the response stability along time are underway with UV LED in the Alte Energie Laboratory of the Cosenza Physics DEpartment.

3.1.2 CCALT

The electromagnetic calorimeter of KLOE covers up to $\geq 21 \div 22°$. To extend the coverage at lower angles (8°), both as veto detector ($K_S^0 \to \gamma\gamma$)

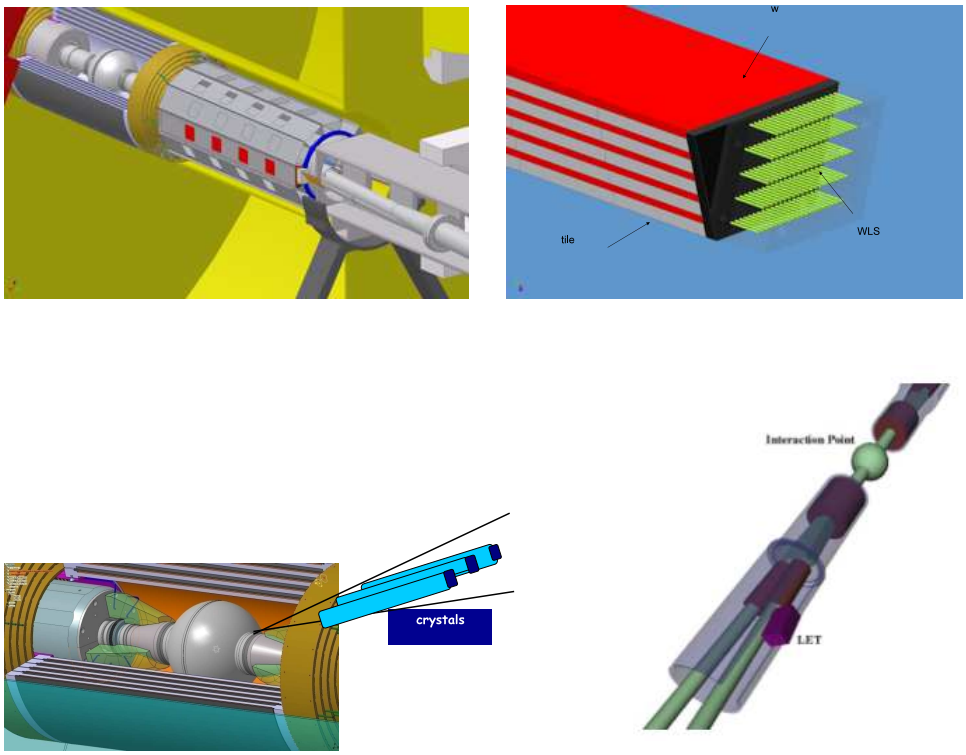

Figure 3.1: Top left: integration of the QCALT; top right: cross-section of a twelfth of QCALT; bottom left: the integration of CALT; bottom right: integration of LET.

or as acceptance extension for rare decay channels ($K_S^0 \rightarrow 3\pi^0$), two small barrels of 24 crystals/each with length from $10 \div 13$ cm and transversal area 1.5×1.5 to 2×2 cm^2 will be installed between the IP and the QCALT, as shown in Fig. 3.1 (bottom). The crystals should be fast and with high light yield. The LYSO crystal match all these features. The energy resolution has been measured at BTF of LNF and the fit of data gives the following terms: $2.4\%/\sqrt{E(GeV)}$ (stochastic), $0.8\%/E(GeV)$ (electronic noise) and 5% (constant due to leakage, light production and collection non uniformity, calibration).

3.1.3 HET and LET

A relevant part of the physics program of the KLOE-2 project is devoted to the $\gamma\gamma$ physics. As a matter of fact the photon-photon scattering gives

access to states with $J^{PC} = 0^{\pm+}, 2^{\pm+}$, and in particular the golden channel $\gamma\gamma \to \pi^0\pi^0$ in the low energy region can infer the existence of the $\sigma(600)$ meson. In order to reduce the huge background coming from the ϕ decays, a couple of tagging system is needed: low-energy tagger (LET) [19] and high-energy tagger (HET) [20]. The first (matrix of LYSO crystals) is placed 1 m far from the IP in the horizontal plane and will detect final leptons with energy between 50 and 450 MeV. The latter is placed inside the machine lattice, 11 m far from the IP, as close as possible to the beam line. The HET tagger is costituted of 30 fast scintillators EJ228 which provide a spatial resolution of 2 mm corresponding to 500 keV/c momentum resolution.

3.1.4 Inner Tracker

An Inner Tracker will be placed between the beam pipe and the DC inner wall. This detector will:

- reduce the track extrapolation length and improve the decay vertex reconstruction capability.
- increase the geometrical acceptance for low momentum tracks, presently limited by KLOE magnetic field and by the distance of the DC first layer and optimize their detection.
- improve the track momentum resolution.

The realization and the tests of a prototype of an Inner Tracker will be investigated in the following chapters.

3.2 Improvement on kaon decoherence and CPT violation

The channel $\phi \to K_S K_L \to \pi^+\pi^-\pi^+\pi^-$ provides many tests about foundamental physics. The KLOE collaboration, studying this channel, measured the distribution $I(\pi^+\pi^-, \pi^+\pi^-; |\Delta t|)$. Moreover, some important limits on γ,$\Re\omega$ and $\Im\omega$, the parameters related to the possible decoherence and CPT violation in the neutral kaon system, were reached. Also on the parameters ζ_{00} and ζ_{SL} were put some stringent bounds. All these measures are dominated by the statistical uncertainty (Fig. 3.2). A decoherence effect should manifest as a deviation from quantum mechanical prediction $I(\pi^+\pi^-\pi^+\pi^-; |\Delta t| = 0) = 0$. In order to perform this measure, a very high resolution in time and space is needed to reconstruct closed vertices near

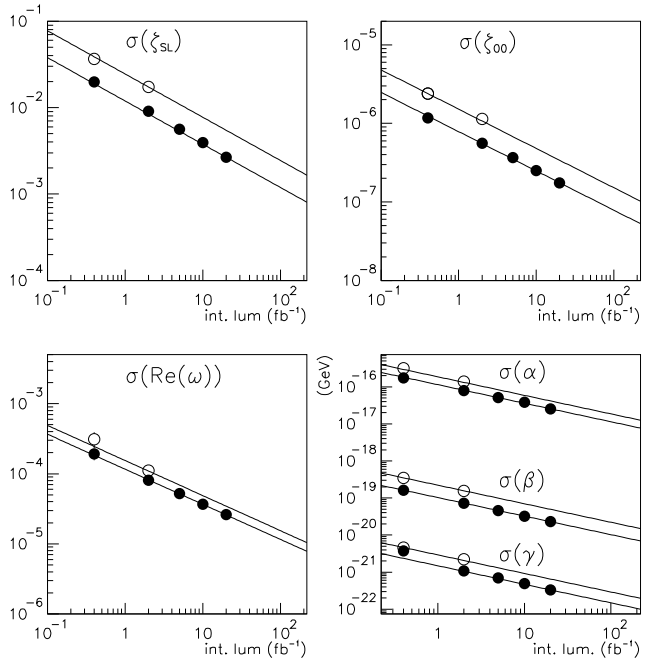

Figure 3.2: The statistical sensitivity to the parameters ζ_{SL} (top left), $\zeta_{\bar{0}0}$ (top right), $\Re\omega$ (bottom left) and α, β, γ (bottom right) withj the present KLOE resolution $\sigma_{|\Delta t|} \equiv \tau_S$ (open circles) and with improved resolution $\sigma_{|\Delta t|} \equiv 0.3\tau_S$ (full circles); solid lines represent $1/\sqrt{\mathcal{L}}$ function.

to the IP. As shown in Fig. 1.1(a) the distribution of $I(\pi^+\pi^-\pi^+\pi^-; |\Delta t| = 0) = 0$ can be fitted by the Monte Carlo curve if time resolution is improved. A resolution $\sigma_{|\Delta t|} \simeq 0.3\tau_S$ was obtained using the corresponding $|\Delta t|$ scale factor in the smearing matrix and in the efficiency curve. This has effect on the measurements of the decoherence and CPT violation parameters, but on the other side we introduce systematic uncertainties. Nevertheless, the statistical sensitivity on the decoherence and CPT violation parameters has an improvement of a factor two, equivalent to increase the luminosity of a factor four. For these reason, an Inner Tracker between the beam pipe and the drift chamber is strongly recommended, since all the possible measures can be improved.

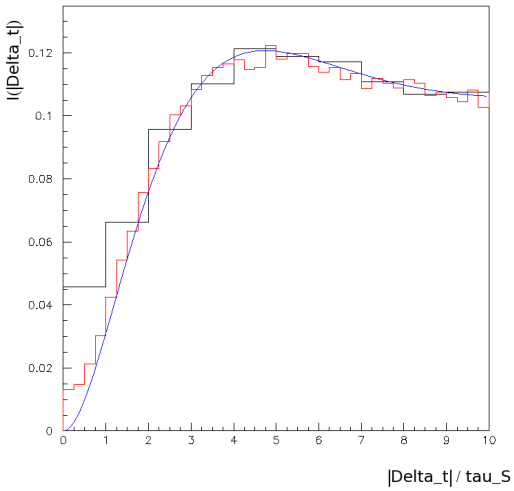

Figure 3.3: The $I(\pi^+\pi^-, \pi^+\pi^-; |\Delta t|)$ distribution as function of $|\Delta t|$ in τ_S units. The wide bins represent KLOE resolution $\sigma_{|\Delta t|} \approx \tau_S$; the narrower bins represent an improved resolution $\sigma_{|\Delta t|} \sim 0.3\tau_S$; the line is the ideal case. Simulation results.

3.3 Improvements on other decay modes

The insertion of an Inner Tracker can help the study on K_S rare decays. The KLOE experiment provides a pure K_S beam, since they are tagged reconstructing K_L decays and K_L interactions in the calorimeter. The dominant mode on K_S decays is the channel $K_S \to \pi^+\pi^-$, well controlled using kinematic constraints. The Inner Tracker will better solve tracking and vertex reconstruction and will optimize the low momentum tracks detection. In fact, the channel $K_S \to \pi e \nu$ is a test for CPT symmetry, $\Delta S = \Delta Q$ rule and it is related to the V_{us}. KLOE measured this branching ratio with a total error of $\sim 1.3\%$ using an intgrated luminosity of 410 pb^{-1}. The statistical contribution is up to 1.1%. By the Inner Tracker, the error is guessed to be completely dominated by the systematic uncertainties (0.7%) at an integrated luminosity of $10 \div 20$ fb^{-1}. These considerations can apply to $K_S \to \pi\mu\nu$,

$K_s \to \pi^+\pi^- e^+ e^-$ or $K_S \to \pi^0 e^+ e^-$. The improvement in the acceptance of low momentum tracks will help the measurement of the branching ratio of $\eta \to \pi^+\pi^- e^+ e^-$ [22]. The uncertainty to this BR has a statistical contribution of 3.4% and a systematic one of 2.6%. The transverse momentum distribution of the four tracks events is peaked at $\sim 10\ MeV/c$. The minimum detectable tranverse momentum in the DC of KLOE is $\sim 23\ MeV/c$ because of the magnetic field[1]. Moreover, the largest contribution (70%) to systematic uncertainty is due to the cut to reject $\eta \to \pi\pi\gamma$ events with γ conversion in the beam pipe. The insertion of an inner tracker will improve the acceptance of low momentum tracks and will improve the efficiency of the background rejection. Similar effects are foreseen for the $\eta \to e^+e^-e^+e^-$ and $\eta \to e^+e^-\mu^+\mu^-$ decays with a BR in the range $10^{-5} \div 10^{-7}$. For the same reasons, the inner tracker will improve detection capability of multi-lepton events connected to the decay of a vector boson belonging to a secluded gauge sector (see sec. 1.5).

3.4 Detector requirements

The design of the Inner Tracker depends on the physics requirements and space constraints. In Fig. 1.1(a) the interference term is shown as a function of K_S lifetime units ($\tau_S \simeq 0.6\ cm$ at a $\phi-$factory). Since the detector must preserve the $K_S - K_L$ interference region, from Fig. 1.1(a) follows that the inner radius of the IT must be at least $\simeq 20\ \tau_S \simeq 12\ cm$. The outer radius is bounded by the inner wall of the Drift Chamber: 25 cm. The request of a better resolution (a factor $3-4$) on the K_S decay point has important consequences on detector design. The decay vertex near IP will be extrapolated following the charged track reconstructed in IT, starting from its inner layer pointing to the decay point. This means that the resolution of the detector and multiple scattering must be carefully studied, fixing a maximum contribution to material budget of $\sim 2\% X_0$. The event rate from ϕ decays at $\mathcal{O}\left(10^{33}\right)\ cm^{-2}s^{-1}$ is of the order of 10 kHz. A crucial parameter for the inner tracker is the occupancy of the detector to the the machine background events. An estimation of this background can be obtained from the FINUDA experiment: at a radius of 6 cm from IP this detector collected $7-8$ hits/plane in 2 μs of integration time at $10^{32}\ cm^{-2}s^{-1}$ luminosity. Scaling with the luminosity and the geometry of the detector, the occupancy for the IT is $10-20$ hits/layer in 1 μs integration time. In conclusion, the requirements for the IT are:

[1] Below this value, the trajectory of particles is expected to be a helix with radius lower than 25 cm.

- $\sigma_{r\phi} \sim 200\ \mu m$ and $\sigma_Z \sim 400\ \mu m$ spatial resolution: this means an improvement of a factor 3 on actual K_S decay point resolution

- 2 $\%X_0$ overall material budget

- 5 kHz/cm^2 rate capability

3.5 Detector layout

The proposed detector is made by four tracking layers with a 2D readout, able to perform a 3D reconstruction of points along the track. The active length of all layers is 700 mm. The Inner Tracker will be formed by four cylindrical-GEM. A cylindrical-GEM is composed by three cylindrical GEM foils between two cylindrical electrodes. In the Inner Tracker the cathode will be the inner layer of a CGEM. The anode will be segmented with 650 μm pitch XV patterned strips with a stereo angle of 40¬∞. The system will have about 30000 FEE channels. The GEM technology allows to have a high spatial resolution (depending on the strips pitch) and a very light detector, minimizing multiple scattering effect for low momentum tracks.

Chapter 4

The Gas Electron Multiplier

4.1 Micro-Pattern Gaseous Detectors

Micro-pattern gaseous detectors [3, 23] are replacing conventional wire chambers, since of their better performancies. Few hundreds volts allow to achieve very high fields with typical gain of $10^3 \div 10^4$. Moreover these devices own a high rate capability and that make this technology attractive for charged particle tracking at high luminosity colliders. An example of MPGD is the Gas Electron Multiplier (GEM).

4.2 The GEM detector

The Gas Electron Multiplier [28, 25] is a 50 μm thick insulating kapton foil, clad on each side with a thin copper layer (5 μm) and chemically perforated with a high density holes. According to the standard techniques, the shape of the holes is bi-conical with a 70 μm external diameter and 50 μm internal diameter. The holes are the multiplication regions of the detector: the electrons produced by ionizing radiation in gas mixture drift toward the GEM and enter the holes. Once applied a voltage difference ($300 \div 500\ V$) between the two copper layers, a very high electric field ($\sim 100\ kV/cm$) is generated allowing electrons to produce avalanches. The GEM is manufactured according to conventional photolitographic methods. Two identical masks are produced and aligned on the two faces of the commercially available copper clad kapton foil. Exposing the foil to UV lights, the pattern of the masks is transferred to the foil. The holes are then opened by a kapton solvent using the copper as mask.

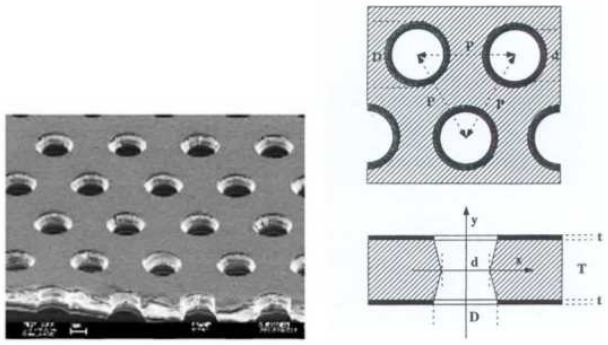

Figure 4.1: A GEM foil seen at the electron microscope (left) and the cross section of the geometry of GEM foil and the bi-conical shape of the holes (right).

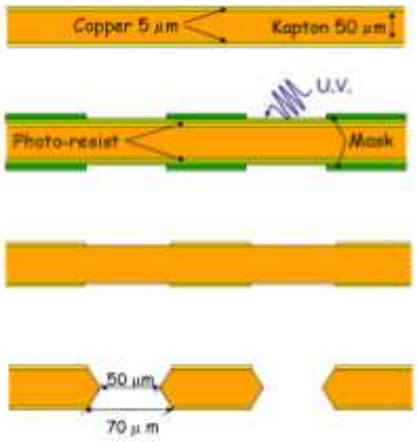

Figure 4.2: GEM manufacturing technology. From the top: commercially available copper clad kapton foil; the double mask alignment and the photolitographic process; copper etching by chemical solution; kapton etching using the copper layer as masks.

4.2.1 Hole diameter

Besides the HV applied across the GEM hole the gain of the GEM depends on the hole diameter. In general a reduction of the hole diameter corresponds to an increase of the gain. Fig. 4.3 shows the correlation between the effec-

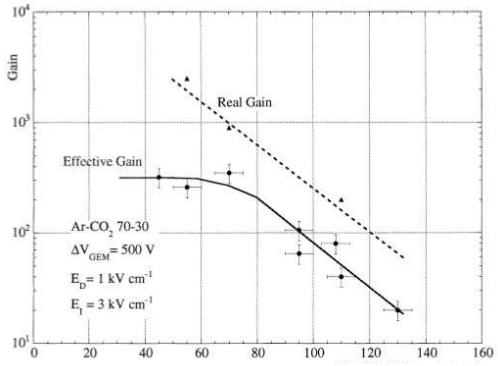

Figure 4.3: Effective and real gain as a function of hole diameter

tive GEM gain and the hole diameter [24], [26]. Below $70\mu m$ a saturation effect appears. The dashed line is obtained measuring all the currents of the detector for three diameters. The difference bewteen the two curves is due to the losses of electrons on the bottom GEM electrodes. It is worth notice that the saturation effect reduces the dependence of the detector gain from the precision of the GEM manufacturing process.

4.2.2 Hole pitch

The hole pitch affects the gain characteristic if combined with the hole diameter, since they appear into the expression of the optical transparency (the ratio of the open area to the total one): $\pi D^2/2\sqrt{3}P^2$ (Fig. 4.2). The electron transparency is strictly related to the optical transparency and it gives a measurement of the electrons lost crossing the multiplication region. Once fixed a diameter, the smaller is the hole pitch, the higher is the electron transparency.

4.2.3 Hole shape

During the avalanche process, electrons and ions can be collected on the insulating kapton surface (charging-up). The effect is a small increase of the electric field and consequently of the gain. The hole geometry which

minimize this effect is the cylindrical shape. Since during the production of cylindrical holes some defects can be created reducing the production yield, the bi-conical shape is a good compromise between the production yield and the charging-up effect.

4.3 The single GEM detector

A single GEM detector is formed by a GEM foil placed between two electrodes that act as cathode and anode. The typical distances between the electrodes are of the order of few millimeters. When a charged particle

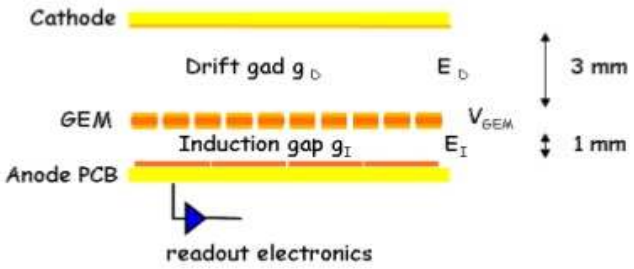

Figure 4.4: Cross section of a single GEM detector.

crosses the detector, electrons are produced into the drift gap (Fig. 4.4) and they move toward the GEM foil, following the drift field (E_D) lines. The electrons are focused into the holes where they generate avalanches. Some electrons hit the bottom side of the GEM, while the remaining ones, since an electric field (E_I) is set up between the bottom side of the GEM and the readout plane, drift through the induction gap: they are collected on the anode plane, inducing a signal during their motion. The readout plane is a simple printed circuit board (PCB) that can be structured according to the experimental needs.

4.3.1 The drift gap

The drift gap is the volume of the detector where primary electrons are produced and addressed into the holes. The thickness of the gap is chosen in order to ensure a high particle detection efficiency. Usually, with standard Argon gas mixtures, a 3 mm wide drift gap ensures the full efficiency of the detector. The number of ion-electron pair increases in wider gaps and

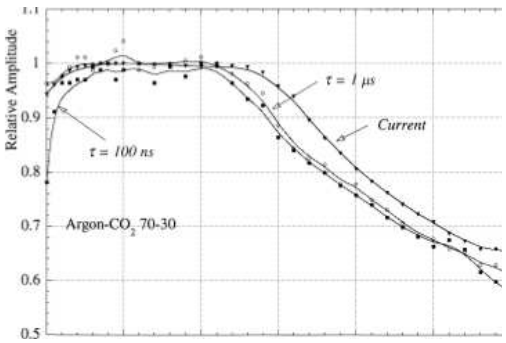

Figure 4.5: Collection efficiency as a function of drift field measured intagrating current

consequently pile-up effects raise up. As already said, the drift field make electrons enter the holes. Measurements in Ar:CO_2 70 : 30 of relative signal gain amplitude as a function of drift fields reveal a maximum efficiency for $1 < E_D < 2\ kV/cm$. In Fig. 4.5 this measurement is shown: the relative signal amplitude is obtained from current and pulse height measurements with two shaping time (100 ns and 1 μs). The drop in the region $E_D < 0.5\ kV/cm$ is due to a small drift velocity of electrons and consequently to recombination effect. For $E_D > 2\ kV/cm$ the field increases and the electrons are mostly collected on the upper side of the GEM.

4.3.2 The induction gap

The induction gap is the volume of the detector where signals are induced on the anode by the drifting electrons. Signal amplitude in a GEM is proportional to the ratio of the electron drift velocity to the gap thickness. An induction gap too small ($< 1\ mm$) could lead to mechanical oscillations which in turn would cause electrical instability with possible discharges in the induction gap. The induction field has to extract the electrons from the holes and to make them drift toward the anode. Not all the electrons are extracted from the holes: some of the exiting electrons are collected on the bottom side of the GEM, where a current is measured. In Fig. 4.6 currents on the electrodes of a single GEM are reported as a function of induction field. The drift field was set up to 1 kV/cm. I_B is the current on the bottom electrode of the GEM foil, I_T on the top side of the GEM, I_S is the current on the pads, I_{TOT} is the sum of currents. When the induction field is below 1 kV/cm, the electrons are all collected on the bottom side of the GEM.

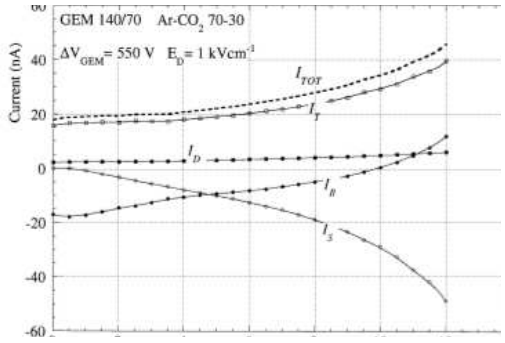

Figure 4.6: Current sharing between electrodes in the single GEM detectors as a function of the induction field for $E_d = 1\neg\text{ffl}kV/cm$

Increasing the field the electrons induce signals on the anode. Usually the value of induction field chosen is the point where $I_B = I_S$ (*charge sharing*) that in Fig. 4.6 is $E_I \simeq 5\ kV/cm$. The induction field shouldn't be chosen over 8 kV/cm in order not to give rise to discharges.

4.3.3 The GEM gain

The voltage applied to the metal sides of the GEM detector generates a high electric field into the holes. The *intrinsic gain* depends only on ΔV_{GEM}. This value can reach 10^3. But in order to compute the *effective gain* of a GEM, *collection efficiency* ε_{coll} and *extraction fraction* f_{extr} have to be taken into account. The first is defined as the ratio of the electrons entering the holes to the electrons produced by the m.i.p.[1] and it should be kept around 80%. This efficiency can be tuned by changing electric drift field. The *extraction fraction* is defined as the number of electrons extracted divided by the number of electrons produced in the avalanche region (holes). Because of previous considerations, this value should be ketp around 50%. The *effective gain* for a single GEM can be so computed:

$$G_{eff} = G_{intr} \cdot \varepsilon_{coll} \cdot f_{extr} \tag{4.1}$$

with

$$G_{intr} \propto e^{\langle\alpha\rangle V_{GEM}} \tag{4.2}$$

where α is the mean value of the Townsend coefficient along the path inside the holes. Using the typical values for G_{intr}, ε_{coll} and f_{extr} in eq. 4.1, we

[1]Minimum Ionizing Particle

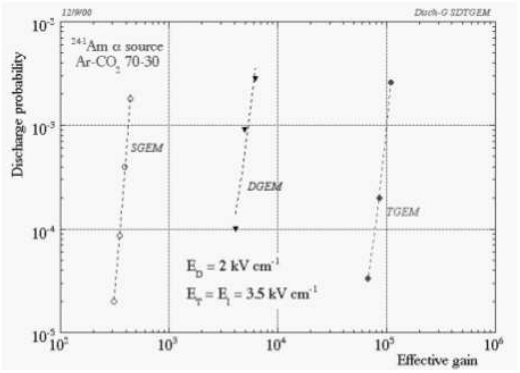

Figure 4.7: Discharge probability as a function of the gas gain for single, double and triple GEM in Ar:Co_2 70 : 30 gas mixture.

would obtain $G_{eff} = 10^3 \cdot 0.8 \cdot 0.5 = 400$. So the effective gain of a single GEM detector is of the order of $10^2 \div 10^3$. A way to increase the gain could be to increase the ΔV applied to the metal sides of the GEM. But working with high voltages is not safe for the detector because of the discharges. Another way to increase gain is assembling more than one GEM foil in cascade at close distance to each other.

4.4 Triple GEM

A triple GEM is otained with three GEM foils in cascade between the anode and the cathode (Fig. 4.8), allowing to reach higher gain with lower discharge probability with respect to single GEM (Fig. 4.7). With the insertion of three GEM foils between the electrodes, the number of gas gaps raises up to four (Fig. 4.8). The central gaps are called *transfer gaps*. The choice of the electric field and of the thickness for the *drift gap* and the *induction gap* follows the same consideration previously mentioned. The electric field E_T in this region combines the tasks of the drift field and of the induction field, since it has to extract the electrons from the holes of the above GEM foil and to focus them into the holes of the underlying GEM. As shown in Fig. 4.9, the induced current on the anode plane has a plateau for $3 < E_t < 4\ kV/cm$. For values of E_T lower than $3\ kV/cm$, the current drops because of the low extraction efficiency, while for $E_T > 4\ kV/cm$ we have a loss of collection efficiency for the underlying GEM. The thickness of the transfer gap must be chosen taking into account that a m.i.p. makes ion-electron pairs in all the gaps. If the transfer gap is quite wide (i.e. larger than 2 mm), the

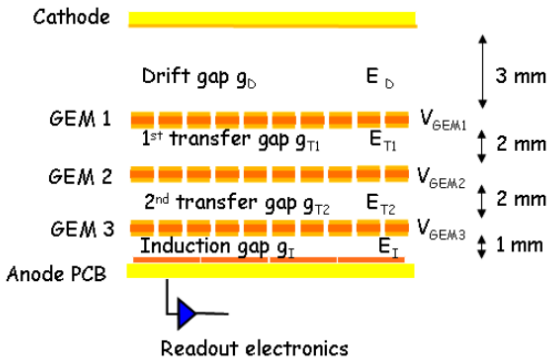

Figure 4.8: Cross section of a triple GEM

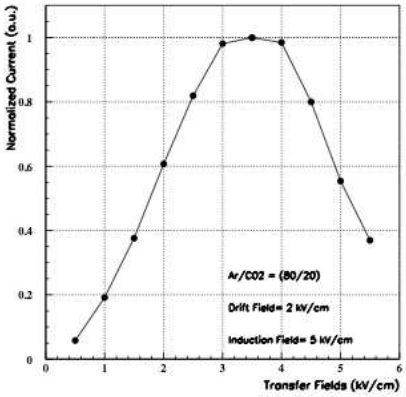

Figure 4.9: Induced current on the anode plane as a function of transfer field for Ar:CO_2 80 : 20 gas mixture. $E_D = 2\ kV/cm$, $E_I = 5\ kv/cm$.

electrons produced here could induce a signal discriminated by the front-end electronics, although they face less multiplication steps than the electrons produced in the drift gap. The signal so generated could anticipate the signal originated in the drift gap. This effect is called *bi-GEM effect*.

4.4.1 The triple-GEM gain

As in eq. 4.1, also for a triple-GEM the *effective gain* can be expressed as a function of the *intrinsic gain* of the three GEM foils. Since the *extraction efficiency* and the *collection efficiency* differ from gap to gap because of different electric fields, the gain is expressed as follows (taking into account eq. 4.2):

$$\begin{aligned} G_{eff} &= \prod_{k=1}^{3} \left(G_{intr}^{k} \cdot \varepsilon_{coll}^{k} \cdot f_{extr}^{k} \right) \\ &\propto \prod_{k=1}^{3} \left(e^{\langle \alpha^k \rangle V_{GEM}^{k}} \cdot \varepsilon_{coll}^{k} \cdot f_{extr}^{k} \right) \\ &\propto e^{\sum_k \langle \alpha \rangle V_{GEM}^{k}} \prod_{k=1}^{3} \left(\varepsilon_{coll}^{k} \cdot f_{extr}^{k} \right) \end{aligned} \tag{4.3}$$

where the k index refers to the GEM foils. Eq. 4.3 suggests that the gain depends on the sum of the the voltage difference applied on the GEM foils. In order to increase the triple-GEM gain, it is better to set higher voltage on the first GEM foil: this reduces discharge probability since the lower gaps are thinner. Optimal configuration is (Fig. 4.8)

$$V_{GEM1} \gg V_{GEM2} \geq V_{GEM3} \tag{4.4}$$

4.4.2 Time performance

The time perfomance of a GEM-based detector depends on the statistics of cluster produced in the drift gap. The expression for the space-distribution of the arrival times on the first GEM for the j-th cluster is ([31])

$$A_j^{\bar{n}}(x) = \frac{x^{j-1}}{(j-1)!} \bar{n}^j e^{-\bar{n}x} \tag{4.5}$$

where $\bar{n}$ is the average number of cluster created per unit length. The probability distribution of the arrival times on the first GEM can be written as function of the drift velocity v_d:

$$P_j(t_d) = A_j^{\bar{n}}(v_d t_d) \tag{4.6}$$

Gas mixture	$v_d\ (E_D)(mm/ns)$	$\bar{n}/mm$	$\sigma_1\,(t_d)\,(ns)$
Ar:CO_2 (70 : 30)	0.045	3.97	5.59
Ar:CF_4 (80 : 20)	0.119	4.61	1.82
Ar:CF_4 (85 : 15)	0.103	4.27	2.27
Ar:isoC_4H_{10} (80 : 20)	0.049	5.32	3.84
Ar:isoC_4H_{10} (85 : 15)	0.044	5.00	4.54
He:CO_2 (70 : 30)	0.028	1.99	17.94
He:CO_2 (80 : 20)	0.031	1.59	20.29
He:CO_2 (90 : 10)	0.029	1.18	29.22
He:iC_4H_{10} (70 : 30)	0.034	4.21	6.99
He:iC_4H_{10} (80 : 20)	0.031	3.08	10.47
He:iC_4H_{10} (85 : 15)	0.029	2.51	13.74
He:iC_4H_{10} (90 : 10)	0.025	1.95	20.51

Table 4.1: Summary table of some gas mixture properties provided by MAGBOLTZ and HEED with the intrinsic time resolution.

The time detection is usually the time of arrival of the closest electron to first GEM foil ($j = 1$). In this case the expression of eq. 4.6 reduces to

$$P_1\,(t_d) = \bar{n} \cdot e^{-\bar{n} v_d t_d} \tag{4.7}$$

Equation 4.7 allows to define the intrinsic time resolution of the detector if the first cluster is always detected:

$$\sigma_1\,(t_d) = \frac{1}{\bar{n} \cdot v_d} \tag{4.8}$$

This equation suggests that choosing a fast gas mixture with a high primary ionization implies a improvement of the time performance of a GEM detector. It is worth notice that intrinsic time resolution is a lower limit. Other effects arise in the particle detection, such the limited collection efficiency, the fluctuation of the gas gain (whereby the value of the gain can be very low) and the finite threshold of electronics: these effects can produce a signal induced by the first cluster that cannot be discriminated without piling-up to signals induced by other clusters. This represents the main contribution to the detector time resolution, but it can be avoided using a fast gas mixture which ensures a large *collection efficiency* and a high detection efficiency of the first cluster.

4.4.3 The signal formation

The signal in a GEM is completely induced by the motion of electrons in the induction gap. The current I_k induced on electrode k by a charge q drifting with $v_d(E_I)$ velocity can be expressed using Ramo's theorem [32]

$$I_k = -\frac{q\vec{v}_d(x) \times \vec{E}_k(x)}{V_k} \tag{4.9}$$

with $\vec{E}_k(x)$ is the electric field created raising the k electrode to the potential V_k. If $V_k = 1\ V$ we obtain

$$I_k = -q\vec{v}(x) \times \vec{E}_k^w(x) \tag{4.10}$$

with $\vec{E}_k^w(x)$ called the *weighting field*. According to simulations both the $\vec{E}_k^w(x)$ and $\vec{v}_d$ are practically constant in the induction gap. For this reason the signal induced by an electron drifting toward a GEM anode is expected to be rectangular shaped in the nearest pad. The width is dependent on the time spent by the electron to cross the induction gap:

$$i = -\frac{q}{t} = -\frac{qv_d}{x} \tag{4.11}$$

where x is the thickness of the gap.

4.5 Large GEM

CERN, where GEM technology was born, is the main producer of GEM foils. The size of the foils is actually limited to $450 \times 450\ mm^2$ for two reasons:

- The material for GEM foil is the Novaclad G2300 from Sheldahl. The polymide kapton foil is cladded on both sides with thin ($\leq 5\ \mu m$) copper layers. This material is usually provided in 457 mm wide rolls.

- The GEM are manufactured according to a photolithographic process. The copper layers are UV-exposed in order to transfer on them the hole pattern from two transparent masks placed on both sides of the foil. Then the foil are etched in an acid bath. The alignment of the masks on both sides of the GEM foil must have a precision up to few μm otherwise deformed holes are produced. The present dimension of the foil is considered a limit to preserve the homogeneity and the quality of the hole geometry. Requests for large GEM imply modification of the standard manufacting procedure.

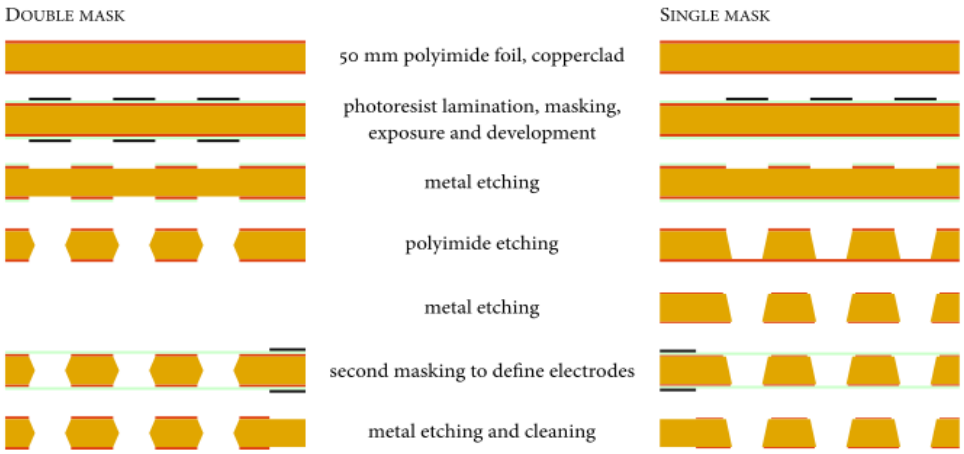

Figure 4.10: Schematic comparison of double-mask (left) and single-mask (right) procedures.

4.5.1 Single-mask procedure

In order to avoid masks misalignement, a single-mask procedure was developed by CERN ESTDEM workshop together with Gas Detector Development (GDD) group of CERN. A photoresist layer is laminated on both sides of the foil; a lithographic mask with the hole pattern is placed on the top layer and exposed to UV light. The top metal is etched while the bottom layer is protected. The polymide is etched from the top, and it is used as mask for the etching of the bottom side of the foil (Fig. 4.10).

4.5.2 Etching

Polymide etching [33] was traditionally done in a basic aqueous solution containing ethylene diamine and potassium hydroxide (KOH). The potassium hydroxide has a isotropic etching characteristic, removing the material in contact at the same rate in all directions. The ethylene diamine has anisotropic etching. The result of the two actions is the production of conical holes. The two etchants are necessary to reach a good aspect ratio (*depth/width* of a hole), that can be handled keeping under control the composition and the temperature of the liquid. Optimized parameters allow to have holes $90 - 45\ \mu m$. If the electrodes are not protected in the etching process, they will be subjected to the same process. Hence they will be slimmed to half their original thickness or less. Moreover a clearance arises around the edge

of the hole in the polymide. This clearance is called *rim* and it degrades time stability of the gain. To minimize this effect, the thickness of the electrode should be kept smaller even if it can be completely avoided protecting the metal with a *galvanic protection* or *electrochemical protection*. In the first case the metal is covered by a layer not attacked by the etchant. The second case, more successful, consists to give the top electrode few volts negative potential with respect to the bottom electrode and to the walls of the etching bath. The top electrode becomes inert to the reactions.

4.6 The prototype of the CGEM

The Inner Tracker for KLOE-2 experiment must cover as much as possible the region between the beam pipe and the inner wall of the Drift Chamber. For this reason the cylindrical geometry seems to be the best shape for it. The idea of a cylindrical GEM was developed by G. Bencivenni and his team at LNF [34], [35], [36]. Preliminary studies were perfomed with a prototype built in 2007. The GEM foils were manufactured by the CERN EST-DEM workshop. The propotype has similar dimensions to those of the first layer of the IT: the diameter is 300 mm while the active length is 352 mm because of the unavailability, at that time, of large GEM foils. Each layer of the cylindrical GEM is for this reason realized joining three identical foils ($352 \times 320\ mm$). The thickness of the gaps were chosen to be $3/2/2/2\ mm$ referring to drift/transfer1/transfer2/induction. The cathode is the inner layer (Fig. 4.11). Each layer (Fig. 4.12) is realized gluing three foils ($352 \times 320\ mm^2$) to

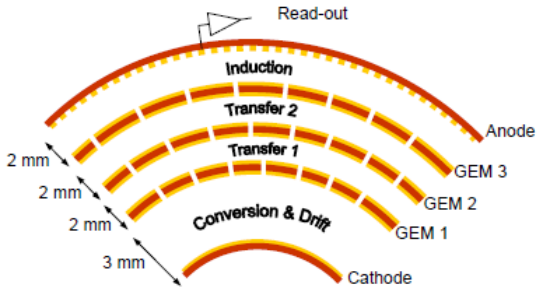

Figure 4.11: The cross section of a cylindrical triple-GEM

obtain a single large foil. Each foil has independent high voltage sectors (20) in order to limit the capacitance and the energy released through the GEM holes in case of discharges. The epoxy (araldite) was applied along the short

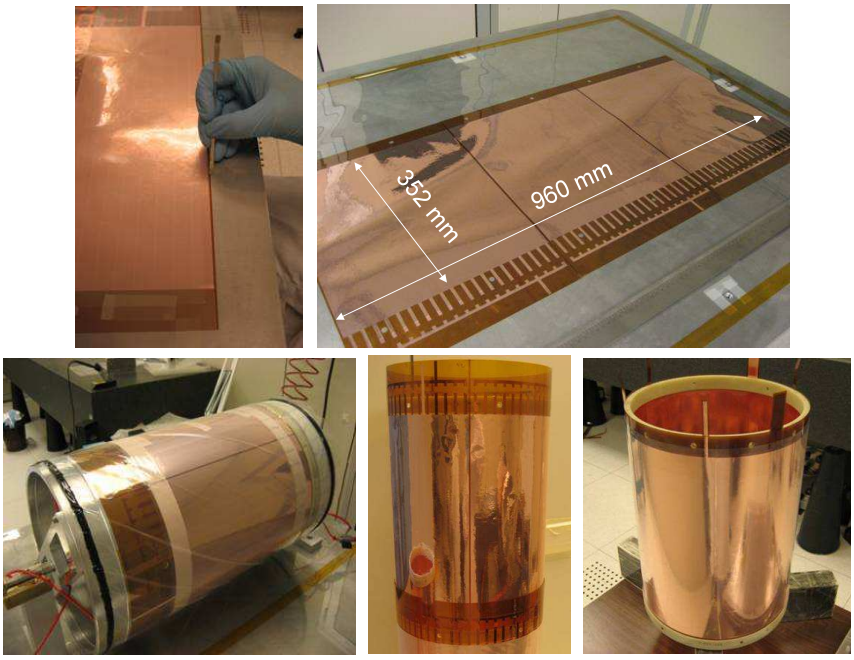

Figure 4.12: The steps of the construction of the CGEM prototype.

side of the GEM foil on a 3 mm wide region. Then the large foil is bent on an aluminium mould coated with a very precisely machined 400 μm thick Teflon film. The mould with the GEM foil is inserted in a vacuum bag: the Venturi system provides a uniform pressure of 0.8 kg/cm^2 over the whole cylindrical surface. Two cylindrical fiberglass anular rings are glued on the edges of the electrodes working as spacers and as mechanical support for the detector. Once ended the gluing procedure, the cylindrical foil can be extracted from the mould thanks to the low friction Teflon surface. Cathode and anode are realized in a very similar way. The cathode is realized as unique polymide foil (100 μm thick) cladded with 18 μm on the internal surface. The mechanical supports are some annular flanges made of Permaglass (G11) that host the inlets and outlets for gas. The anode readout is formed by three foils with the readout copper and the ground. The stripped surface and the ground surface are placed on the opposite faces of two polymide foils, staggered and glued togheter. The strips end-up in polimyde flaps, grouping 32 strips where the FEE is plugged with ZIF connectors. The pitch of the strip is

650 μm, with a $\sigma = 650/\sqrt{12} \simeq 200$ μm spatial resolution when equipped with a digital readout. In the flaps the pitch is reduced to 500 μm. Once the layers are ready, they are extracted from the mould using a PVC ring. To assembly the cylindrical triple-GEM a dedicated tool was realized: the Vertical Insertion System. The electrodes are fixed on two aluminium plates aligned on vertical axis and they can be pulled down with a very precise linear bearing equipment. This way an electrode can be inserted into another one without damaging it. The cylindrical triple-GEM was sealed on both sides, mounted on a support system providing a longitudinal tension of 200 g/cm measured by a load cell.

4.6.1 Materials

The materials chosen to build GEM were largely tested and validated in high rate environment and for different gas-mixture. With respect to the prototype, the Inner Tracker will have some modifications. The most relevant is the presence of a very light honeycomb carbon fiber cylinder (CFC) on which the anode circuit will be glued (*embedded-anode*). The GEM foils will be realized with new single mask procedure and they will be glued with a two components epoxy. The anode will be formed by $X - V$ strips. The table 4.2 reports the materials that will be used in the construction of the detector. while in table 4.3 are reported the contributions to material budget of a CGEM.

4.6.2 Quality controls

The quality control differs according to the component under test. For the GEM foils, a first check is performed at CERN: a voltage difference of 600 V is applied and leak currents are measured. The leak currents cannot be larger than 1 nA. This test takes place in a clean room. A cleaning of the GEM can be done with a light nitrogen flush that is able to gently remove dust. After this, an optical inspection must be made in order to find possible macroscopic damaged areas. This inspection will be performed by a microscope equipped with a digital camera. No more than 1 defect/mm^2 is allowed. The HV test is done inside a gas tight box flushed with Nitrogen, in order to reduce the humidity percentage under 10%. The HV is applied to each sector through a 500 $M\Omega$ limiting resistor, in order to avoid damages due to discharges. The maximum current in the power supply is set to 100 nA. The HV is slowly increased according to the following procedure:

- from 0 to 400 V with 50 V steps of 20 s

Material	**Details**	**Supplier/ Manufacturer**
Exposy glue	Araldite AY103+HD991	Ciba Geigy
(2 comp.)	Ciba 2012 (for fast applications)	Ciba Geigy
Annular frames	3/2/2/1 mm thick Permaglass	Resarm Itd (B)
CFC support	CF(250 μm)-Nomex(3 mm)-CF(250 μm)	Riba srl (I)
SF support	8 mm thick Permaglass annular-flange for FEE/HV/gas-piping location	Nuova Saltini (I)
GEM foils	50 μm thick kapton, $3-5$ μm Cu; 70 μm hole diam., 140 μm hole pitch	EST-DEM-CERN Workshop
Cathode	$3-5$ μm Cu on a 50 μm thick kapton	EST-DEM-CERN
Anode readout	$3-5$ μm Cu on a 100 μm thick kapton with $X-V$ strips-pad patterned	EST-DEM-CERN
Gas pipes	4 mm out.-diam. brass tube	LNF-Workshop
Gas outlet	6 mm out.-diam. rilsan Pa11 tube (not hygroscopic)	Tesfluid srl (I)

Table 4.2: Materials used to assemble the CGEM

Component	**times $\times$ material (X_0)$\times$ quantity**	**% of X_0**
3 GEMs	Copper: 6×2 μm Cu ($X_0 = 14.3$ mm) $\times 0.8$	0.067
	Kapton: 3×50 μm kapton ($X_0 = 286$ mm) $\times 0.8$	0.042
		Total: 0.109
1 Cathode	Copper: 1×2 μm Cu $\times 1$	0.013
	Kapton: 1×50 μm kapton$\times 1$	0.017
		Total: 0.030
1 Readout	Copper: 1×2 μm Cu $\times 0.95$	0.013
anode	Kapton: 2×50 μm kapton $\times 1$	0.034
		Total: 0.047
1 Shielding	Aluminum: 1×10 μm Al($X_0 = 89$ mm)$\times 1$	Total: 0.011
1 Honeycomb	NOMEX: 1×3 mm Nomex ($X_0 = 13125$ mm)$\times 1$	Total: 0.023
2 CF skins	CF: 2×250 μm CF ($X_0 = 250$ mm) $\times 1$	Total: 0.160
		Total: 0.380

Table 4.3: Material budget for a single cylindrical triple-GEM

- from 400 V to 500 V with 25 V steps of 60 s

- from 500 V to 600 V with 10 V steps of 2 min

The measured currents cannot overflow 1 nA and no more than 3 discharges can occur. Otherwise the test is repeated later on.
The readout is firstly tested at EST-DEM CERN Workshop. Here possible shorts between the strips are tested. Another validation test consists to measure the distance between the first and last strip at different positions: the maximum deviation cannot exceed 100 μm.
The annular frames are preliminary washed with isopropilic-alcohol. A carefully inspection to find and eliminate spikes and possible broken fibers is performed before and after the final cleaning, which is done in an ultra-sonic bath with demineralized water for 30 minutes. The frames are then dried in a oven at 40 $°C$ for 1 hour. The HV test is needed to proof their insulating power: they are placed bewteen two copper foils at a voltage difference of 4 kV within a clean box flushed with nitrogen. If sparks occur frames are flushed for about two hours and then tested again. In case of further sparks, the frames are inspected with a microscope.
A gas leakage test is performed on the completed CGEM. The CGEM is connected to a differential pressure device, to which is also connected a tight reference volume (same volume of the detector, gas leak $\ll$ 1 $mbar/day$). The CGEM and the reference volume are flushed in parallel with an overpressure of 5 $mbar$. The difference bewteen the two pressure is a measure of the gas leakage of the detector. The reference volume is useful to take into account atmospheric and temperature variations.

4.6.3 Electronics

The readout of the IT is composed by about 30000 XV strips. The length of the V strips differs according their position, so the parasitic capacitance will range between 1 and 50 pF making impossible to optimize the S/N ratio. This ratio can be improved installing the front-end electronics on the detector itself. One of the costraints deriving from KLOE DAQ is the 200 ns delay of the Level 1 trigger with respect to the Bunch Crossing: signals have to be stretched. In order to fulfill the requirements, a 64-channels front-end ASIC prototype was developed: GASTONE (Gem Amplifier Shaper Tracking ON Events). The chip is also equipped with a robust protection circuit to prevent damages caused by discharges in the detector. The GASTONE chip is a mixed analog-digital circuit, consisting of 64 channels followed by a digital section. The main features of GASTONE are the low input equivalent noise (ENC), the high modularity and the low power consumption. The

modularity was set to 64 channels: this is a compromise between the number of I/O lines and the reliability of the system, since the devices cannot be accessible without extracting the beam pipe. Once the signals are amplified and shaped, they are digitized and read out using both edges of a 50 MHz clock. The analog and the digital section have different power supply to avoid interferences. The I/O signals are implemented in the LVDS standard. The readout clock activates only in the download period (starting after the arrival of Level 1 trigger). Each channel of the analog section is made of four blocks:

- **A charge sensitive preamplifier**. In a GEM the input charge ranges from few fC to some tenths of fC. The amplifier should combine high charge sensitivity to low noise level. The amplifier is a common-source cascaded amplifiers with an active feedback network made of 150 fF capacitor and a PMOS transistor. The features of the integrated amplifier are summarized in Table 4.4.

- **Shaper**. The shaper provides semi-gaussian shaping for noise filtering and is characterized by a voltage gain of 4. The non-linearity is less than 3% with a supply current of 200 nA. The peaking time lies between 90 and 220 ns when the capacitance ranges between 1 and 50 pF. The charge sensitivity of the preamplifier-shaper system is about 23 mV/fC.

- **Discriminator**. The leading edge discriminator has a threshold between 0 and $\sim$ 200 fC when support current of 180 μA. It is AC-coupled to the shaper. The threshold spread is below 2% and an offset of $\sim$ 2.2 mV over the full range of the threshold.

- **Monostable**. The digitized signals are here stretched in order to be collected when the Level 1 trigger snaps. The pulse width can be tuned between 200 ns and 1 μs.

The digital section is composed by:

- **Readout Interface**. The digital section cares the storage of the discriminated signals. Once the signal from Level 1 trigger arrives, the signals are stored into a 96$-$bits register. The arrival of 50 MHz readout clock starts the download procedure (960 ns). The consumption power is about 40 mW.

- **Slow Control-SPI interface**. The Slow Control is managed by a SPI interface with a clock running at 1 MHz. Twenty-eight 8$-$bit registers

configure the chip functionality, set the DACs threshold and read four ADCs. Another ADC set and read the width of the monostable output pulse. The amplitude of the internal test pulse is set and read by a sixth ADC. The threshold is set to $\sim 3\ fC$ at power on.

The off-detector electronics is formed by:

- **GEO boards**. These boards provide full control on GASTONE chips: stting/reading GASTONE registers, testing different sections of the chain and downloading the 64 bits data when permitted by the Level 1 trigger. The data transmission between the chip and the GEO boards were implemented by LVDS connections, while communications with the Experiment Control System are provided by optical links. After a signal from Level 1 trigger, the GEO boards bring the trigger signal to the chips in order to load the registers and to start the readout running the 50 MHz clock.

- **CONCENTRATOR**. These boards manage the communications between the GEO boards and Slow Control, DAQ and Trigger. The trasmission from GEO boards to CONCENTRATOR starts 1.8 μs after the Level 1 trigger signal: it is the moment for the Level 2 trigger signal to be generated.

Feedback capacitance	150 fF
Feedback resistance	5 $M\Omega$ $I_{feed} = 300\ nA$
Transconductance (g_m)	6.4 mA/V
Gain	5 mV/C $C_{in} = 0\ pF$
Z_{in}	120 Ω up to 10^5 Hz
Non-linearity	$\leq 1\%(0 \div 30\ fC)$
ENC (erms)	800 $e_{rms} + 40\ e_{rms}/pF$
Supply Current	$\approx 350\ \mu A$

Table 4.4: Main features of the charge preamplifier

Chapter 5

The measurements on CGEM

5.1 X-ray test

The very first test of the prototype [21] was performed using a 5.9 keV X-ray gun. The prototype (Fig. 5.1 (left)) was flushed with a gas mixture Ar:iC_4H_{10}:CF_4 65/7/28 tested in current mode. A 10×10 cm^2 planar triple-GEM was placed in the same gas line and irradiated from a side opening of the gun (Fig. 5.1 (right)). The planar detector works as reference to account for possible gain variations due to changes in atmospheric variables. The CGEM was characterized measuring the relative gain with respect to the reference detector as a function of the electric fields in the GEM (Fig. 5.2), as discussed in the previous chapter. In the plots on the top of Fig. 5.2, electron transparency (related to the *focusing efficiency*) is shown as function of drift (left) and transfer fields (right), while on the third plot *charge sharing* between the anode and the bottom side of the GEM3 is reported. The sum of the two charges is also shown: no dependence from the induction field is observed. This test allowed to study uniformity of the CGEM over the 940 mm of its circumference. Excluding the sectors where the response is weaker (joins), the R.M.S of the values measured in Fig. 5.3 (left) is within 9%. A measurement of the induction gap thickness uniformity (Fig. 5.3 (right)) can be performed considering that the ratio between the current on GEM3 and the readout electrode depends only on the thickness of the induction gap. The results suggest that the detector was built with a good mechanical precision.

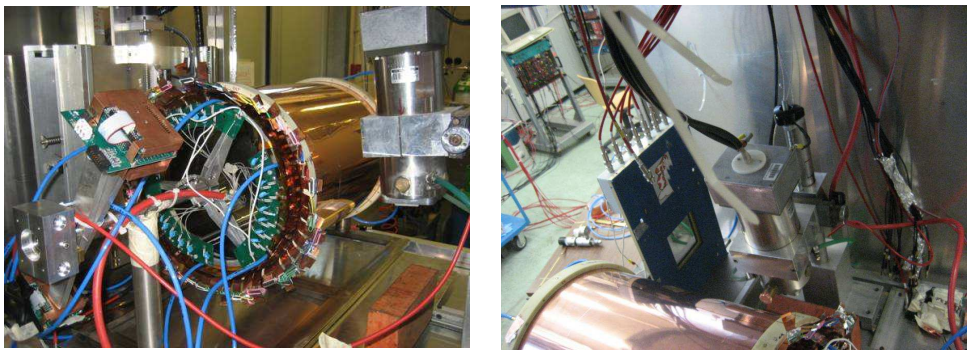

Figure 5.1: Experimental layout for X-ray test: the CGEM prototype (left) and the reference planar triple-GEM (right).

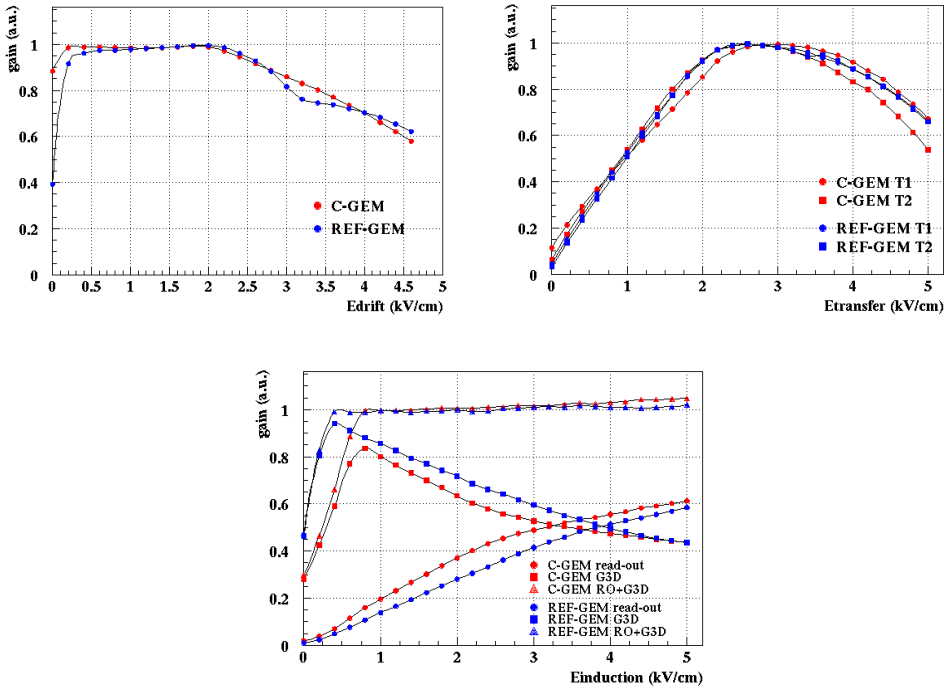

Figure 5.2: Relative gain as a function of drift field (top left), transfer fields T1 and T2 (top right) and induction field (bottom) of the CGEM with respect to the planar reference chamber. All the electric fields not involved in each measurement are kept at constant values.

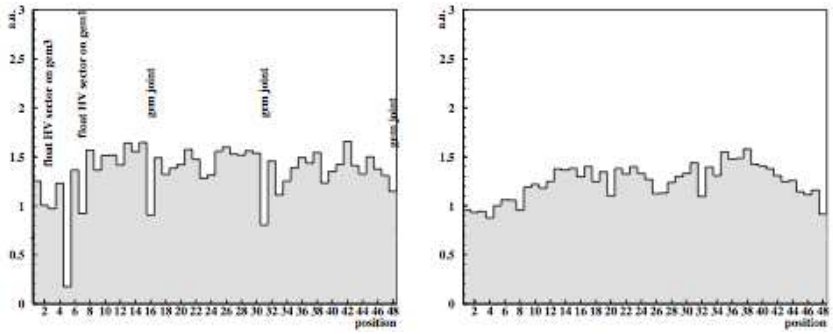

Figure 5.3: CGEM gain uniformity (left) and induction gap thickenss uniformity (right).

5.2 The test beam at the T9 area

The CGEM prototype was also extensively tested with the 10 GeV pion beam at the T9 area of CERN PS [37]. Two different readout devices were used: 128 channels were equipped with the GASTONE ASIC, while 96 channels with the CARIOCAGEM electronics. GASTONE is a custom chip developed to fulfill the power consumption and high integration requirements of the KLOE-2 experiment, while the CARIOCAGEM chip was developed for the LHCb Muon System GEM detectors: it is very fast (10 ns peaking time) with digital readout and it was used to measure the timing performance of the detector, using a 100 ps resolution TDC. The CGEM was flushed with a Ar:CO_2 70 : 30 gas mixture and operated with the following voltages: $V_{fields} = 1.5/2.5/2.5/4\ kV/cm$ and $V_{GEM} = 390/380/370\ V$ ($\sum V_G = 1140\ V$ corresponding to a gas gain of 2×10^4). The track position was measured with an external tracker based on ATLAS drift tubes with 30 mm diameter and 0.4 mm wall thickness. The wire diameter is 100 μm and they were operated in streamer mode with a gas mixture Ar:C_4H_{10} 40 : 60 at STP. The tracker is formed of two sets of longitudinal stations, each with 8 channel distributed on 3 planes and providing a measurement on y coordinate (Fig. 5.4). The CGEM was placed between the two stations. Only tracks with on-time hits in each of the 6 tracker planes have been used for the analysis. The contribution to the spatial resolution due to the external tracker was measured to be $\sigma_{tracker} = 140\ \mu m$. The setup also included a trigger built with a coincidence of three scintillators placed before and after CGEM. The reconstruction procedure had to take into account the fact that the measured

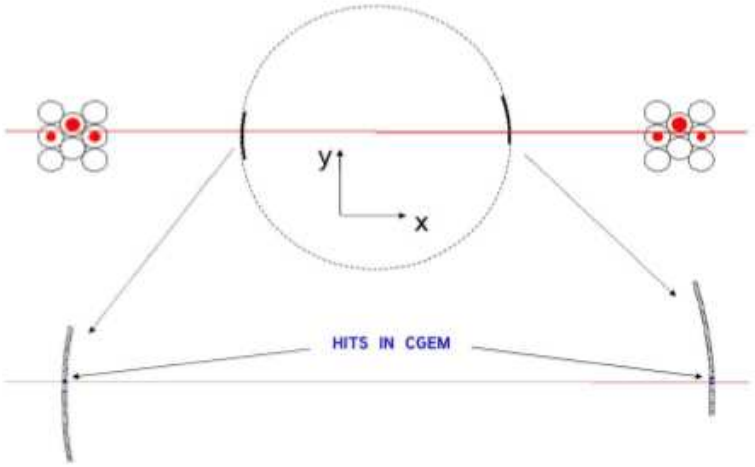

Figure 5.4: The setup tracker of the test beam at T9 area.

particles do not generally cross the detector along the radius of the cylinder (Fig. 5.5). An offset must be computed based on the impact position of the track in order to correct the reconstructed position. Moreover the clusters created along lines non parallel to the drift ones involve signals induced on a larger number of strips. The cluster size increases as function of y coordinate of the track. In Fig. 5.5 (left) we have the efficiency of the chamber measured

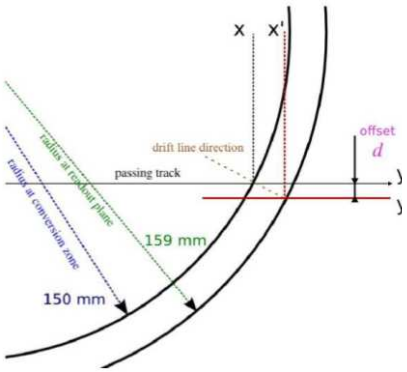

Figure 5.5: A scheme of the offset bewteen the passing track and the collection area on the readout.

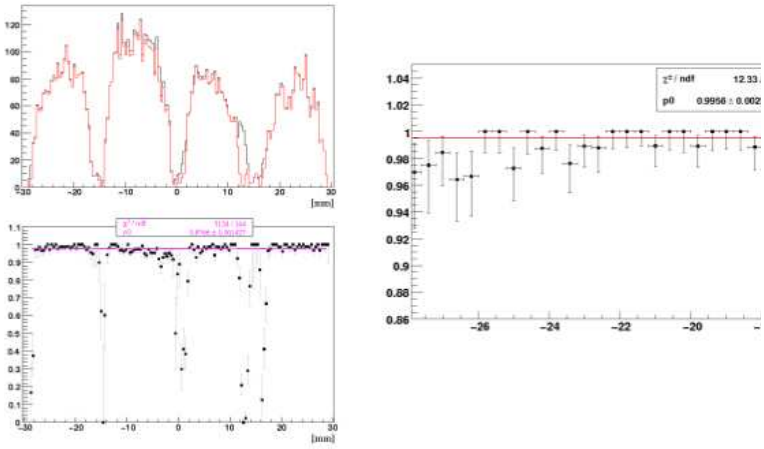

Figure 5.6: Top left: distribution of reconstructed (black) and measured (red) impact track postition; bottom left: efficiency as function of the impact track position; right: detail of the efficiency in a high statistic region.

for different position of the impact track with the GASTONE chip threshold set at 3.5 fC. The efficiency averaged over the whole equipped region is 97.7%. The low statistic point are related to a lack of reconstructed track in proximity of the walls of the drift tubes. An efficiency of 99.6% is obtained rejecting these points. Loss of efficiency are present also in the gluing zone of the small GEM foils: in the final detector designs, these regions account for less than 0.4% of the total GEM foil. This effect was investigated studying the time distribution provided by the CARIOCA-GEM chip. In the regular regions time distributions (Fig. 5.7 (left)) with 13 ns R.M.S. were obtained in agreement with the performance expected for the used gas mixture (Ar:CO_2 $70:30$, $v_{drift} = 7\ cm/\mu s$ at 2 kV/cm). In the joint region (Fig. 5.7 (right)) the R.M.S of the time distribution is 200 μs. In these areas the electrons follow distorted field lines to reach the anode (Fig. 5.8 (left)). In Fig. 5.8 (right) residuals of the cluster position with respect to the reconstructed track position are showed. The CGEM spatial resolution is obtained by the $\sigma_{tracker}$ and by the $\sigma_{residuals}$ since $\sigma_{GEM} = \sqrt{\sigma^2_{residuals} - \sigma^2_{tracker}} \simeq 200\ \mu m$ in good agreement with what expected from a digital readout of 650 μm pitch strips. In conclusion, the full scale prototype was safely operated at CERN PS with 10 GeV pion beam. This test validated the innovative idea of the fully sensitive cylindrical GEM detector, constructed with no support frames

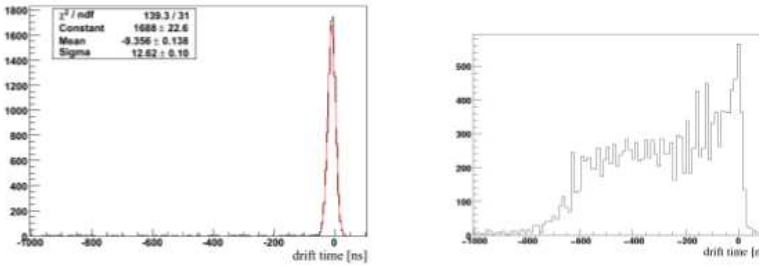

Figure 5.7: Time distribution in regular regions (left) and in the joint zone (right).

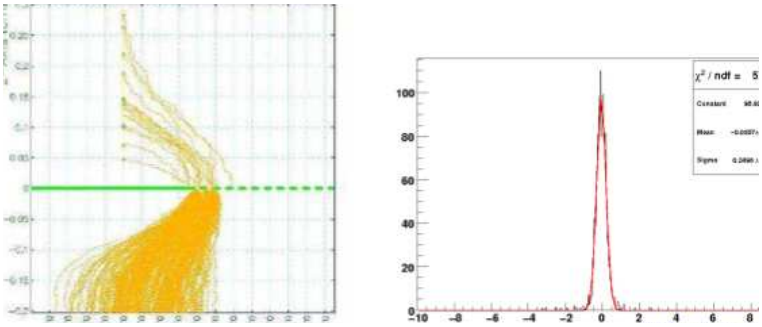

Figure 5.8: Field lines distortion in the gluing region simulated by GARFIELD (left) and CGEM resolution (right).

inside the active area. The material budget used in the construction of the CGEM prototype and the measured spatial resolution are fulfilling the inner tracker requirements.

5.3 Planar GEM for readout studies

A readout made of orthogonal strips ($X-Y$) cannot be used in a cylindrical anode: the strips in the $r-\phi$ plane couldn't be read out. A 2-D readout can be obtained using 650 μm pitch strips at an angle of 40° ($X-V$ layout, Fig. 5.9). The investigation of the possible problems related to this layout required a dedicated test. For this test a planar triple GEM (10×10 cm^2 active area) equipped with the $X-V$ readout and four planar triple GEM

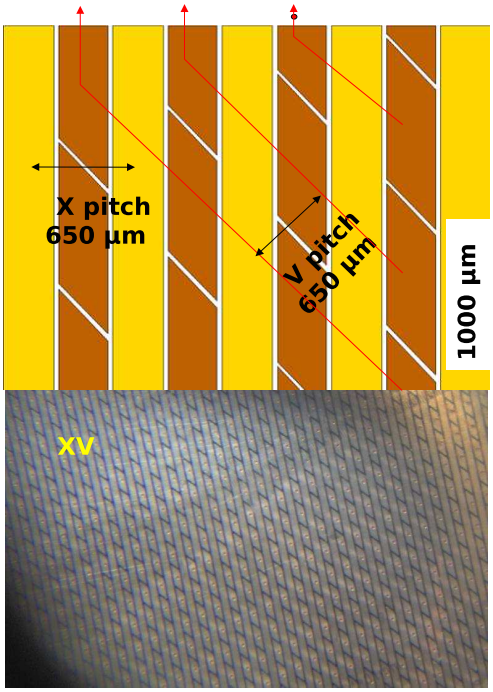

Figure 5.9: The $X - V$ readout

equipped with $X - Y$ readout were built. The behaviour in magnetic field of the new readout was studied using the $X - Y$ readout as reference.

5.4 Operation in magnetic field

The Inner Tracker for the KLOE-2 experiment will work in magnetic field, affecting the reconstruction procedure. In order to correctly reconstruct the tracks in the experiment, sistematic effects must be known *a priori*. Here follows a brief description of the effect of a magnetic field in a triple GEM.

5.4.1 The drift of electrons in magnetic field

When solving the equation of the drift motion for a charged particle, it is usually introduced a frictional force K so that

$$m\frac{d\vec{v}}{dt} = e\vec{E} + e\left[\vec{v} \times \vec{B}\right] - K\vec{v} \tag{5.1}$$

The ratio m/K has the dimensions of a characteristic time τ. Introducing the cyclotron frequency $\omega = (e/m)\,|\vec{B}|$ we can have an estimation of Lorentz effect, governed by the numerical value $\omega\tau$. Since the mobility is defined as $\mu = (e/m)\,\tau = |\vec{v}|/|\vec{E}|$, using $B = 1\ T$ we have [27]

$$\omega\tau = |\vec{B}|\mu \simeq \begin{cases} 10^{-4} & \text{for ions} \\ 1 & \text{for electrons} \end{cases}$$

This suggests that the effect is negligible for ions. The eq.5.1 reduces to

$$\frac{1}{\tau}\vec{v} - \frac{e}{m}\left[\vec{v} \times \vec{B}\right] = \frac{e}{m}\vec{E} \tag{5.2}$$

The equation for $\vec{v}$ can be solved writing $\omega_x = (e/m)\,B_x$, etc.. and expressing eq. 5.2 in the matrix form

$$\begin{aligned} \mathbf{M}\vec{v} &= \varepsilon \\ \mathbf{M} &= \begin{pmatrix} 1/\tau & -\omega_z & \omega_y \\ \omega_z & 1/\tau & -\omega_x \\ -\omega_y & \omega_x & 1/\tau \end{pmatrix} \end{aligned} \tag{5.3}$$

The solution is computed inverting $\mathbf{M}$

$$\begin{aligned} \mathbf{M}^{-1} &= \begin{pmatrix} 1+\omega_x^2\tau^2 & \omega_z\tau + \omega_x\omega_y\tau^2 & -\omega_y\tau + \omega_x\omega_z\tau^2 \\ -\omega_z\tau + \omega_x\omega_y\tau^2 & 1+\omega_y^2\tau^2 & \omega_x\tau + \omega_y\omega_z\tau^2 \\ \omega_y\tau + \omega_x\omega_z\tau^2 & -\omega_x\tau + \omega_y\omega_z\tau^2 & 1+\omega_z^2\tau^2 \end{pmatrix} \\ &\times \frac{\tau}{1+\omega^2\tau^2} \end{aligned} \tag{5.4}$$

where $\omega^2 = \omega_x^2 + \omega_y^2 + \omega_z^2 = (e/m)^2\,|\vec{B}|^2$. The drift velocity can be written

$$\vec{v} = \frac{e}{m}\tau|\vec{E}|\frac{1}{1+\omega^2\tau^2}\left[\hat{E} + \omega\tau[\hat{E}\times\hat{B}] + \omega^2\tau^2\left(\hat{E}\cdot\hat{B}\right)\hat{B}\right] \tag{5.5}$$

If the magnetic and the electric fields are orthogonal (i.e. $\vec{E} = (0,0,E)$ and $\vec{B} = (0,B,0)$), the eq. 5.5 reduces [27]

$$\begin{aligned} v_x &= -\frac{(e/m)\,\tau}{1+\omega^2\tau^2}\omega\tau|\vec{E}| \\ v_y &= 0 \\ v_z &= \frac{(e/m)\,\tau}{1+\omega^2\tau^2}|\vec{E}| \end{aligned} \tag{5.6}$$

If the fields are uniform, ω is a constant; τ is a characteristic time, so it doesn't change. The result is a constant velocity in the $x-z$ plane and a

constant angle with respect to the z axis: the Lorentz angle. The Lorentz angle is computed as

$$\tan \alpha_L = \frac{v_x}{v_z} = -\omega\tau = -|\vec{v}|\frac{|\vec{B}|}{|\vec{E}|} \tag{5.7}$$

and it is defined as the angle between the effective drift direction and the direction of the electric field where the charge moves.

5.4.2 The triple-GEM in magnetic field

A triple GEM has four gas gaps where the electric fields are mostly constant: so the conclusions made in sec. 5.4.1 must be taken into account. Let's consider the anode plane as the $x-y$ plane and the direction orthogonal to the GEM foils as the z axis. The eqs. 5.6 suggest that the presence of a magnetic field affects the drift motion of electrons produced by ionization in the gas, thus influencing the position reconstruction of primary particles. All the charged particles involved in the ionization process experience the Lorentz force and consequently two effects arise (Fig. 5.10):

- The area where signals are induced is shifted with respect to the position of the ionizing track
- The shift experienced by each primary electron depends on the position along the track where the pair is produced: this involves a larger spread of electrons and consequently a worse spatial resolution.

An estimation (at the 0^{th} order approximation) of the shift Δx of the electrons produced in the drift gap could be computed knowing $|\vec{v}\left(\vec{E}\right)|$ for each gas gaps of the triple GEM:

$$\begin{aligned} \Delta x &\simeq y_1 \tan \alpha_L \left(\vec{E}_i\right) + \sum_{i=2}^{4} \Delta y_i \tan \alpha_L \left(\vec{E}_i\right) \\ &= |\vec{B}| \cdot \left[y_1 \frac{|\vec{v}\left(\vec{E}_1\right)|}{|\vec{E}_1|} + \sum_{i=2}^{4} \Delta y_i \frac{|\vec{v}\left(\vec{E}_i\right)|}{|\vec{E}_i|} \right] \end{aligned} \tag{5.8}$$

where y_1 is the position in the drift gap where the ion-electron pair is produced and Δy_i is the thickness of the other gas gaps. As already said, the eq. 5.8 doesn't take into account signals induced by the primary electrons produced in the first transfer gap [1]. A preliminary value of Δx can be

[1] Signals induced by primary electrons produced in the second transfer gap and in the induction gap are not discriminated.

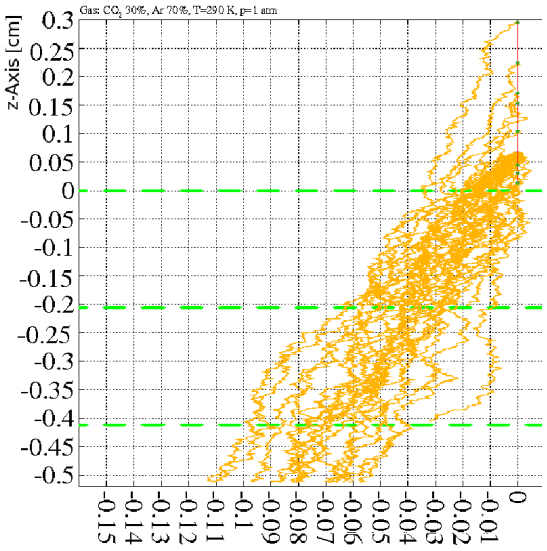

Figure 5.10: A simulation of the effect of the magnetic field on drifting electrons in a triple GEM filled with Ar:CO_2 70 : 30 gas mixture. The simulation is made with GARFIELD

obtained by simulations. A finite element method program, **ANSYS**, was used to build the chamber while **GARFIELD** (see appendix A) was used to simulate the electron drift behaviour.

5.5 Simulations of a triple GEM

5.5.1 GARFIELD

Preliminary studies of gaseous detector can be performed with GARFIELD [39], a computer program developed by R. Veenhof. GARFIELD computes and plots the electrostatic field, the drift lines of electrons and ions and the currents on the anodes resulting from the passage of a charged particle through the chamber. The program is meant for use with chambers that consist only of thin wires and infinite equipotential planes. Periodicity, magnetic fields and cylindrical geometry are allowed. GARFIELD cannot deal with three-dimensional structures. The properties of the gas mixtures are computed calling MAGBOLTZ [40], a program developed by S. Biagi, that numerically integrates the Boltzmann transport equation. We can obtain from MAGBOLTZ the drift velocity of electrons, the diffusion coefficients,

the Townsend and attachment coefficients as a function of electric field. If a magnetic field is set up, the program computes the Lorentz angle and other properties. In order to simulate the ionization processes, GARFIELD calls HEED [41], a program written by I. Smirnov: this program can compute in detail the energy loss of fast charged particles in gases and it can provide the number of clusters per *cm*, the cluster size distribution and the range and straggling of delta electrons. A GARFIELD code is composed by different sections dedicated to:

- the geometry of the detector (&CELL)
- the definition of a magnetic field (&MAGNETIC)
- the gas section, where the properties of the gas mixtures are computed (&GAS)
- find a compromise among the chamber layout, the fields and the working point of the detector (&OPTIMISE)
- show the field lines (&FIELD)
- the drift of electrons and to the avalanche processes (&DRIFT)
- the signals computation (&SIGNAL)

Some of these points are discussed in appendix A.

5.5.2 Simulation of the elementary cell of a GEM

A GEM foil is a plane with a high number of holes with dimensions very small with respect to the dimensions of the plane. So if we focus our eyes on a hole, the plane looks infinite. As already said, GARFIELD can periodically reproduce in the space a cell defined in the dedicated section. So a good strategy is to build an elementary cell and to ask GARFIELD to reproduce it to form an infinite plane. The **unitary** cell is the part of the GEM foil which can reproduce the whole foil by rototranslations (Fig. 5.11 (left)). But in this work we will define the **elementary** cell (Fig. 5.11 (right)) as the cell which reproduces the foil only by translating it. As shown in Fig. 5.11 the elementary cell is composed by four unitary cells. GARFIELD can interface ANSYS, MAXWELL and TOSCA to build the desired cell: each of these programs produces a map of the electric field and of the materials used. These maps are read by GARFIELD and used to build a cell for the simulations. The program used in the following work is ANSYS. Once built

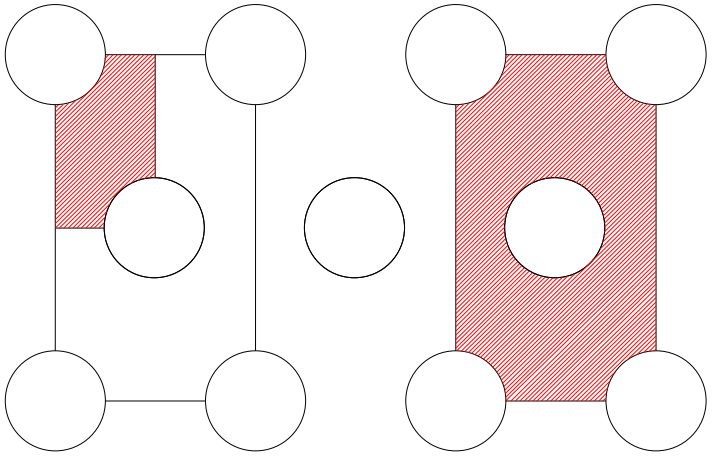

Figure 5.11: A representation of the **unitary** cell (left): the whole foil can be reproduced rotating and translating it. On the right a represantation of what is called **elementary** cell.

the GEM plane, the gas mixture properties are computed in an electric field range properly set by the user. The electric field lines are computed and they can be shown (Fig. 5.12). GARFIELD makes electrons drift following their position and computing the drift velocity at each step. It uses three methods to compute the electron drift (see appendix A). When an electron reaches a volume of the chamber where the Townsend coefficient is larger than zero, the avalanche gets started. The simulation of an avalanche computed by GARFIELD shows some problems since the value of the *intrinsic gain* is very different from the measured values. This is mainly due to two effects not simulated by GARFIELD:

- the charging-up effect (sec. 4.2.3)

- the Penning effect

These effects (one depending on the hole geometry and the other depending on the gas mixture) give a contribution to the gain of the detector. Work is in progress to include Penning effect in the simulations, while a work for the simulation of the charging-up effect was presented by the CERN group.

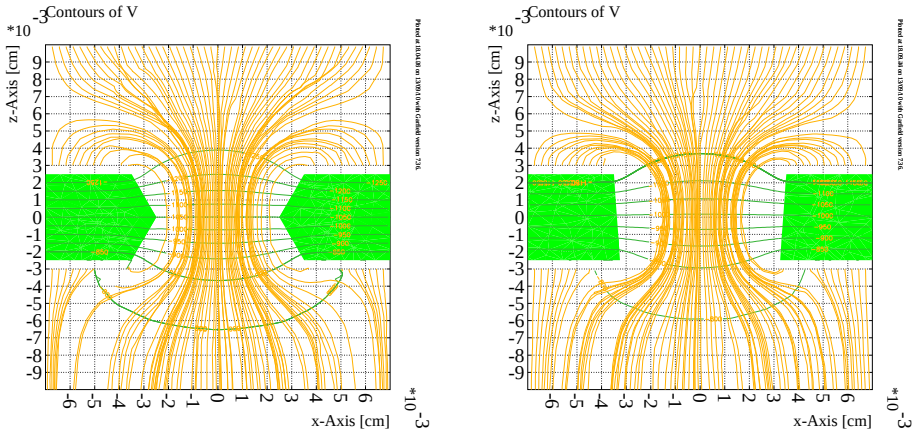

Figure 5.12: GARFIELD output of the electric field lines (yellow) and equipotential lines (dark green) close to the hole for the standard hole geometry (left) and the new geometry (right) ($E_D = 1.5\ kV/cm$ and $E_I = 5\neg\text{ffl}kV/cm$).

5.5.3 Simulation of the gas mixtures

The choice of the gas mixture for a detector depends on its properties. A sample of properties of gas mixtures are shown in Fig. 5.13, where the magnetic field was set up to 0.5 T (as in the KLOE experiment). From the plot of the Lorentz angle we could estimate the mean displacement of the electrons in a GEM filled with Ar:$C0_2$ 70 : 30 working in 0.5 T using eq. 5.8, where the y_1 of the equation could be fixed, at the 0^{th} order, in the middle of the drift gap. This leads us to have[2] $\Delta x \simeq 1047.9\ \mu m$. A better way to give a value to Δx is to simulate the drift of electrons towards a triple GEM and to study their distribution on the anode plane.

5.5.4 Simulation of a triple GEM

The difference bewteen an elementary cell of a single GEM and the one of a triple GEM is its extension in the z direction: in a single GEM we have a kapton foil, two copper layers and two gas gaps, while in a triple GEM we have three GEM foils, six copper layers and four gas gaps. Once built it, we can ask GARFIELD to reproduce it. The displacement of electrons can be evaluated looking at the distribution of electrons on the anode plane at the end of their drift. The process can be easily described as follows:

- a m.i.p. ionizes some gas atoms along its path: GARFIELD gives the

[2]The values of the gaps thickness used are 3 mm/2 mm/2 mm/1 mm

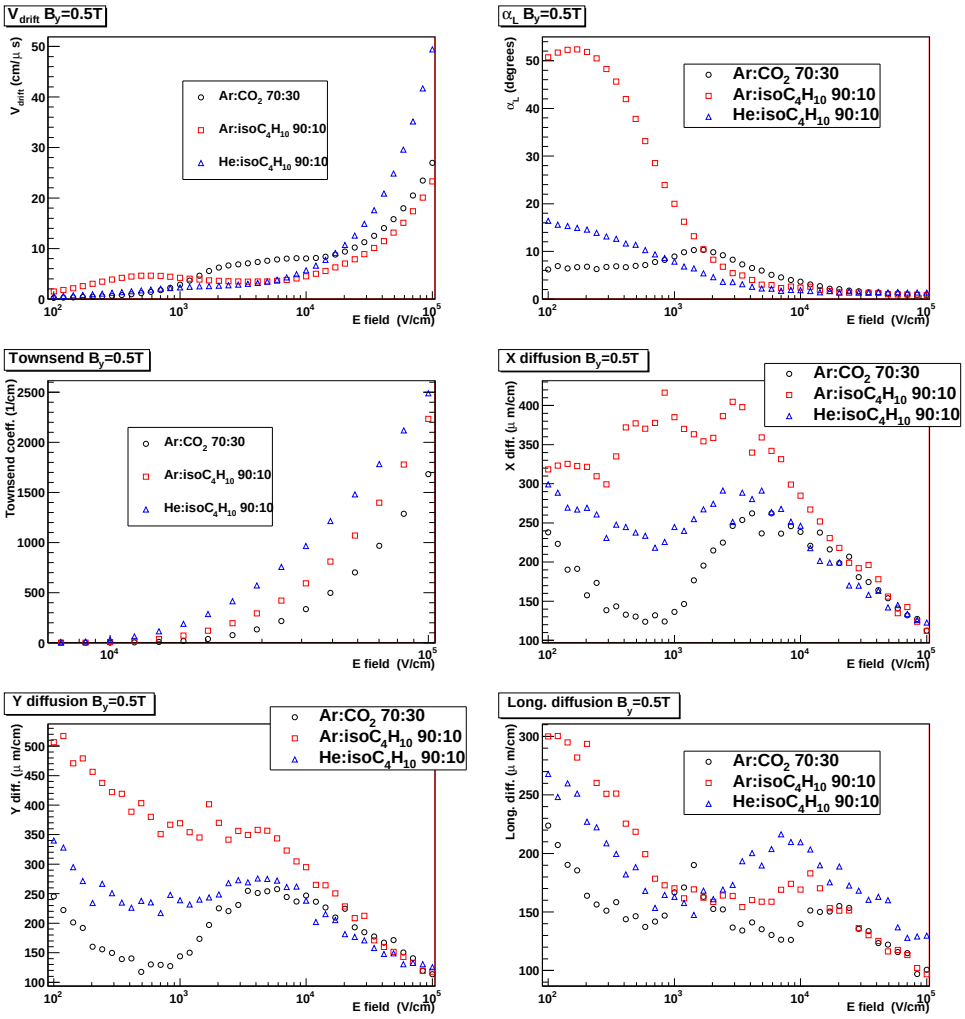

Figure 5.13: Some properties of Ar:CO_2 70 : 30, Ar:isoC$_4$H$_{10}$ 90 : 10 and He:isoC$_4$H$_{10}$ 90 : 10 in a $B = 0.5\ T$ magnetic field as a function of electric field. Top left: drift velocity; top right: Lorentz angle; center left: Townsend coefficient; center right: diffusion coefficient along the x axis (Fig. 5.12); bottom left: diffusion coefficient along the y axis; bottom right: longitudinal diffusion coefficient (corresponding to the diffusion coefficient along the z axis).

position of the clusters, the number ne of electron-ion pairs produced and the energy lost (ΔE) by the m.i.p.

- the electrons start their drift motion with a kinetic energy computed as $\Delta E/ne$.

In order to save CPU time, the track ionizes olny in the drift gap: this matches the discrimination of signals when the primary electrons are produced in the drift gap. GARFIELD requires the drift parameters to be set in order to compute a fine or a rough integration of the equations of the motion. There is a correlation between these parameters and the length of the electron drift path. Some trials gave evidence that the finer is the integration, the smaller is the drift path. This can be avoided in two ways: finding a good compromise between a fine and a rough integration in order to let the electrons reach the anode or exploit GARFIELD tools, since in the &DRIFT section the user must define the volume where the electrons drift. In this case the user can divide the whole chamber in four volumes and follow the electrons in each of these volumes. The advantage of this method is that the reduced dimensions of the boxes allow a finer integration. The boxes have the same base (1.9 mm along x and 0.6 mm along y), while the z length is divided in order to have:

- the drift gap and a half of the first GEM foil
- the first GEM foil, the first tranfer gap and a half of the second GEM foil
- the second GEM foil, the second transfer gap and a half of the third GEM foil
- the third GEM foil and the induction gap

As the electron enters a hole of a GEM foil, the succeeding volume is defined and the simulation goes on. The overlap is requested to avoid that an electron starts from a bound of the volume: in this case GARFIELD doesn't make electron drift. Using the microscopic integration, we can know where the electron is produced and its final coordinates. Moreover GARFIELD uses a *status-code* to indicate if an electron leaves the declared volume (-1), hits the copper layers (-6), hits the kapton (-5) or it is attached (-7). Other cases are foreseen, but they didn't occur in this work. The electrons are considered collected on the anode plane if they reach the lower bound of the fourth box. Studies on the electron displacement were performed as function of the gas mixture and of the angle of the track with respect to the GEM foil.

5.6 The test beam at the H4 area

A test beam was performed at SPS-H4 North Area beam line at CERN in order to study the performance of a triple GEM in magnetic field and to validate a new readout geometry [21],[38]. The H4 area is equipped with the GOLIATH dipole magnet which provides a magnetic field adjustable from 0.1 to 1.5 T perpendicular to the horizontal beam plane and then orthogonal to the electric fields inside the detector. The $X-V$ readout was tested with a tracking telescope realized with five $10\times10\ cm^2$ planar triple GEM detectors. Four chambers were equipped with $X-Y$ while the fifth was equipped with $X-V$ readout. The five detectors were fixed on an aluminium structure (Fig. 5.14) with the active area orthogonal to the beam direction. The detectors were equally spaced between each others, with the $X-V$ chamber placed at the center (Fig. 5.15). The whole setup was 1 m long. The GEMs were partially equipped with 22 digital readout GASTONE boards. The coincidence of 6 scintillators ($3\times3\ cm^2$) read out by silicon photomultipliers provided the trigger signal for the acquisition. The chosen working point for the chambers was the same fixed for the cylindrical prototype: Ar:CO_2 70 : 30 gas mixture and $E_{fields} = 1.5/2.5/2.5/4\ kV/cm$ with $V_{GEM} = 390/380/370\ V$ ($\Sigma V_{GEM} = 1140\ V$). The GASTONE threshold was set at 3.5 fC. As already discussed, the response of a GEM working in magnetic field is affected by a shift of electrons with respect to the ionization points and their larger spread. These effects are common to all the chambers of the test beam setup. Anyway the displacement is related to the direction of the electric and magnetic fields. While the B field direction cannot be changed, the direction of the electric fields in a GEM can be changed reversing the chamber along the beam direction (Fig. 5.15): the $X-Y$ triple GEMs were fixed with the same cathode-anode configuration and the $X-V$ was rotated. The detectors were aligned at zero magnetic field to a few micrometer precision. In presence of magnetic field, the track reconstructed using the $X-Y$ chambers is shifted of Δx with respect to the position of the real track. The $X-V$ chamber that is reversed gives a hit shifted of the same Δx, but in the opposite direction. The distance between the $X-V$ hit and the reconstructed track (called *residual*) is $2\Delta x$. The Δx was measured for different values of magnetic field, starting from $B = 0\ T$ to $B = 1.35\ T$. The results are displayed in Fig. 5.16 The spatial resolution of the $X-V$ chamber was studied as a function of magnetic field (Fig. 5.17). It is defined as the value of the sigma from the gaussian fit of the distribution of the residuals. The spatial resolution (Fig. 5.18 (right)) worsens as the magnetic field increases. This is mainly due to the larger spread (Fig. 5.10) of electrons. In the test beam the effect of magnetic

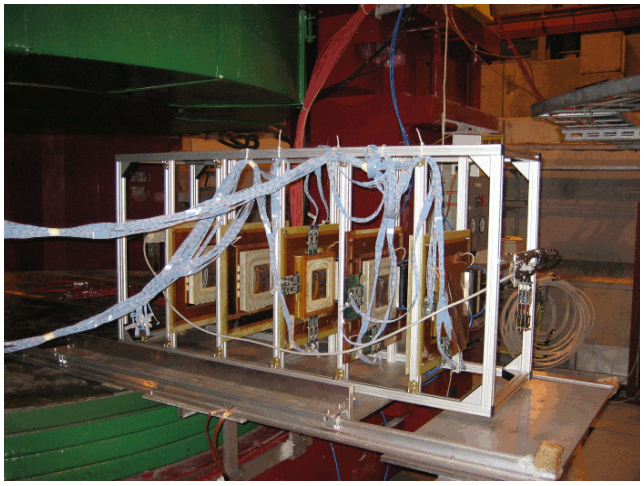

Figure 5.14: Setup of the test beam at CERN with a 2-D readout.

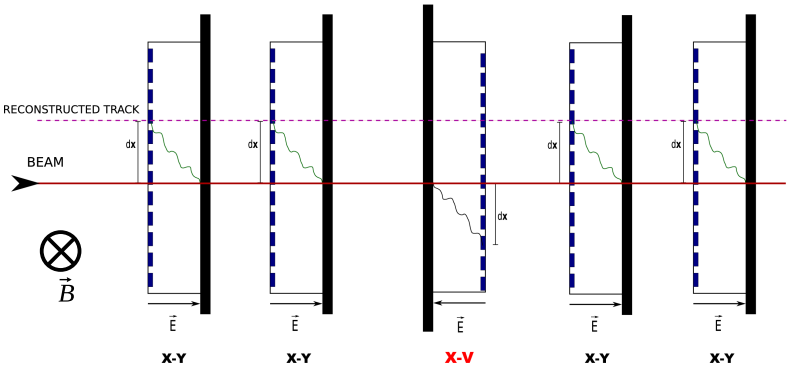

Figure 5.15: Direction of the chambers in the H4 test beam.

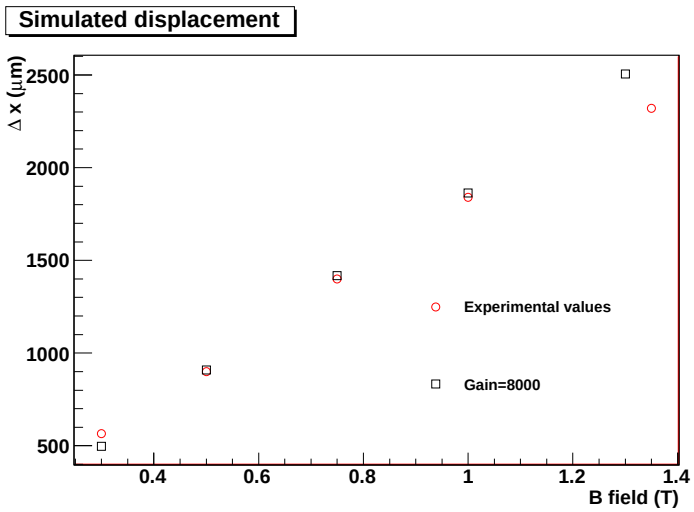

Figure 5.16: Displacement Δx as a function of the magnetic field. The blue point is a GARFIELD simulation results (Fig. 5.10).

field is only along the x direction[3]. The resoultion ranges from 200 μm at $|\vec{B}| = 0\ T$ up to 380 μm at $|\vec{B}| = 1.35\ T$. The y coordinate in the $X - V$ readout was computed as $Y = \tan 50° \cdot X + V/\cos 50°$. The resolution along y direction is $\sim 370\ \mu m$ in good agreement with what expected from the digital readout of the two views. The measurements performed were also focused on the position resolution as a function of the GEM voltage (and consequently of the gain) (Fig. 5.19 (right)). It is stable in a rather broad range of the voltage settings around to the nominal value; an appreciable decrease can actually be observed only for values much below the nominal, corresponding to the gains $G \sim 0.3 \times 10^4$. The performance of the front-end chip GASTONE were studied measuring the cluster size and the reconstruction efficiency, defined as the presence of a cluster in the $X-V$ chamber when a candidate track was reconstructed using four $X - Y$ chambers. GEM efficiency and cluster size were measured as a function of the magnetic field and of the GEM voltage. The efficiency for the nominal KLOE $|\vec{B}|$ field value and voltage settings (Fig. 5.18 (left)) was measured to exceed 99% slightly decreasing at higher magnetic fields. The size of the clusters formed in both X and V views were studied as a function of the value of the GASTONE threshold, of the GEM voltage and of the magnetic field. In principle the charge sharing, grounding, cross-talk could be different for X and V views due to the different readout

[3]The y axis was aligned to $\vec{B}$ (see Fig. 5.15) and the z axis was aligned to the beam direction.

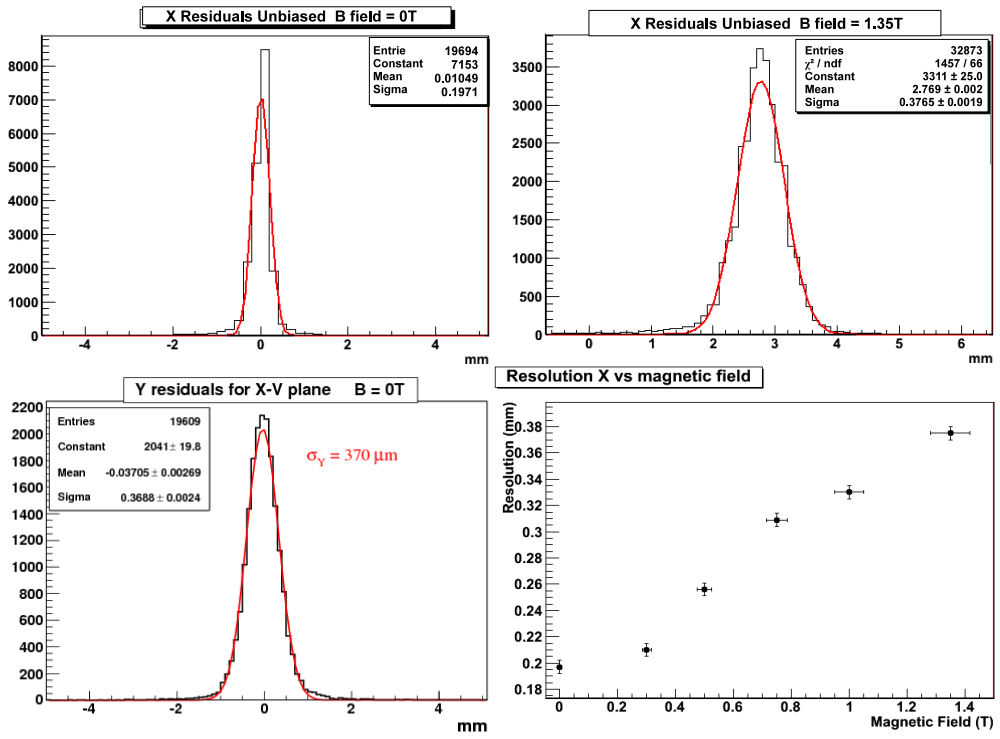

Figure 5.17: Top left: resoultion along x direction at $|\vec{B}| = 0\ T$; Top right: resolution along x direction ar $|\vec{B}| = 1.35\ T$; Bottom left: resolution along y direction at $|\vec{B}| = 0\ T$; Bottom right: resolution on the x coordinate as a function of the magnetic field.

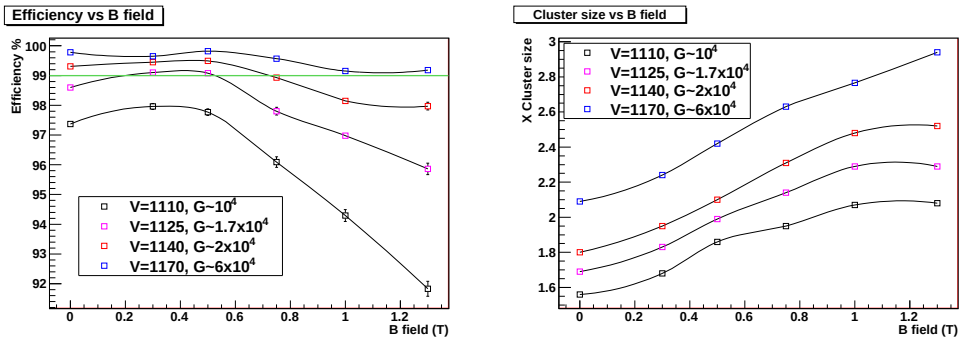

Figure 5.18: Efficiency (left) and x cluster size (right) as functions of magnetic field and of the gain of the GEM.

geometry. However, the measurements show essentially identical response of both X and V readout views (Fig. 5.19 (left)). The variation of the magnetic fields within KLOE-2 planned values ($0.3 \div 0.5\ T$) has a negligible effect on the reconstruction efficiency in the voltage range around our working point ($V_{ref} = 1140\ V$).

5.7 New hole geometry

The construction of large GEM foils requires, as reported in sec. 4.5, a new photolitographic process, based on the use of a single mask. The shape of the holes is not bi-conical but simply conical ($70 - 60\ \mu m$), very close to the cylindrical one[4]. To characterize this new foil, two $10 \times 10\ cm^2$ single-GEM chambers were assembled [42], [43], [44]: one with single-mask foil (see sec. 4.5) and one with the standard foils used as reference. They were both put on the same gas line and flushed with Ar:CO_2 70 : 30, simultaneously irradiated with a 6 keV $X - rays$ gun and tested in current mode. The single-mask chamber was tested in bottom-open configuration and then reversed in top-open configuration. In the first case, the larger section of the hole faced the anode while in the second case the larger section of the hole faced the cathode. The configurations will be referred as $60 - 70$ and $70 - 60$ respectively. In Fig. 5.20 (top left), the new GEM foil has a different behaviour depending on the orientation: in $60 - 70$ configuration the plateau of the efficiency is reached at higher electric drift field with respect to the other configurations. While in Fig. 5.20 (top right) the charge sharing between the bottom GEM surface and the anode is shown, and the values of E_I to equally share the

[4]That is the shape which minimize the *charging-up* effect.

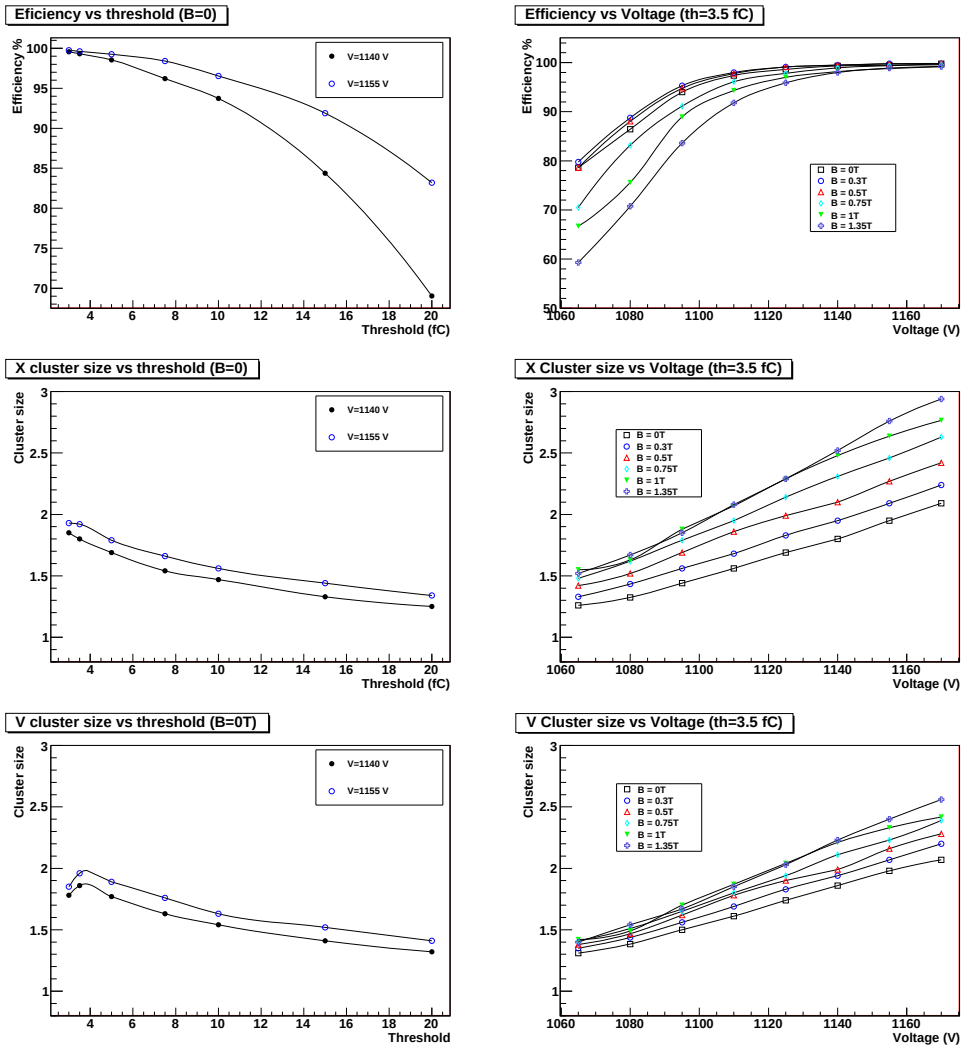

Figure 5.19: Efficiency and cluster size as functions of the GASTONE threshold (left) and of the GEM gain (right).

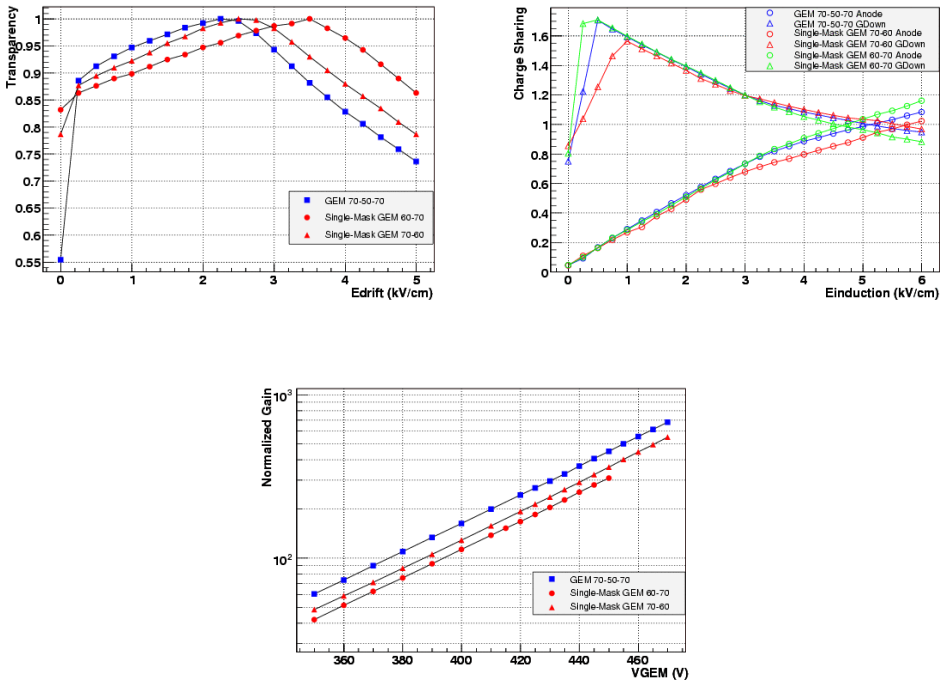

Figure 5.20: Top left: electron transparency as a function of E_D. Top right: charge sharing between bottom surface of the GEM and anode as a function of E_I. Bottom: gas gain in Ar:CO_2 70 : 30.

cahrge are 4.6 kV/cm, 5.2 kV/cm and 5.7 kV/cm for $70-60$, $70-50-70$ [5] and $60-70$ respectively. In Fig. 5.20 bottom, the gas gain of the GEM is shown as function of the voltage drop bewteen the two faces of the foil. The gain of the new foil is $20 \div 30\%$ smaller with respect to the standard one: this means that $10 \div 20$ V additional voltage have to be applied in order to equalize the standard GEM gain.

[5] Standard hole geometry

Chapter 6

Search for Dark Matter in KLOE

As discussed in sec. 1.5, a possible signature of the production of the U boson at DAΦNE is the channel $e^+e^- \to U\gamma \to \mu\mu\gamma$. These events are classified in the **RAD** stream [46], see sec. 2.2.6. It is useful to define some important variables used to address an event to the appropriate category:

- $x_{PCA}, y_{PCA}, z_{PCA}$ are the coordinates of the Point of Closest Approach[1]
- $P_\Sigma = |\vec{p}_1| + |\vec{p}_2|$
- $\Delta E_\gamma = |\vec{p}_1 + \vec{p}_2| - \left(m_\phi - \sqrt{M_\pi^2 + |\vec{p}_1|^2} - \sqrt{M_\pi^2 + |\vec{p}_2|^2}\right)$
- E_{tot} is the total energy in the calorimeter

where $\vec{p}_1$ and $\vec{p}_2$ are the momenta of the two charged particles at the PCA, m_ϕ and $\vec{p}_\phi$ are respectively the mass and the momentum of the ϕ meson. ΔE_γ is a vertex variable that is 0 only in the case of $\pi^+\pi^-\gamma$ and $\pi^+\pi^-$ final states. This stream requires the following selection cuts [48]:

$$\begin{aligned} \rho_{PCA} &= \sqrt{x_{PCA}^2 + y_{PCA}^2} < 8\ cm \\ |z_{PCA}| &< 15\ cm \\ 150\ MeV &< P_\Sigma < 1020\ MeV \\ -220\ MeV &< \Delta E_\gamma < 120\ MeV \\ 80\ MeV &< M_{trk} < 400\ MeV \end{aligned} \tag{6.1}$$

[1]The PCA is the point which minimizes the distance between the impact point of the inward extrapolated track and the beam axis.

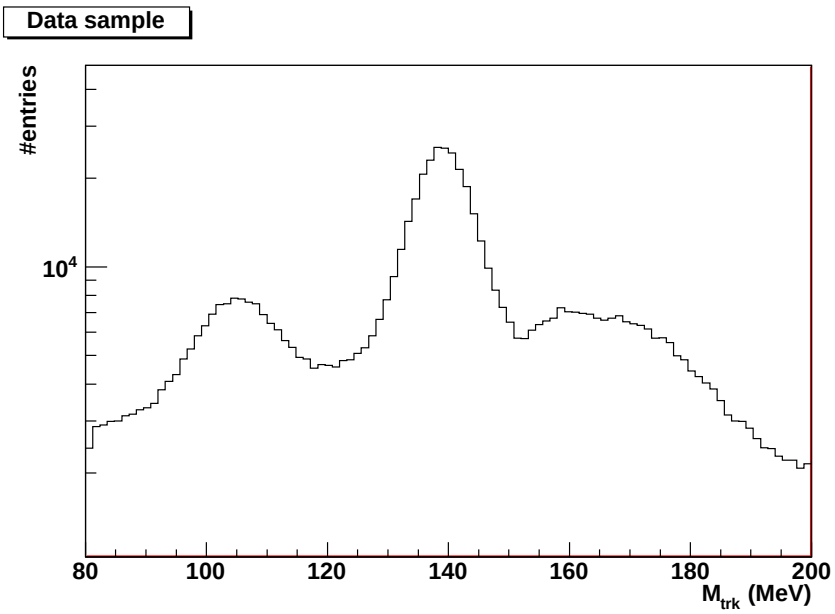

Figure 6.1: An example of an histogram built with the M_{trk} variable.

Eq. 6.1 introduces the so called *trackmass*, M_{trk} [45]. It is computed using the informations from the Drift Chamber, and it the solution of the following equation, obtained by energy and momentum conservation in the hypothesis of two tracks with the same mass and one photon:

$$\sqrt{s} - \sqrt{M_{trk}^2 + |\vec{p}_1|^2} - \sqrt{M_{trk}^2 + |\vec{p}_2|^2} = |\vec{p}_\phi - (\vec{p}_1 + \vec{p}_2)\,| \qquad (6.2)$$

where $\sqrt{s}$ is the c.o.m. energy of DAΦNE. Fig. 6.1 shows the distribution of M_{trk} as obtained by data. As can be seen not only tracks associated to muons ($\mu\mu\gamma$, peaked at $M_{trk} \simeq 105\ MeV$) are selected, but also events associated to pions ($\pi\pi\gamma$, peaked at $M_{trk} \simeq 140\ MeV$) and not well reconstructed events (3π, in the region $M_{trk} > 150\ MeV$). As can be seen in Fig. 6.2 in order to have a pure $\mu\mu\gamma$ sample (where to search for the U boson contribution), it is necessary to cut off the tail of the pion sample in the region $M_{trk} \leq 120\ MeV$: this requires further cuts which will be described in the following. These additional cuts were firstly studied on high purity 3π sample.

6.1 The 3π sample

The tab. 2.2 shows that the sum of the B.R. of $\rho\pi$ and $\pi^+\pi^+\pi^0$ is $\sim 15\%$. The $\rho \to \pi^0\pi^0$ is forbidden by C-symmetry, so the final states is mainly

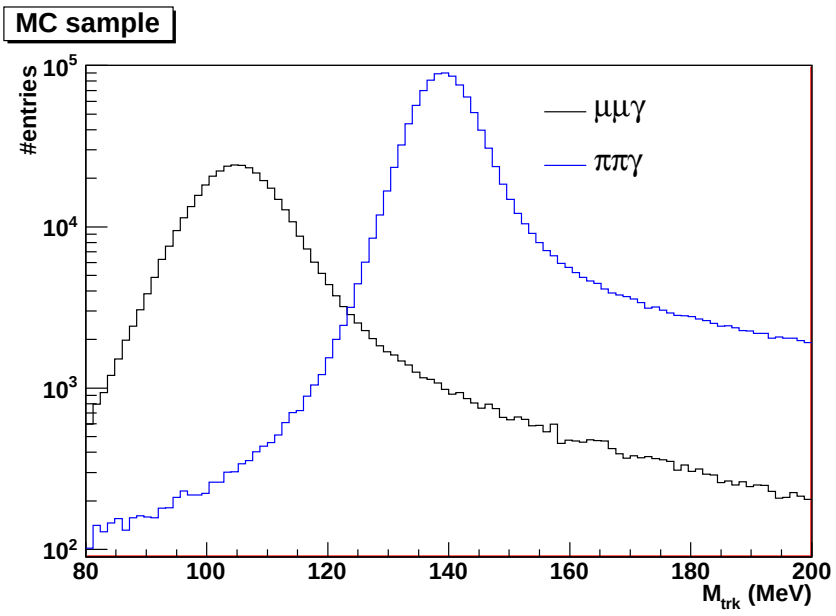

Figure 6.2: M_{trk} computed from a MC $\mu\mu\gamma$ sample (black line) and from a MC $\pi\pi\gamma$ sample (blue line).

$\pi^+\pi^-\pi^0$. The events with two charged tracks and two clusters prompt[2] are recorded in the **RPI** stream. The selection cuts in these case are[3]

$$\begin{aligned} 450\ MeV &< P_\Sigma < 850\ MeV \\ -0.060 - \frac{e^{\frac{P_\Sigma(GeV)-0.4}{0.1}}}{1000.} &< \Delta E_{miss} < 0.100 - \frac{e^{\frac{P_\Sigma(GeV)-0.4}{0.11}}}{1000.} \\ E_{tot} &> 10\ MeV \end{aligned} \tag{6.3}$$

The main signature for such events is the correlation between the ΔE_γ and the sum of the momenta of the two tracks (see Fig. 6.3). Indeed the selection on ΔE_{miss} allows to separate the three-pion events from other final states characterized by two tracks with high momentum and one prompt photon. In order to study the trackmass distribution in this pure sample, eq. 6.2 must be slightly modified since in this case the missing energy is carried out by the π^0 and not by the photon.

$$\sqrt{s} - \sqrt{M_{trk}^2 + |\vec{p}_1|^2} - \sqrt{M_{trk}^2 + |\vec{p}_2|^2} = \sqrt{|\vec{p}_\phi - (\vec{p}_1 + \vec{p}_2)\,|^2 + m_{\pi^0}^2} \tag{6.4}$$

[2] A cluster is called *prompt* if it is not associated to a charged track.
[3] ΔE_{miss} is equivalent to ΔE_γ.

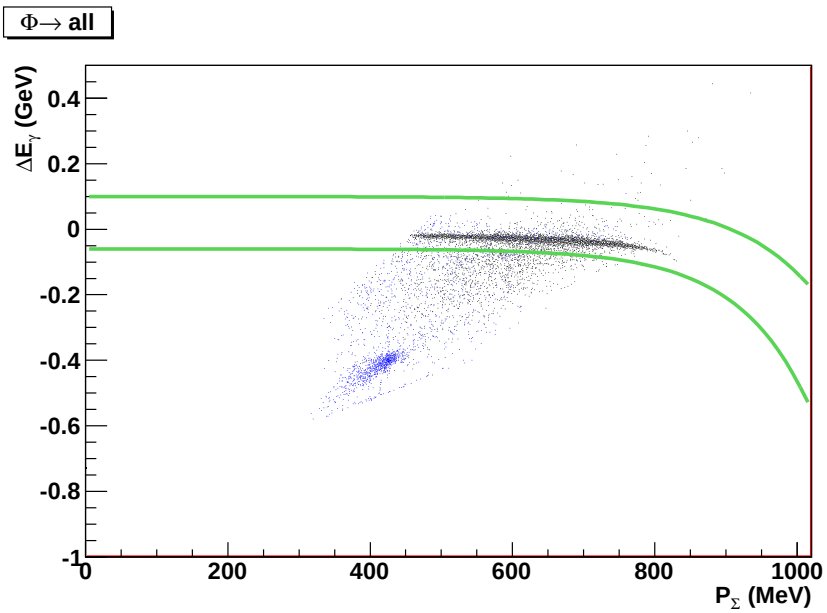

Figure 6.3: Graphical representation of the ΔE selection. The black points are events associated to the 3π channel while the blue points are associated to all the other kaon decays. The events out of the area bounded by the two green lines are rejected

To further improve the purity of the sample we require two clusters prompt associated to the photons coming from the decay of the π^0 ($BR_{\pi^0\to 2\gamma} = 98.823 \pm 0.034\%$ [3]): $120\ MeV \leq M_{\gamma\gamma} \leq 150\ MeV$, where

$$M_{\gamma\gamma} = \sqrt{2E_1E_2\,(1-\cos\theta_{\gamma\gamma})}$$

with $\theta_{\gamma\gamma}$ the angle between the photons. Moreover, we ask for events with tracks detected in the barrel calorimeter ($50^\circ < \theta_{trk} < 130^\circ$) and for $0.35\ GeV^2 < q^2 < 0.5\ GeV^2$. A likelihood estimator as defined in [49] is also used to select events. The study on rejection of events in the region $M_{trk} < 120\ MeV$ was performed using also MC samples.

6.1.1 The comparison Data-MC

The Monte Carlo simulation is useful to estimate the selection and reconstruction efficiency for a given cut [50]. A comparison of the M_{trk} computed from data and MC samples was finally done (Fig. 6.4). There is a discrepancy between the two distributions in the region below $120\ MeV$, which if

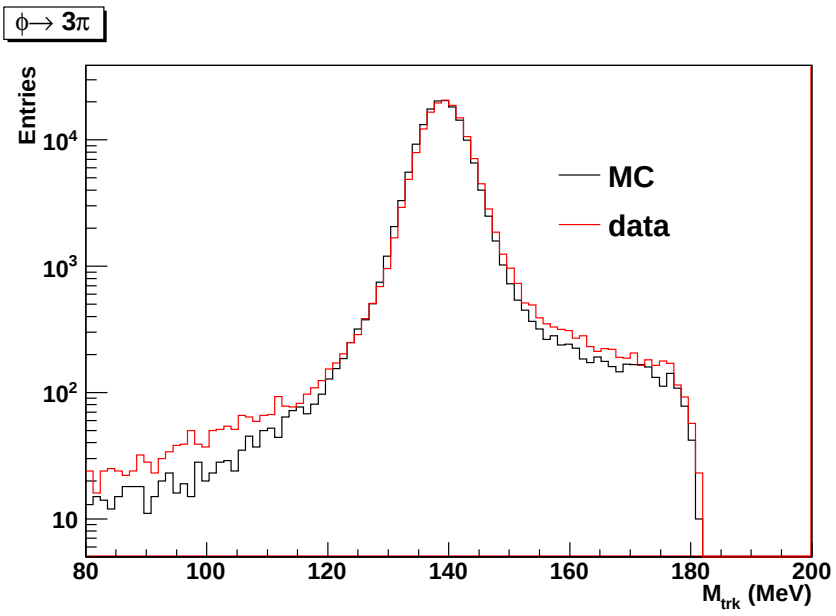

Figure 6.4: Comparison among the M_{trk} from 3π events computed from MC and data samples.

not cured could lead to systematic effect in the $\mu\mu\gamma$ selection. Before applying a correction factor to the Monte Carlo sample we studied the possibility to further cut the $\pi\pi\gamma$ tail.

6.1.2 The error on the $\mathrm{M_{trk}}$

The basic idea to reduce the $\pi\pi\gamma$ low trackmass value is that the events contributiong to the tails of the M_{trk} distribution are not well reconstructed, so the error associated to the M_{trk} could be a discriminating variable. A study on the correlation between the M_{trk} and the associated error $\sigma_{M_{trk}}$ is performed. The error of a function of many variables can be computed as [51]

$$\sigma^2_{M_{trk}} = \sum_{i,j} \frac{\partial M_{trk}}{\partial x_i} \mathbf{M}_{i,j} \frac{\partial M_{trk}}{\partial x_j} \tag{6.5}$$

where the x_i (x_j) are the $i-$th ($j-$th) variables of the function and $\mathbf{M}$ is the covariance matrix, with elements:

$$\mathbf{M}_{i,i} = \sigma^2_{x_i} \quad \mathbf{M}_{i,j} = \rho_{x_i x_j}$$

$\sigma^2_{x_i}$ is the squared uncertainty of the variable x_i while $\rho_{x_i x_j}$ is the covariance between the variables x_i and x_j. In the datasets used for the analysis, the

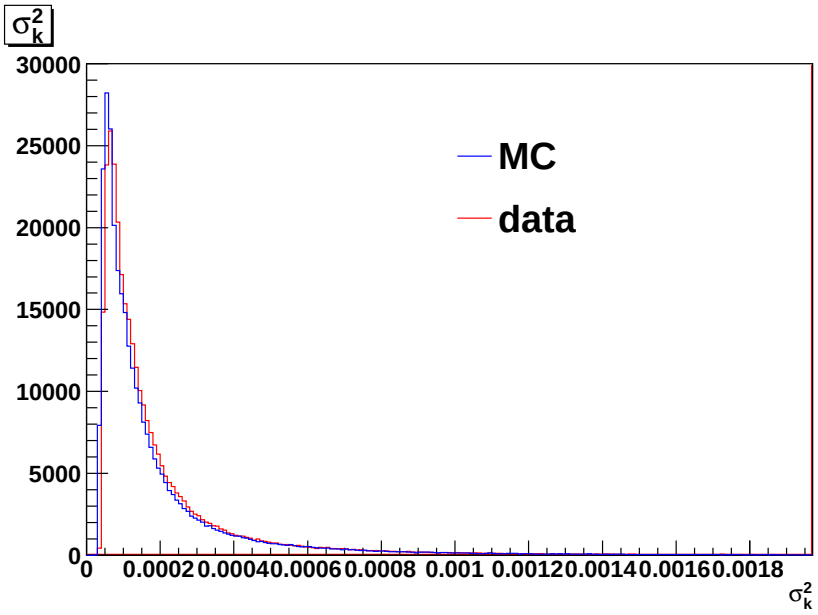

Figure 6.5: Comparison of the error on the σ_k^2 obtained from MC and data samples.

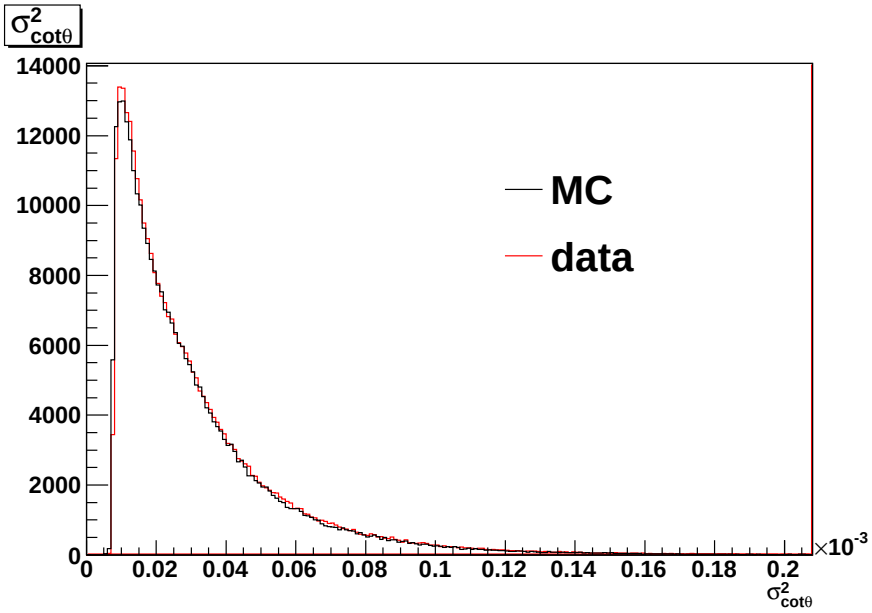

Figure 6.6: Comparison of the error on the $\sigma^2_{\cot\theta}$ obtained from MC and data samples.

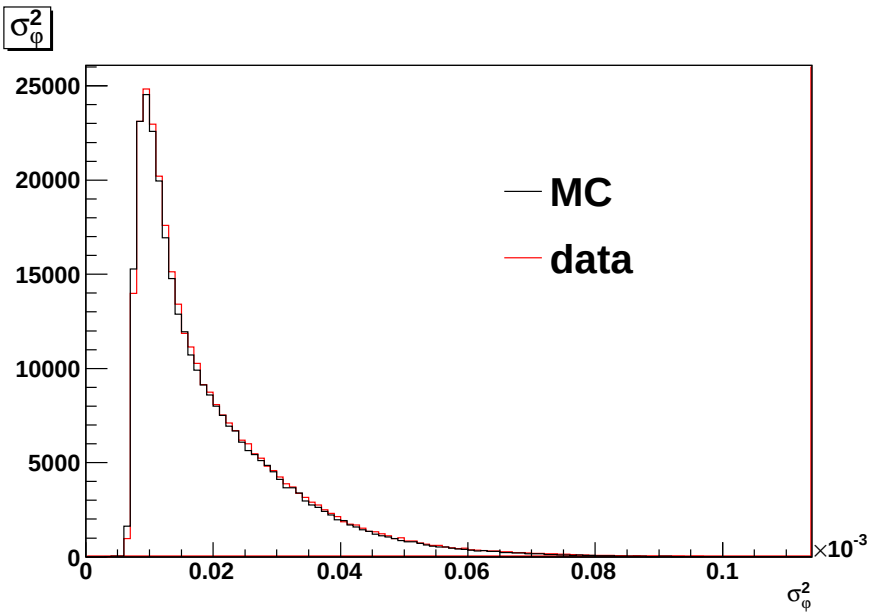

Figure 6.7: Comparison of the error on the σ^2_φ obtained from MC and data samples.

informations on the uncertainty of the components of $\vec{p}_1$ and $\vec{p}_2$ are missing, while are present the error on the curvature k of the tracks, the error on the cotangent of the azimuthal angle ($\cot\theta$) and the error on the polar angle (φ). The relationships among these variables and the components of the momenta $\vec{p}_{1,2}$ are

$$k_i = (-1)^{i-1}\frac{1000}{|\vec{p}_i^{\perp}|}, \quad \cot\theta_i = \frac{p_i^z}{|\vec{p}_i^{\perp}|}, \quad \varphi_i = \tan^{-1}\frac{p_i^y}{p_i^x} \tag{6.6}$$

with $|\vec{p}_i^{\perp}| = \sqrt{(p_i^x)^2 + (p_i^y)^2}$. Assuming that there is no correlation among the parameters describing different tracks, the eq. 6.5 becomes in this case

$$\sigma^2_{M_{trk}} = \left(\frac{\partial M_{trk}}{\partial k_1} \quad \frac{\partial M_{trk}}{\partial \cot\theta_1} \quad \frac{\partial M_{trk}}{\partial \varphi_1} \quad \frac{\partial M_{trk}}{\partial k_2} \quad \frac{\partial M_{trk}}{\partial \cot\theta_2} \quad \frac{\partial M_{trk}}{\partial \varphi_2} \right) \cdot$$

$$\begin{pmatrix} \sigma^2_{k_1} & \rho_{k_1\cot\theta_1} & \rho_{k_1\varphi_1} & 0 & 0 & 0 \\ \rho_{\cot\theta_1 k_1} & \sigma^2_{\cot\theta_1} & \rho_{\cot\theta_1\varphi_1} & 0 & 0 & 0 \\ \rho_{\varphi_1 k_1} & \rho_{\varphi_1\cot\theta_1} & \sigma^2_{\varphi_1} & 0 & 0 & 0 \\ 0 & 0 & 0 & \sigma^2_{k_2} & \rho_{k_2\cot\theta_2} & \rho_{k_2\varphi_2} \\ 0 & 0 & 0 & \rho_{\cot\theta_2 k_2} & \sigma^2_{\cot\theta_2} & \rho_{\cot\theta_2\varphi_2} \\ 0 & 0 & 0 & \rho_{\varphi_2 k_2} & \rho_{\varphi_2\cot\theta_2} & \sigma^2_{\varphi_2} \end{pmatrix} \begin{pmatrix} \frac{\partial M_{trk}}{\partial k_1} \\ \frac{\partial M_{trk}}{\partial \cot\theta_1} \\ \frac{\partial M_{trk}}{\partial \varphi_1} \\ \frac{\partial M_{trk}}{\partial k_2} \\ \frac{\partial M_{trk}}{\partial \cot\theta_2} \\ \frac{\partial M_{trk}}{\partial \varphi_2} \end{pmatrix}$$

The distribution of M_{trk} as a function of its error is shown in Fig. 6.8: the

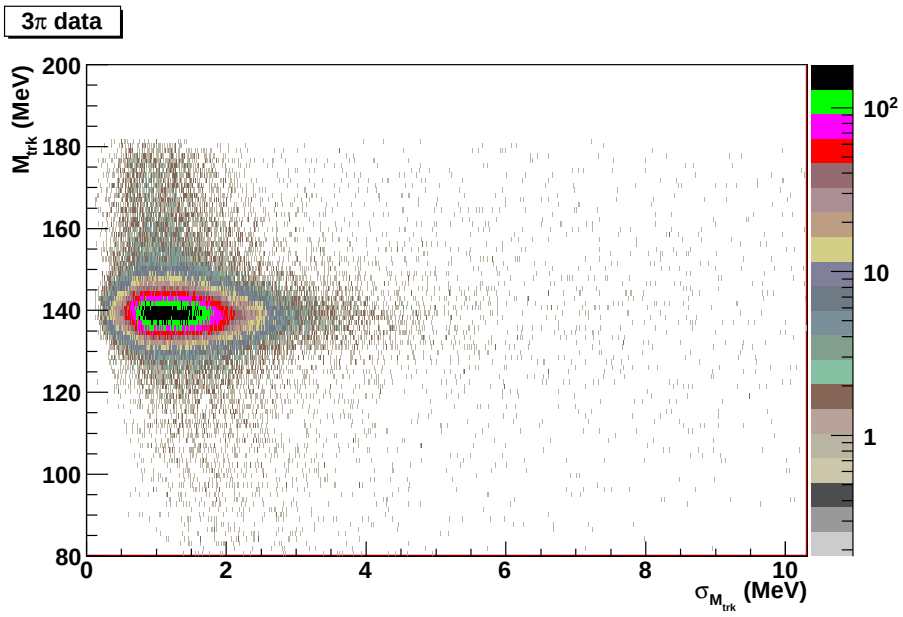

Figure 6.8: M_{trk} vs $\sigma_{M_{trk}}$ without cuts on $\sigma_{M_{trk}}$.

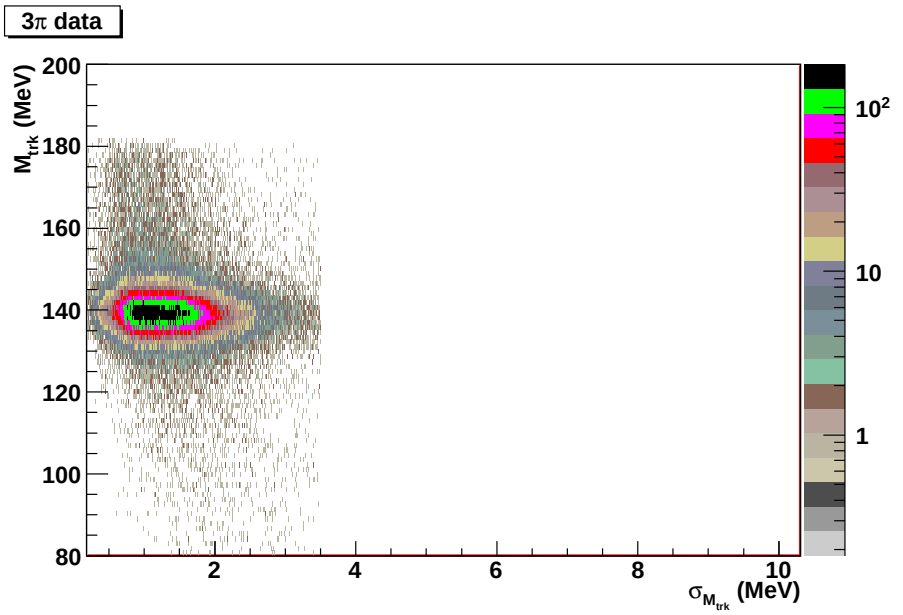

Figure 6.9: M_{trk} vs $\sigma_{M_{trk}}$ with $\sigma_{M_{trk}} < 3.5\ MeV$.

events are mostly placed in the region $120\ MeV < M_{trk} < 150\ MeV$ and $\sigma_{M_{trk}} < 3\ MeV$. The events with the value of trackmass below $140\ MeV$ are distributed on the whole range of $\sigma_{M_{trk}}$. A cut on the error of the trackmass was applied in order to reduce the population of events in this region. The events with $\sigma_{M_{trk}} > 3.5\ MeV$ were rejected. The quality of the cut can be evaluated by the efficiency ε: the ratio of the events selected on the total number. In this case we found $\varepsilon \sim 96\%$. The effect of the cut is visible in Fig. 6.9 and in Fig. 6.10. The number of events in the region $M_{trk} < 120\ MeV$ decreases of almost a factor 2, leaving practically unchanged the central peak. Since the cut on the error of the trackmass is very efficient, the implementation of this cut was studied on $\pi\pi\gamma$ and for $\mu\mu\gamma$ samples.

6.2 The $\pi\pi\gamma$ and $\mu\mu\gamma$ samples

In this case we ask for events $e^+e^- \to x^+x^-\gamma$, where the $x^\pm$ could be $e^\pm, \mu^\pm$ or $\pi^\pm$. The topology of the event is characterized by two charged tracks reconstructed in the Drift Chamber and one photon. Other quality cuts are:

$$\begin{aligned}
\sqrt{x_{FH}^2 + y_{FH}^2} &< 50\ cm \\
\sqrt{x_{PCA}^2 + y_{PCA}^2} &< 8\ cm \\
|z_{PCA}| &< 7\ cm \\
P_\perp > 160\ MeV/c \quad & or \quad P_z > 90\ MeV/c \\
50^\circ < \theta_{trk} &< 130^\circ \\
\theta_\gamma &< 15^\circ \qquad (6.7)
\end{aligned}$$

(6.8)

where x_{FH}, y_{FH} and z_{FH} are the coordinates of the First Hit of a track in the Drift Chamber and θ_{trk} is the azimuthal angle of the track at the PCA. The cut on the polar angle of the photon enhances the probability of the photon to be emitted by the electron or by the positron (in this way increasing the sensitivity for the U boson search). The error of the trackmass can be computed as reported in the previous section, taking into account that in this case the M_{trk} must be computed using eq. 6.2. The same cut as in the case of the 3π sample (rejecting events with $\sigma_{M_{trk}} > 3.5\ MeV$) was applied. The effect of this cut is shown in Fig. 6.11. The efficiency of the cut is $\sim 32.5\%$, much lower than what expected and required. This small value for ε can be explained since the distribution of $\sigma_{M_{trk}}$ has a peak around $1.5\ MeV$ but has also a long tail until $30\ MeV$. A rough cut cannot be applied in this case to separate the μ peak from the π peak, so further finer cuts must be studied.

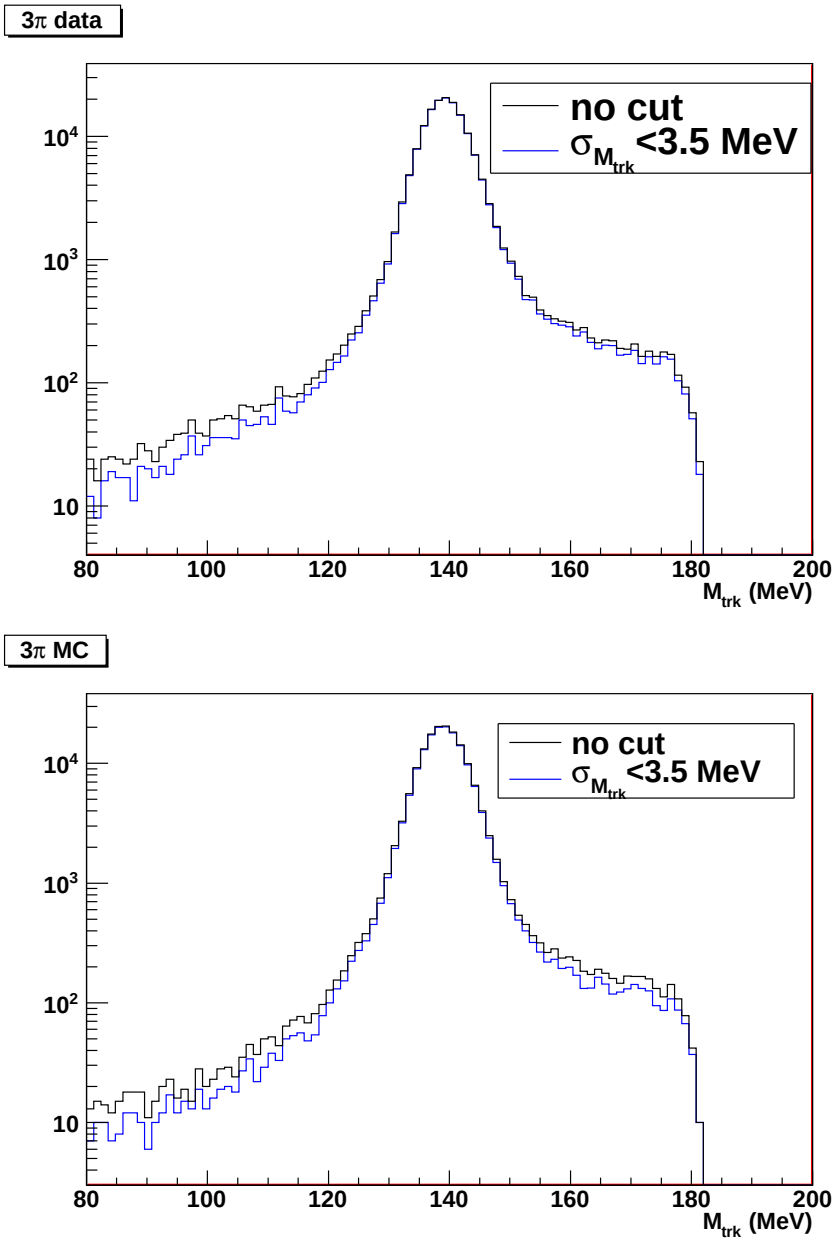

Figure 6.10: M_{trk} spectrum obtained by KLOE data (top) and by MC (bottom).

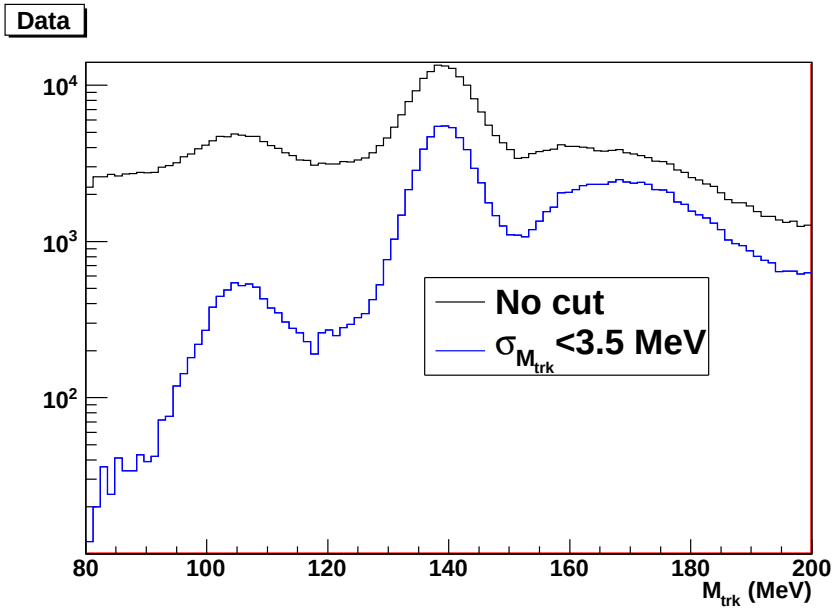

Figure 6.11: The M_{trk} spectrum with the cut $\sigma_{M_{trk}}$ compared to the spectrum without cut computed by data.

6.3 The $\sigma_{M_{trk}} - q_x^2$ correlation

An important information on the event can be provided by the invariant mass of the two charged tracks.

$$\begin{aligned} q_x^2 &= (p_1^\mu + p_2^\mu) \\ &= 2\left[m_x^2 + (E_1 E_2 - \vec{p}_1 \cdot \vec{p}_2)\right] \end{aligned} \tag{6.9}$$

where x is the particle associated to the tracks of 4-momentum p^μ. It is worth notice that for each event two variables can be computed: q_π^2 (in the hypothesis that pions are associated to the tracks) and q_μ^2 (muons hypothesis). During the analysis, an evidence of the correlation between the $\sigma_{M_{trk}}$ and the q_x^2 (both in pion and muon hypothesis) arose. This correlation was used to define a cut on the $\sigma_{M_{trk}}$ as a function of the q_x^2 of the event. Each slice in q_x^2 of the distribution was fitted with a gaussian[4], obtaining a mean value of the error $\bar{\sigma}_{M_{trk}}$ and its standard deviation $\sigma_{\sigma_{M_{trk}}}$. This information allowed us to obtain (with a polynomial fit) an analitical expression for the $\sigma_{M_{trk}}$ and for $\sigma_{\sigma_{M_{trk}}}$ as a function of q_x^2. For each event we computed the

[4]The procedure can be done with a specified statement in ROOT

following variable

$$\xi_x = \frac{\sigma_{M_{trk}} - \bar{\sigma}_{M_{trk}}(q_x^2)}{\sigma_{\sigma_{M_{trk}}}(q_x^2)} \tag{6.10}$$

that gives an estimation of the difference between the error on the M_{trk} and the mean error expected for the given q_x^2 proportional to the standard deviation of the error. Different cuts on ξ_x were applied on the datasets, computing the muon and the pion efficiency as a function of q_x^2. Moreover for the three slices of q_x^2 the ratio of the $\varepsilon_{\pi\pi\gamma}/\varepsilon_{\mu\mu\gamma}$ as a function of the M_{trk} was computed in the region $M_{trk} < 120\ MeV$, in order to evaluate the rejection power for pions and muons. Four different cases can be obtained

- Study of the cuts deriving from the functions $\sigma_{M_{trk}}(q_\pi^2)$ and $\sigma_{\sigma_{M_{trk}}}(q_\pi^2)$ computed from the MC $\pi\pi\gamma$ sample
- Study of the cuts deriving from the functions $\sigma_{M_{trk}}(q_\pi^2)$ and $\sigma_{\sigma_{M_{trk}}}(q_\pi^2)$ computed from the MC $\mu\mu\gamma$ sample
- Study of the cuts deriving from the functions $\sigma_{M_{trk}}\left(q_\mu^2\right)$ and $\sigma_{\sigma_{M_{trk}}}\left(q_\mu^2\right)$ computed from the MC $\pi\pi\gamma$ sample
- Study of the cuts deriving from the functions $\sigma_{M_{trk}}\left(q_\mu^2\right)$ and $\sigma_{\sigma_{M_{trk}}}\left(q_\mu^2\right)$ computed from the MC $\mu\mu\gamma$ sample

6.3.1 $\sigma_{M_{trk}}\left(q_\pi^2\right)$ and $\sigma_{\sigma_{M_{trk}}}\left(q_\pi^2\right)$ from MC $\pi\pi\gamma$

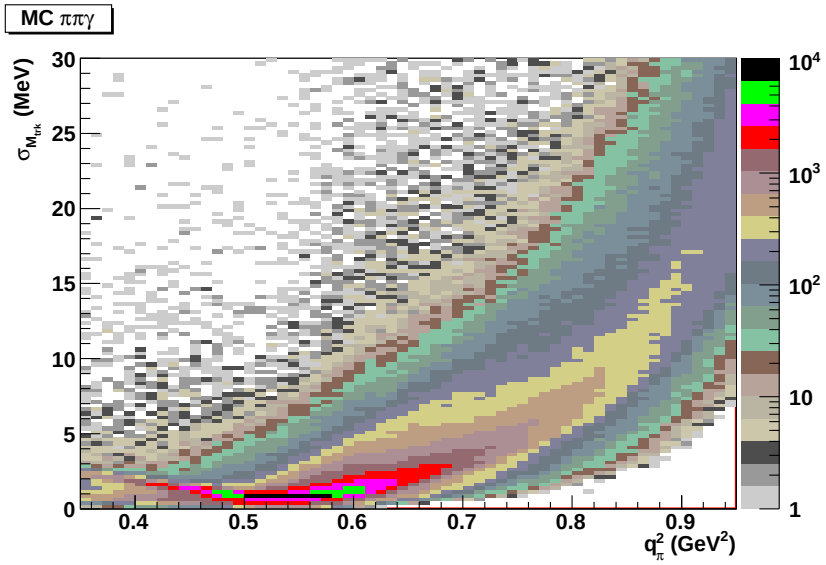

Figure 6.12: $\sigma_{M_{trk}}$ vs q_π^2 of the events for the MC $\pi\pi\gamma$.

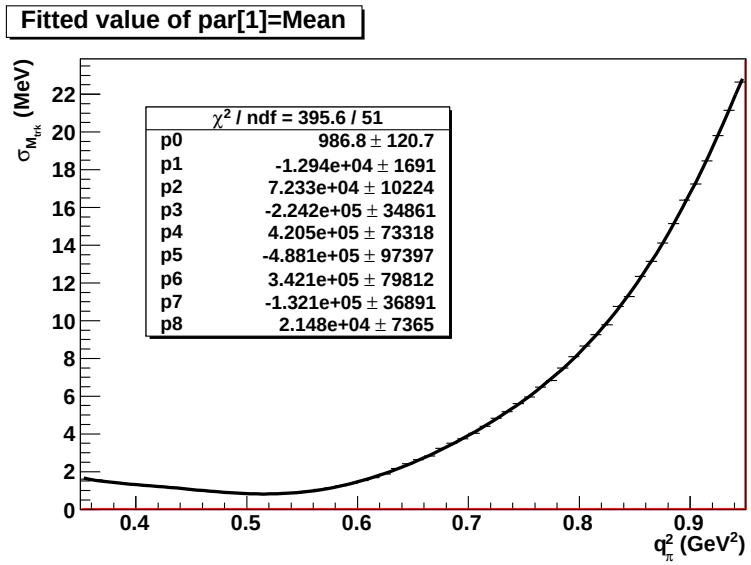

Figure 6.13: $\bar{\sigma}_{M_{trk}}$ as a function of the q_π^2 for the MC $\pi\pi\gamma$ sample.

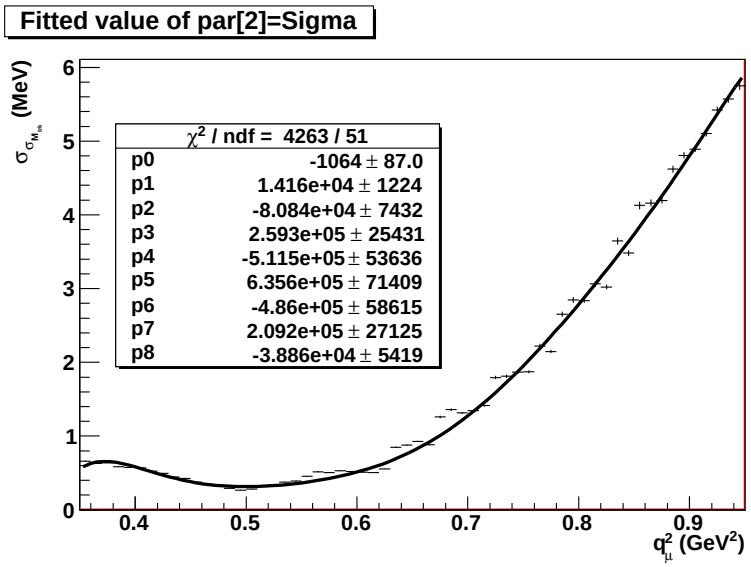

Figure 6.14: $\sigma_{\sigma_{M_{trk}}}(q_\pi^2)$ as a function of the q_π^2 for the MC $\pi\pi\gamma$ sample.

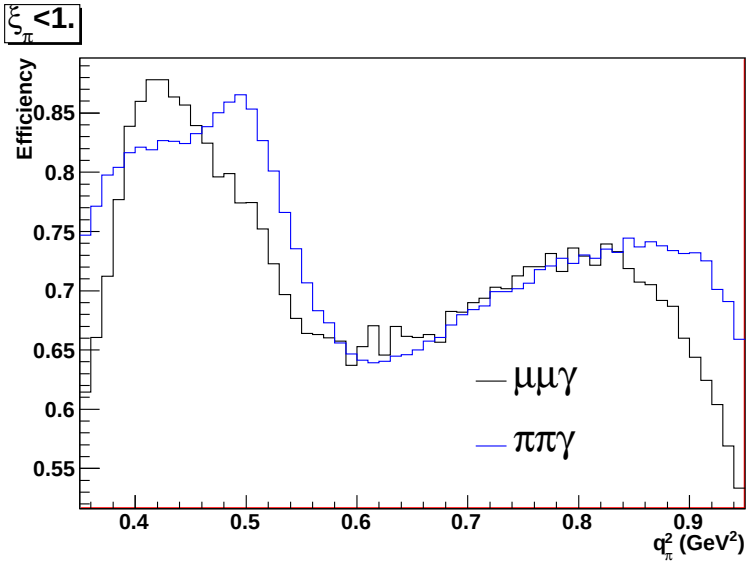

Figure 6.15: Efficiency of the cut $\xi_\pi < 1.$ for both MC $\mu\mu\gamma$ and MC $\pi\pi\gamma$ as a function of q_π^2.

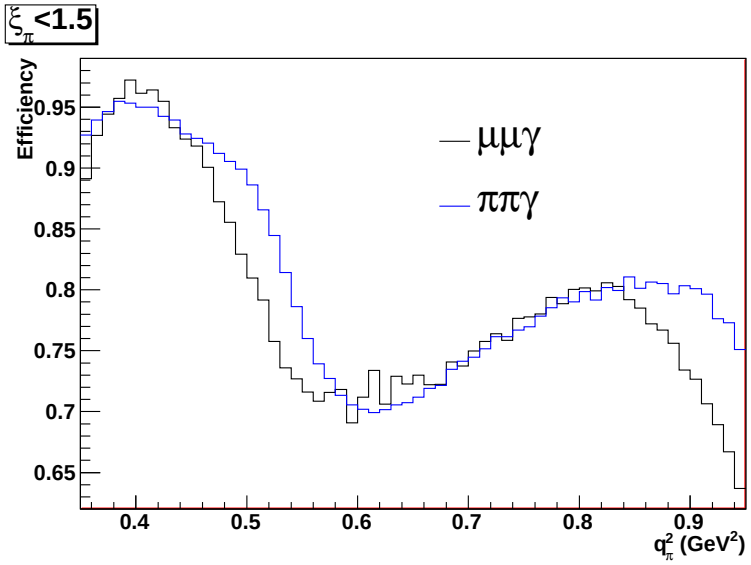

Figure 6.16: Efficiency of the cut $\xi_\pi < 1.5$ for both MC $\mu\mu\gamma$ and MC $\pi\pi\gamma$ as a function of q_π^2.

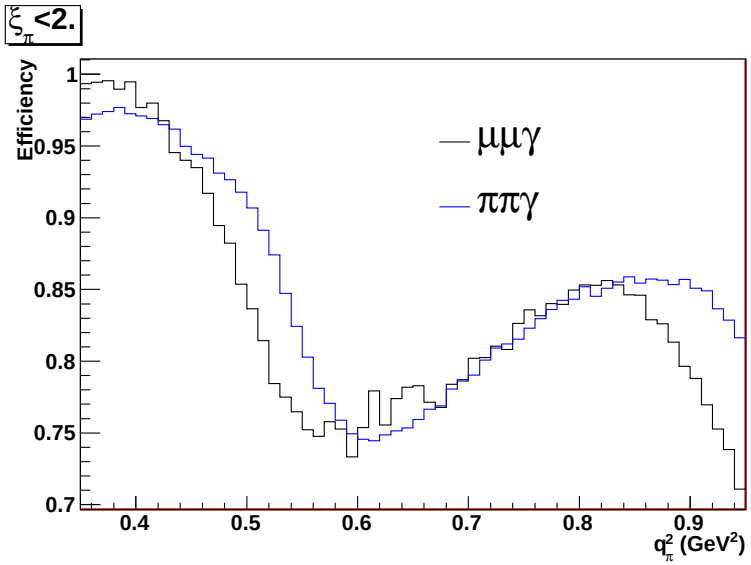

Figure 6.17: Efficiency of the cut $\xi_\pi < 2.$ for both MC $\mu\mu\gamma$ and MC $\pi\pi\gamma$ as a function of q_π^2.

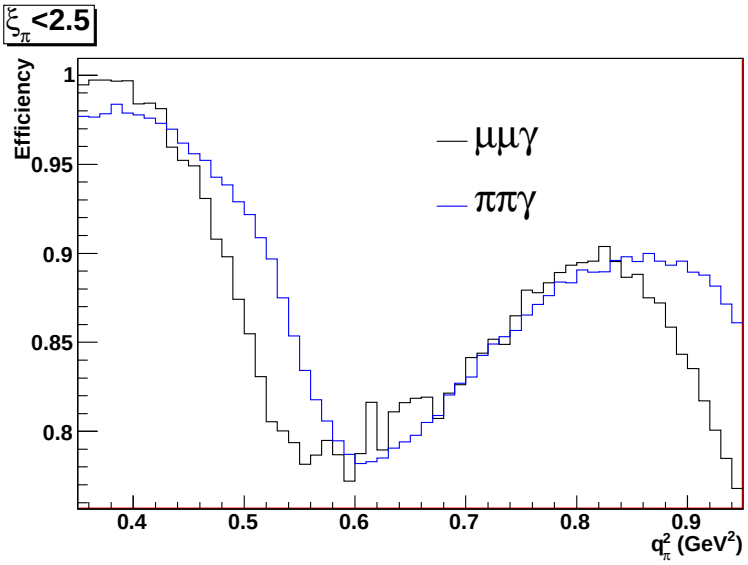

Figure 6.18: Efficiency of the cut $\xi_\pi < 2.5$ for both MC $\mu\mu\gamma$ and MC $\pi\pi\gamma$ as a function of q_π^2.

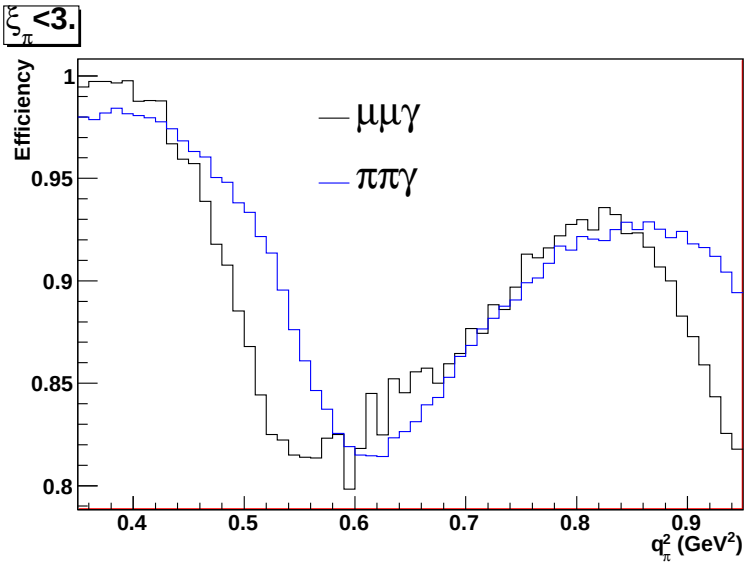

Figure 6.19: Efficiency of the cut $\xi_\pi < 3.$ for both MC $\mu\mu\gamma$ and MC $\pi\pi\gamma$ as a function of q_π^2.

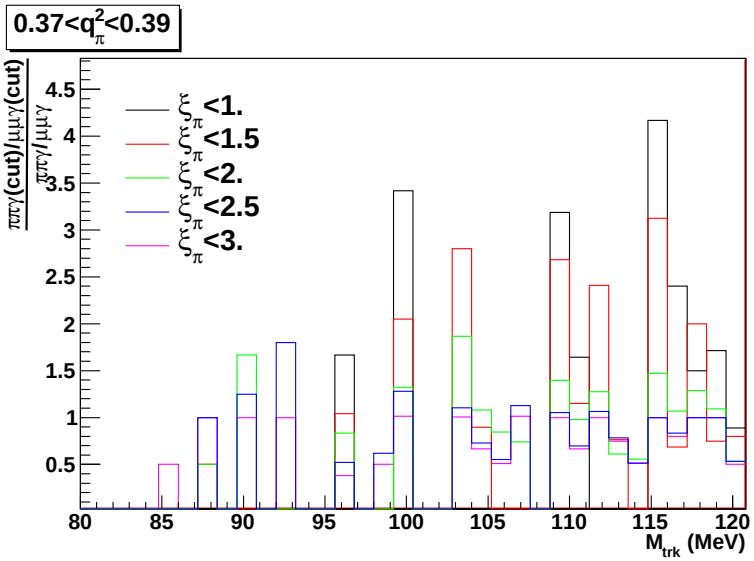

Figure 6.20: $\varepsilon_{\pi\pi\gamma}/\varepsilon_{\mu\mu\gamma}$ for all the applied cuts on ξ_π for events with $0.37 < q_\pi^2 < 0.39$ in the region $M_{trk} < 120\ MeV$.

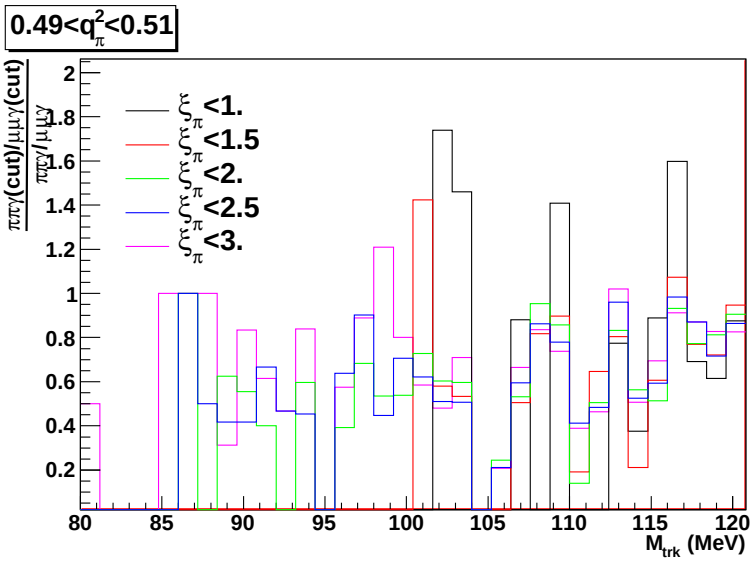

Figure 6.21: $\varepsilon_{\pi\pi\gamma}/\varepsilon_{\mu\mu\gamma}$ for all the applied cuts on ξ_π for events with $0.49 < q_\pi^2 < 0.51$ in the region $M_{trk} < 120\ MeV$.

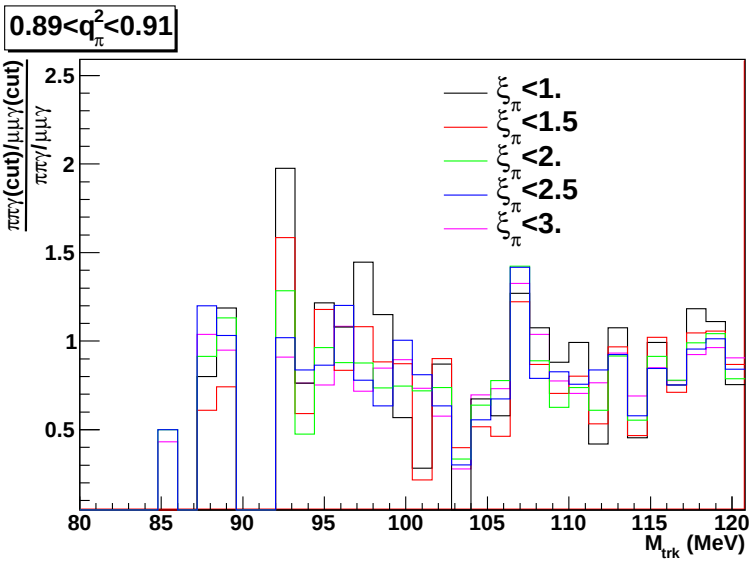

Figure 6.22: $\varepsilon_{\pi\pi\gamma}/\varepsilon_{\mu\mu\gamma}$ for all the applied cuts on ξ_π for events with $0.89 < q_\pi^2 < 0.91$ in the region $M_{trk} < 120\ MeV$.

6.3.2 $\sigma_{M_{trk}}\left(q_\mu^2\right)$ and $\sigma_{\sigma_{M_{trk}}}\left(q_\mu^2\right)$ from MC $\pi\pi\gamma$

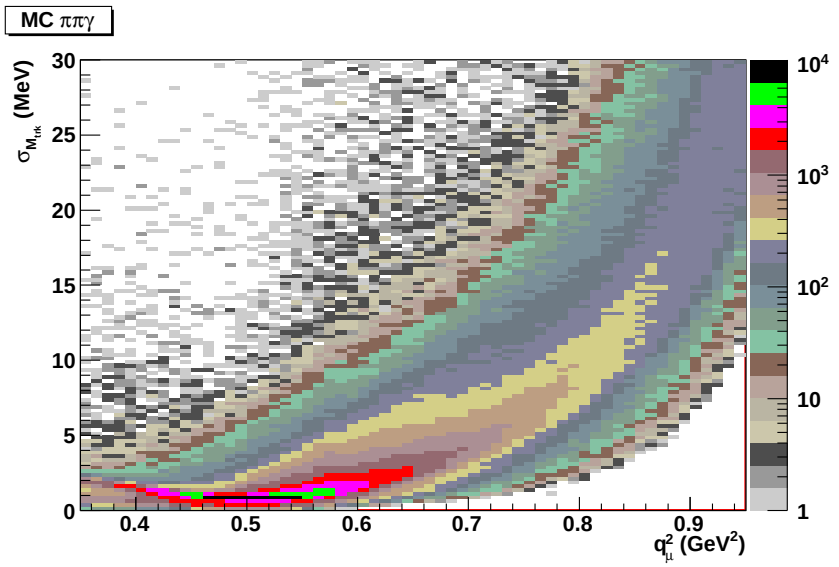

Figure 6.23: $\sigma_{M_{trk}}$ vs q_μ^2 of the events for the MC $\pi\pi\gamma$.

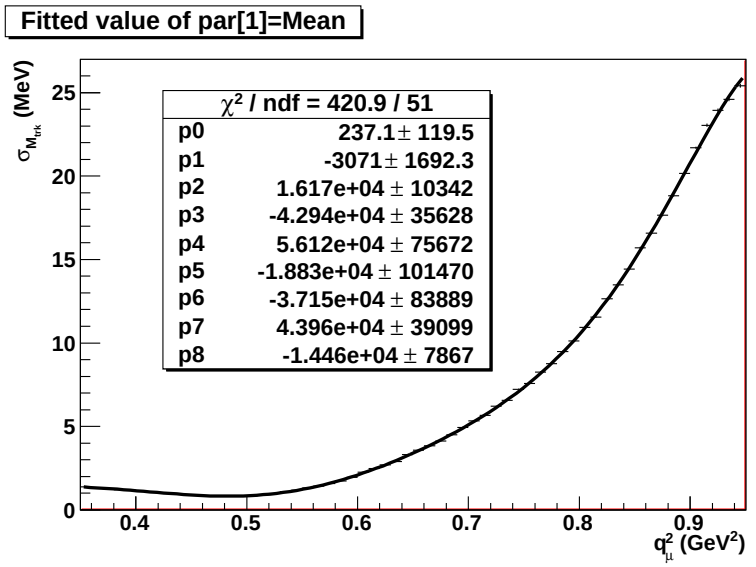

Figure 6.24: $\bar{\sigma}_{M_{trk}}$ as a function of q_μ^2 for the MC $\pi\pi\gamma$ sample.

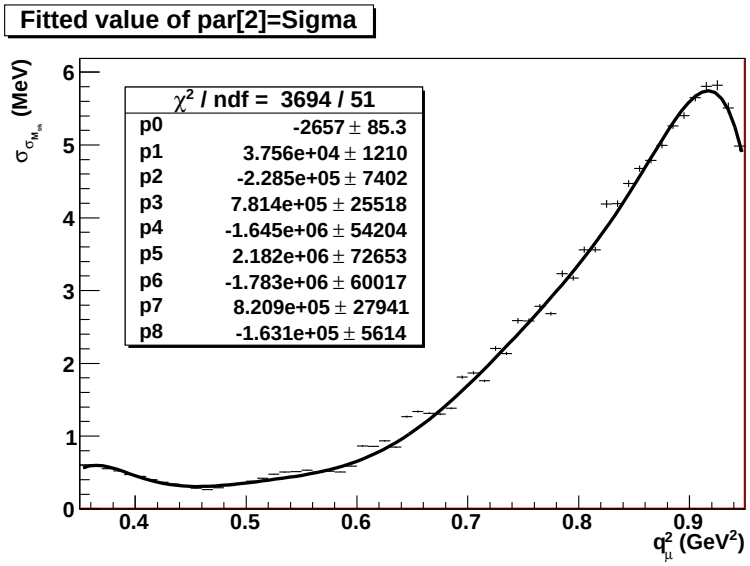

Figure 6.25: $\sigma_{\sigma_{M_{trk}}}$ as a function of the q_μ^2 for the MC $\pi\pi\gamma$ sample.

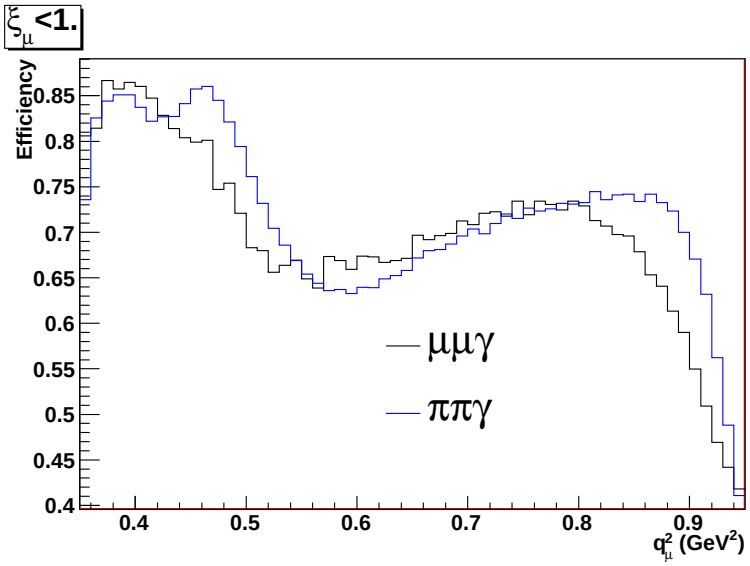

Figure 6.26: Efficiency of the cut $\xi_\mu < 1.$ for both MC $\mu\mu\gamma$ and MC $\pi\pi\gamma$ as a function of q_μ^2.

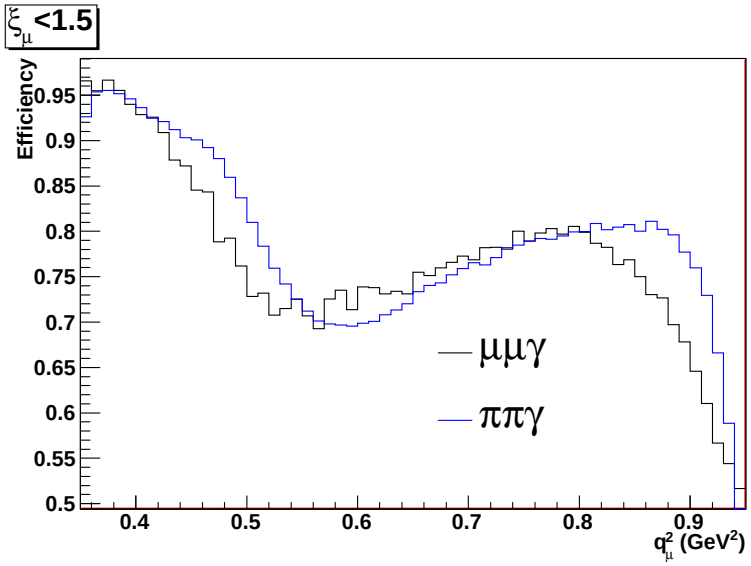

Figure 6.27: Efficiency of the cut $\xi_\mu < 1.5$ for both MC $\mu\mu\gamma$ and MC $\pi\pi\gamma$ as a function of q_μ^2.

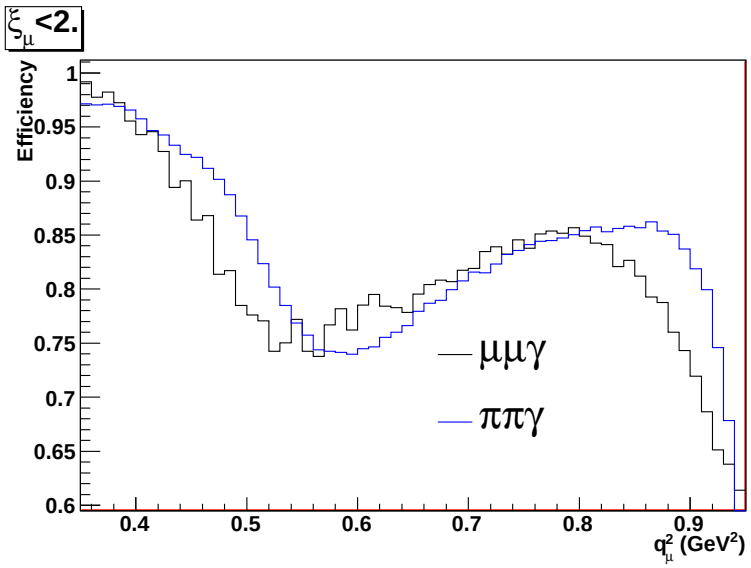

Figure 6.28: Efficiency of the cut $\xi_\mu < 2.$ for both MC $\mu\mu\gamma$ and MC $\pi\pi\gamma$ as a function of q_μ^2.

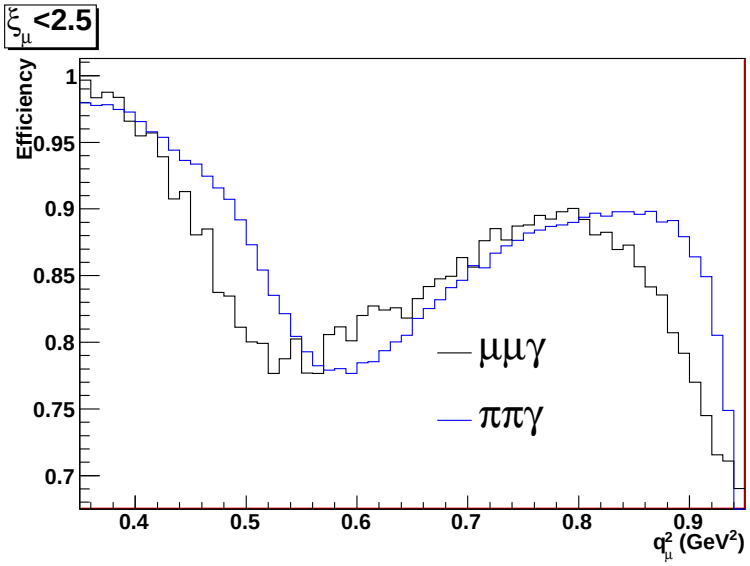

Figure 6.29: Efficiency of the cut $\xi_\mu < 2.5$ for both MC $\mu\mu\gamma$ and MC $\pi\pi\gamma$ as a function of q_μ^2.

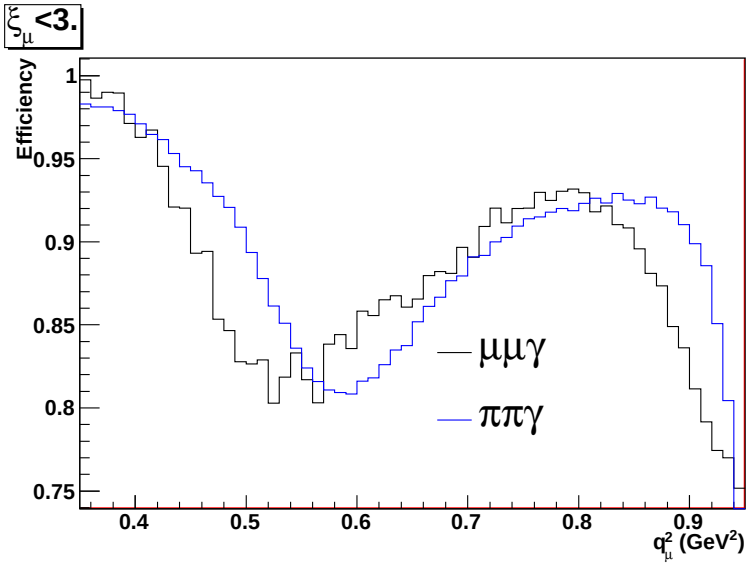

Figure 6.30: Efficiency of the cut $\xi_\mu < 3.$ for both MC $\mu\mu\gamma$ and MC $\pi\pi\gamma$ as a function of q_μ^2.

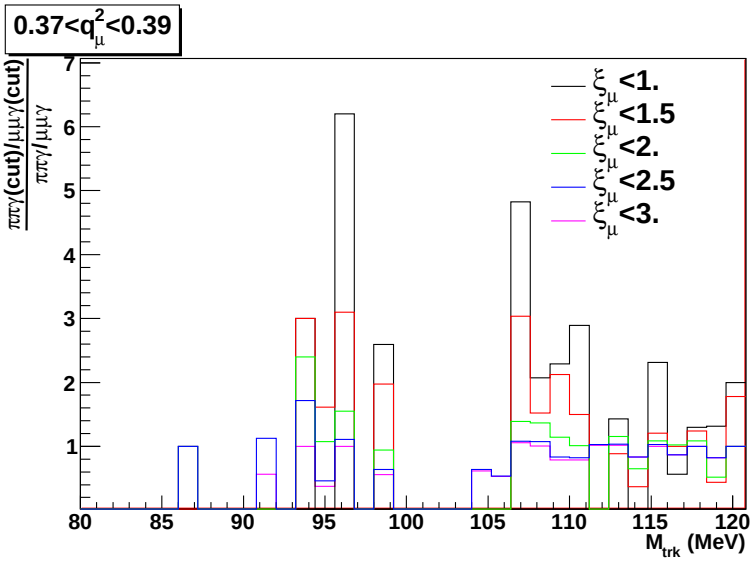

Figure 6.31: $\varepsilon_{\pi\pi\gamma}/\varepsilon_{\mu\mu\gamma}$ for all the applied cuts on ξ_μ for events with $0.37 < q_\mu^2 < 0.39$ in the region $M_{trk} < 120\ MeV$.

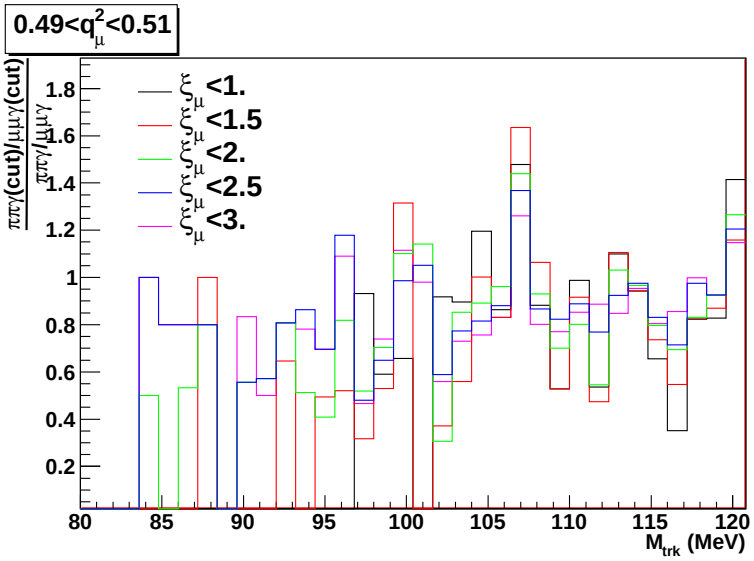

Figure 6.32: $\varepsilon_{\pi\pi\gamma}/\varepsilon_{\mu\mu\gamma}$ for all the applied cuts on ξ_μ for events with $0.49 < q_\mu^2 < 0.51$ in the region $M_{trk} < 120\ MeV$.

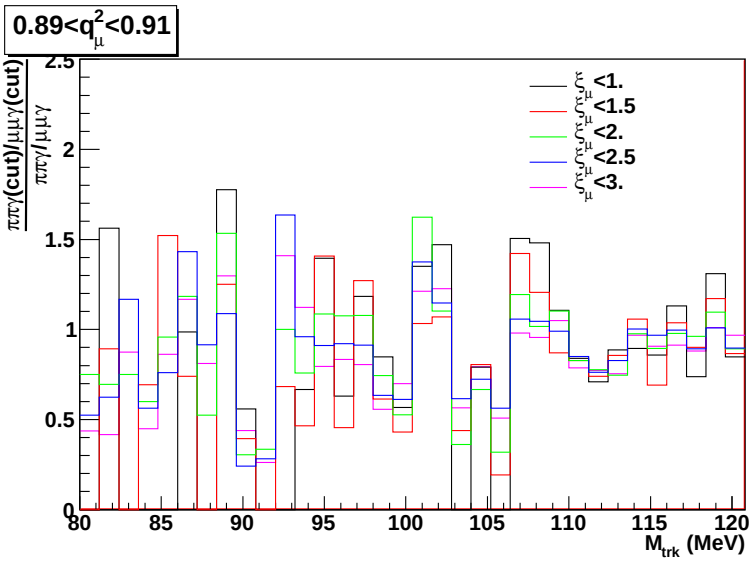

Figure 6.33: $\varepsilon_{\pi\pi\gamma}/\varepsilon_{\mu\mu\gamma}$ for all the applied cuts on ξ_μ for events with $0.89 < q_\mu^2 < 0.91$ in the region $M_{trk} < 120\ MeV$.

6.3.3 $\sigma_{M_{trk}}\left(q_\pi^2\right)$ and $\sigma_{\sigma_{M_{trk}}}\left(q_\pi^2\right)$ from MC $\mu\mu\gamma$

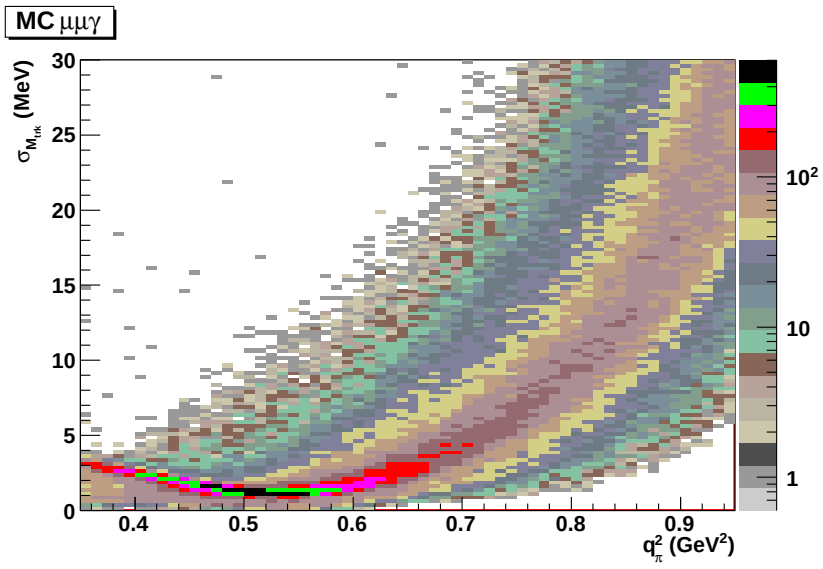

Figure 6.34: $\sigma_{M_{trk}}$ vs q_π^2 of the events for the MC $\mu\mu\gamma$.

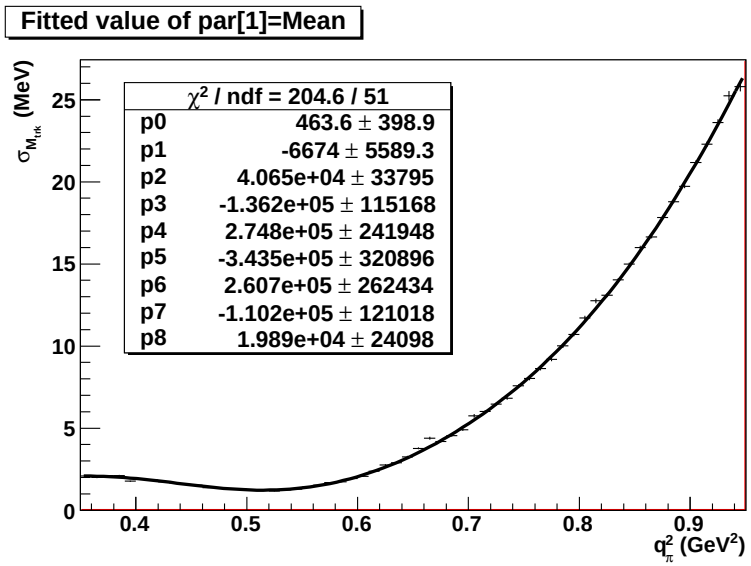

Figure 6.35: $\bar{\sigma}_{M_{trk}}$ as a function of q_π^2 for the MC $\mu\mu\gamma$.

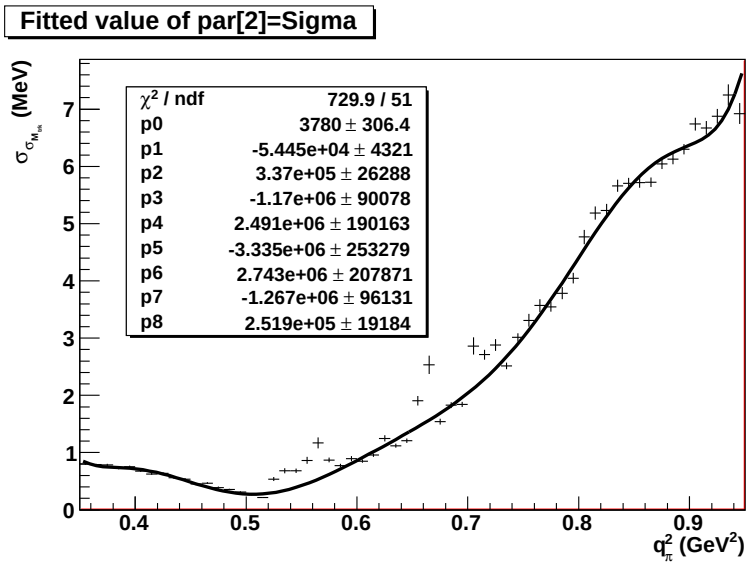

Figure 6.36: $\sigma_{\sigma_{M_{trk}}}$ as a function of the q_π^2 for the MC $\mu\mu\gamma$.

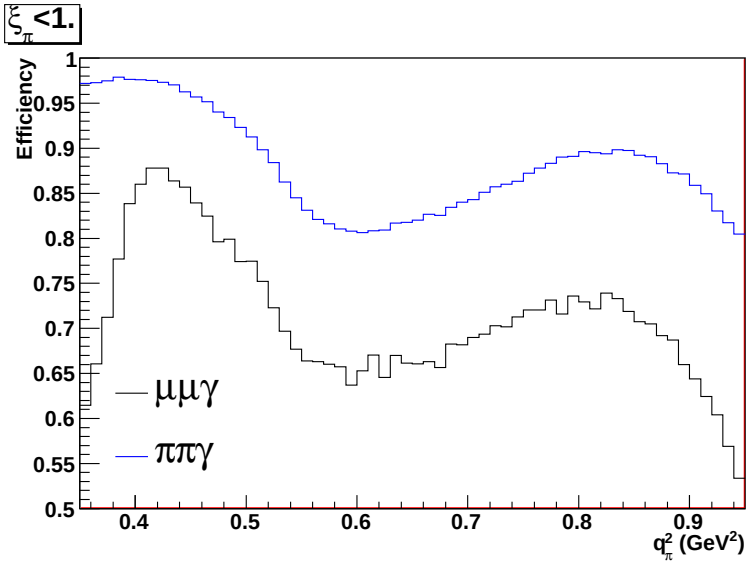

Figure 6.37: Efficiency of the cut $\xi_\pi < 1.$ for both MC $\mu\mu\gamma$ and MC $\pi\pi\gamma$ as a function of q_π^2.

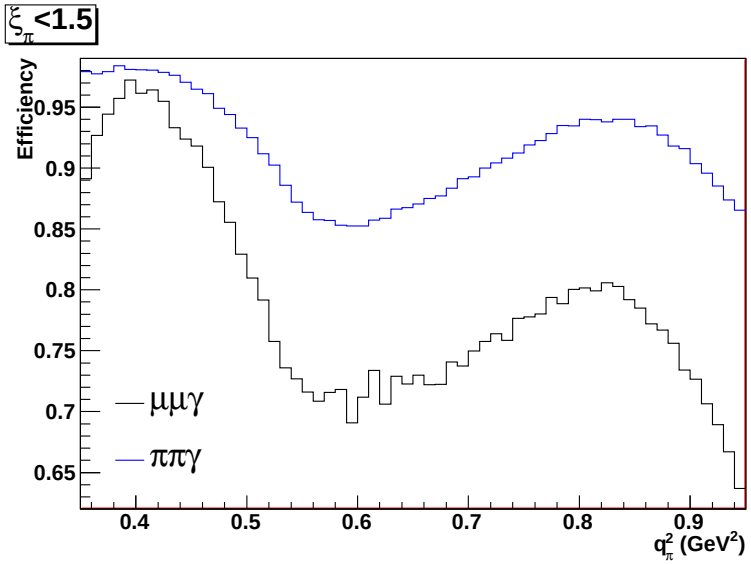

Figure 6.38: Efficiency of the cut $\xi_\pi < 1.5$ for both MC $\mu\mu\gamma$ and MC $\pi\pi\gamma$ as a function of q_π^2.

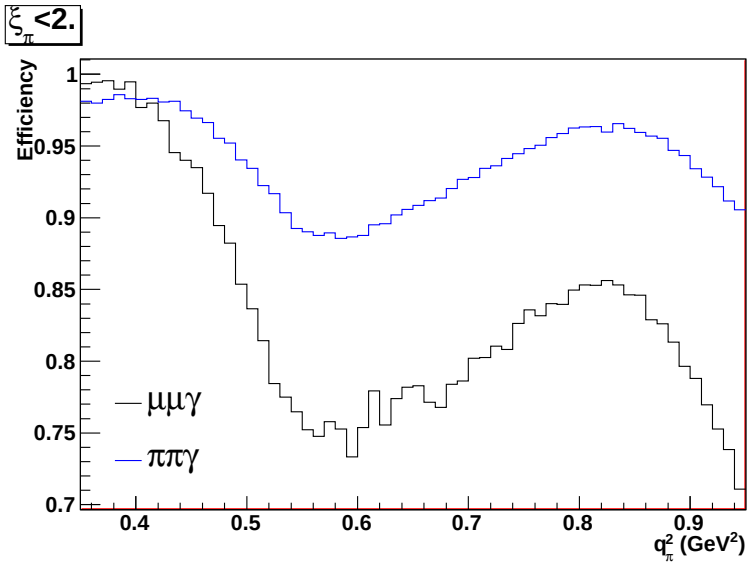

Figure 6.39: Efficiency of the cut $\xi_\pi < 2.$ for both MC $\mu\mu\gamma$ and MC $\pi\pi\gamma$ as a function of q_π^2.

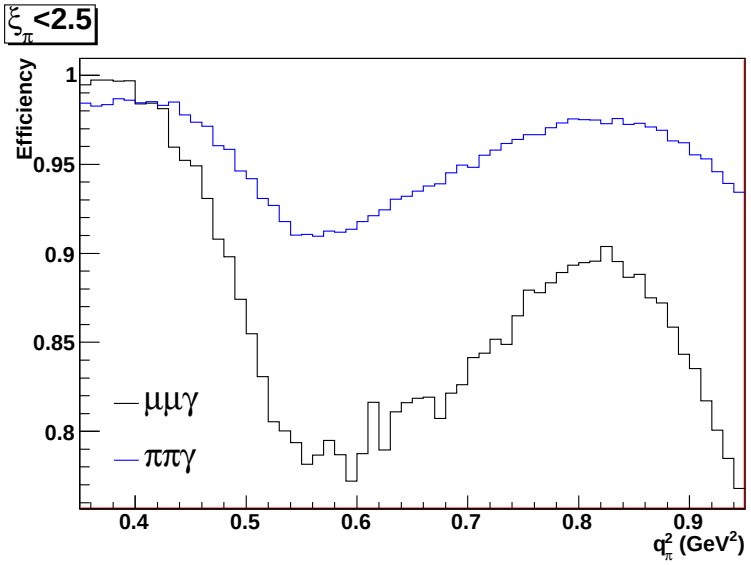

Figure 6.40: Efficiency of the cut $\xi_\pi < 2.5$ for both MC $\mu\mu\gamma$ and MC $\pi\pi\gamma$ as a function of q_π^2.

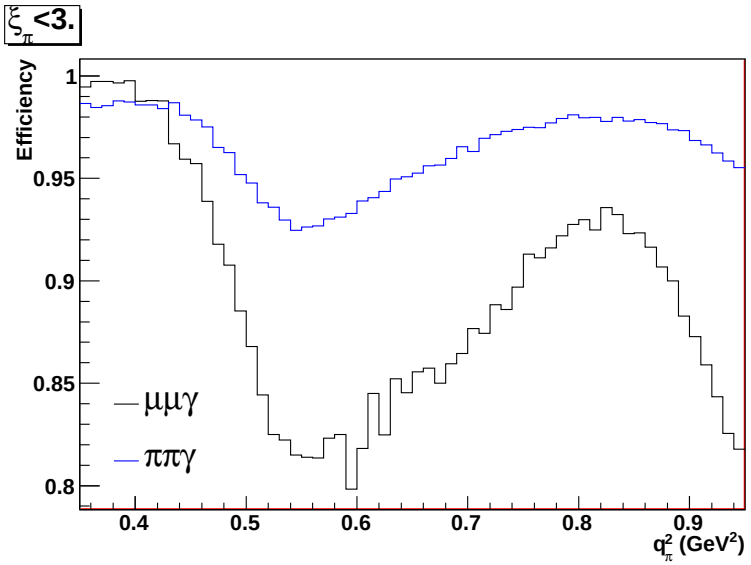

Figure 6.41: Efficiency of the cut $\xi_\pi < 3.$ for both MC $\mu\mu\gamma$ and MC $\pi\pi\gamma$ as a function of q_π^2.

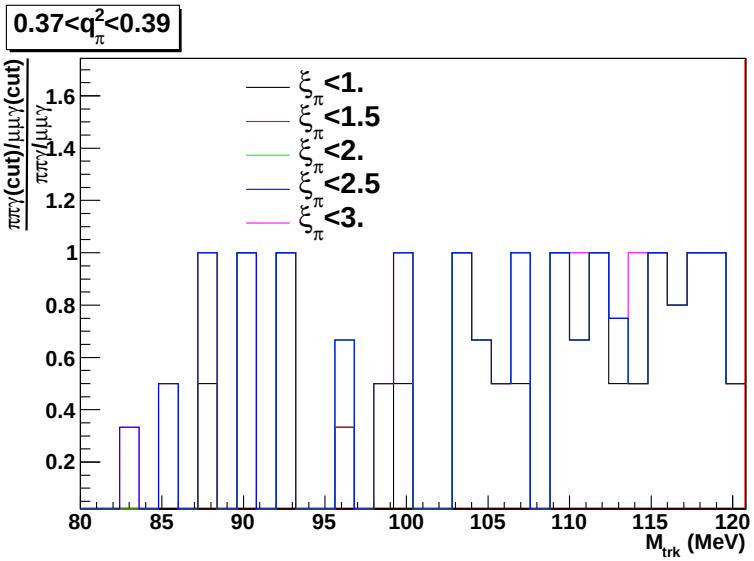

Figure 6.42: $\varepsilon_{\pi\pi\gamma}/\varepsilon_{\mu\mu\gamma}$ for all the applied cuts on ξ_π for events with $0.37 < q_\pi^2 < 0.39$ in the region $M_{trk} < 120\ MeV$.

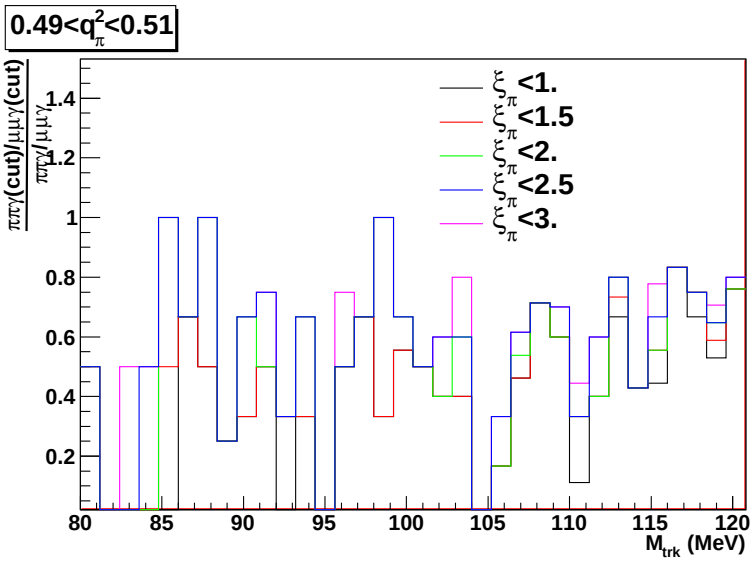

Figure 6.43: $\varepsilon_{\pi\pi\gamma}/\varepsilon_{\mu\mu\gamma}$ for all the applied cuts on ξ_π for events with $0.49 < q_\pi^2 < 0.51$ in the region $M_{trk} < 120\ MeV$.

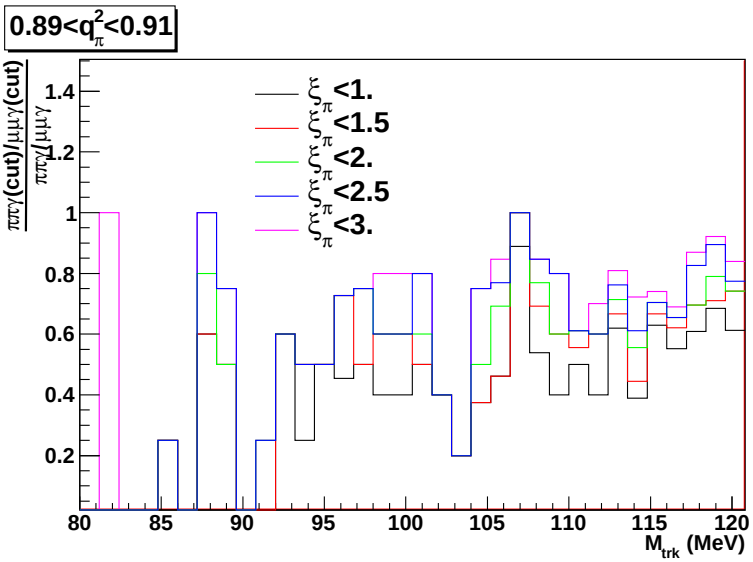

Figure 6.44: $\varepsilon_{\pi\pi\gamma}/\varepsilon_{\mu\mu\gamma}$ for all the applied cuts on ξ_π for events with $0.89 < q_\pi^2 < 0.91$ in the region $M_{trk} < 120\ MeV$.

6.3.4 $\sigma_{M_{trk}}\left(q_\mu^2\right)$ and $\sigma_{\sigma_{M_{trk}}}\left(q_\mu^2\right)$ from MC $\mu\mu\gamma$

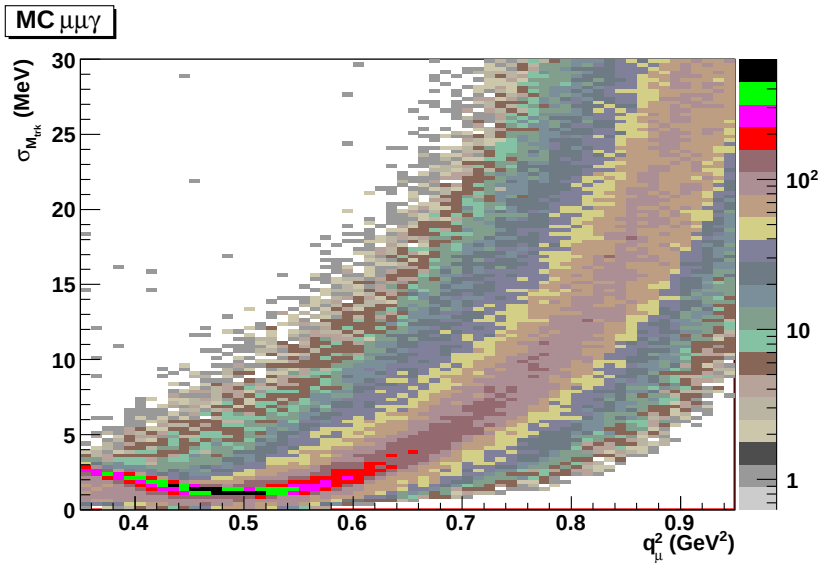

Figure 6.45: $\sigma_{M_{trk}}$ vs q_μ^2 of the events for the MC $\mu\mu\gamma$.

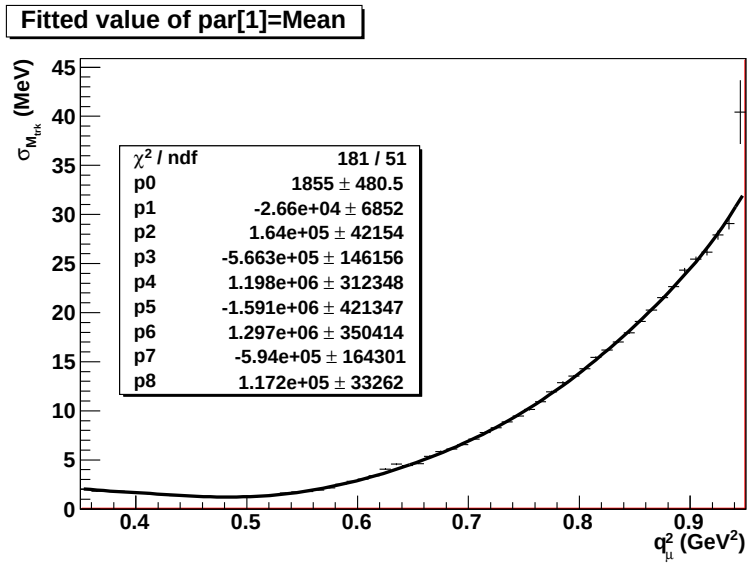

Figure 6.46: $\bar{\sigma}_{M_{trk}}$ as a function of q_μ^2 for the MC $\mu\mu\gamma$.

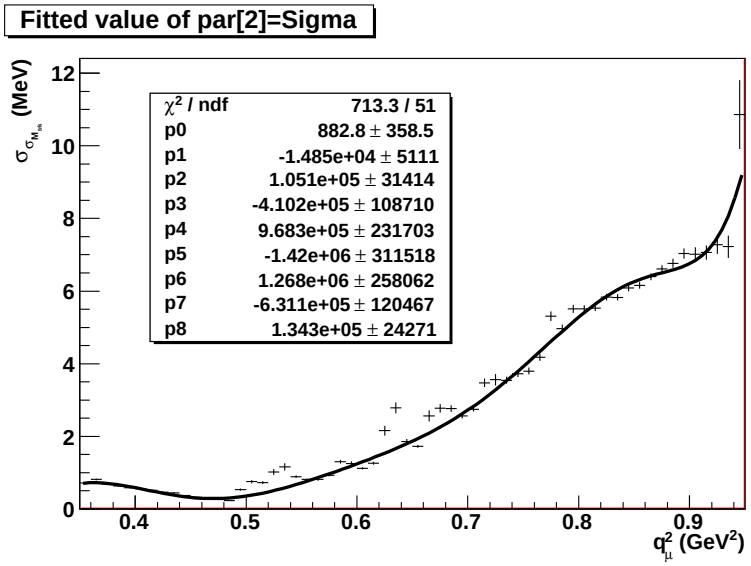

Figure 6.47: $\sigma_{\sigma_{M_{trk}}}$ as a function of the q_μ^2 for the MC $\mu\mu\gamma$.

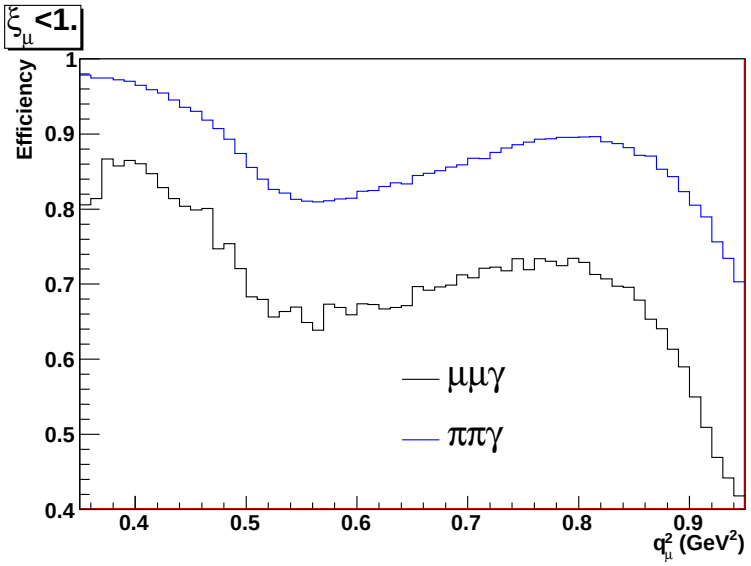

Figure 6.48: Efficiency of the cut $\xi_\mu < 1.$ for both MC $\mu\mu\gamma$ and MC $\pi\pi\gamma$ as a function of q_μ^2.

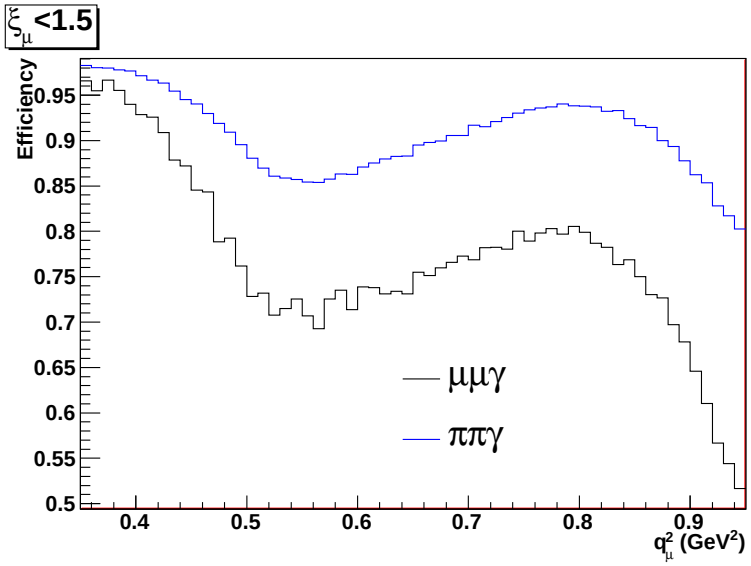

Figure 6.49: Efficiency of the cut $\xi_\mu < 1.5$ for both MC $\mu\mu\gamma$ and MC $\pi\pi\gamma$ as a function of q_μ^2.

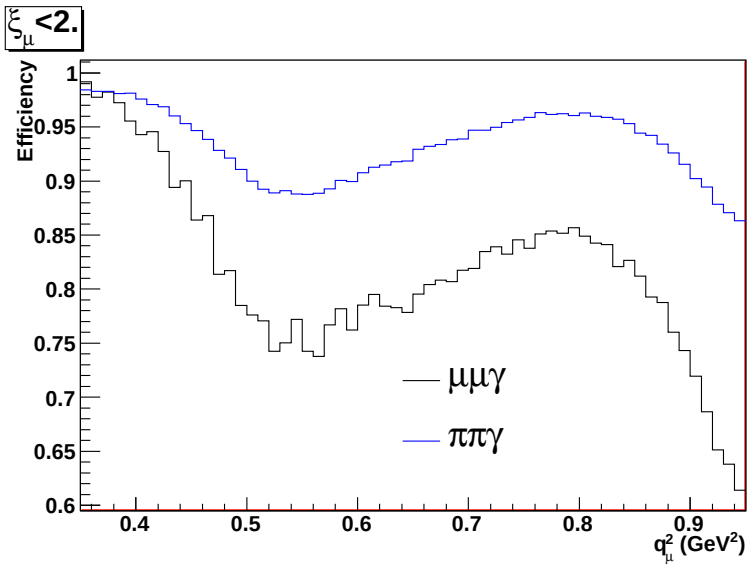

Figure 6.50: Efficiency of the cut $\xi_\mu < 2.$ for both MC $\mu\mu\gamma$ and MC $\pi\pi\gamma$ as a function of q_μ^2.

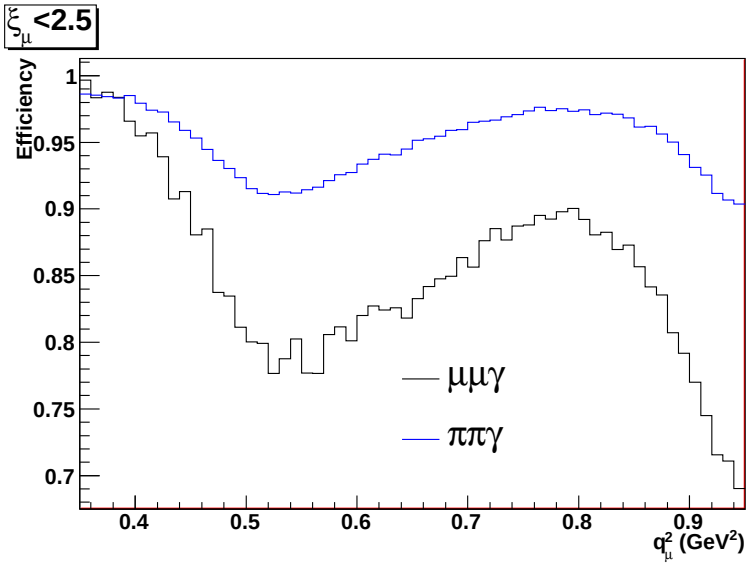

Figure 6.51: Efficiency of the cut $\xi_\mu < 2.5$ for both MC $\mu\mu\gamma$ and MC $\pi\pi\gamma$ as a function of q_μ^2.

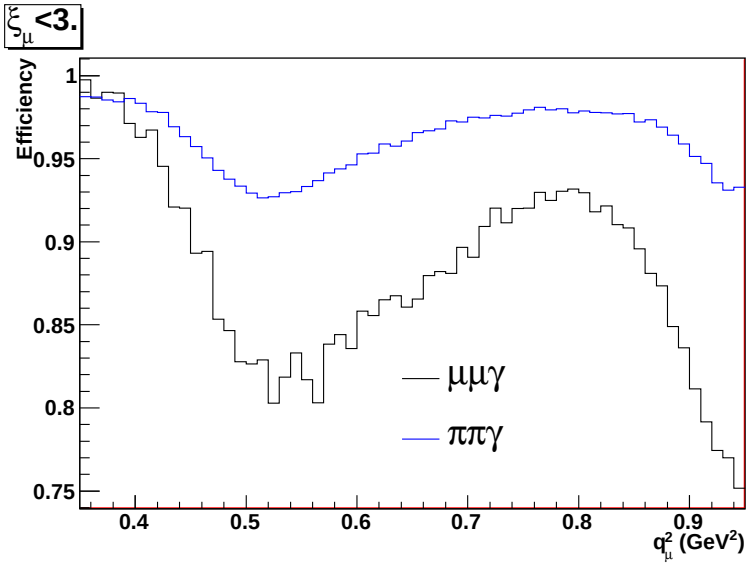

Figure 6.52: Efficiency of the cut $\xi_\mu < 3.$ for both MC $\mu\mu\gamma$ and MC $\pi\pi\gamma$ as a function of q_μ^2.

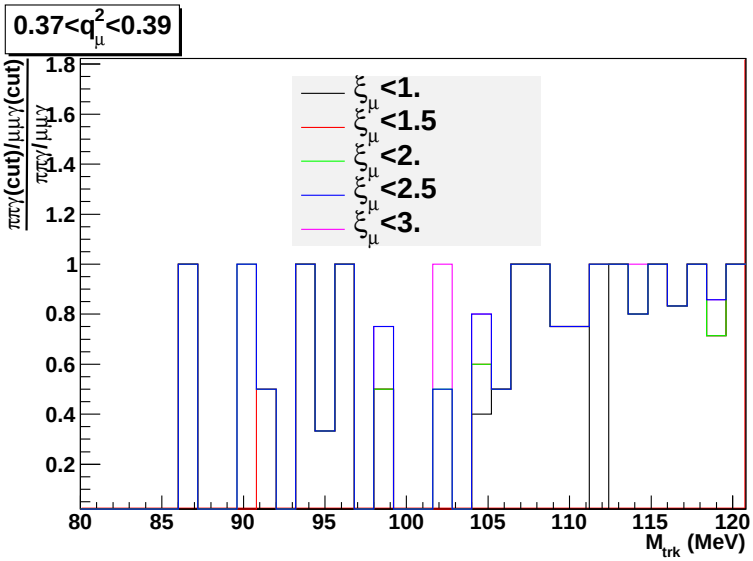

Figure 6.53: $\varepsilon_{\pi\pi\gamma}/\varepsilon_{\mu\mu\gamma}$ for all the applied cuts on ξ_μ for events with $0.37 < q_\mu^2 < 0.39$ in the region $M_{trk} < 120\ MeV$.

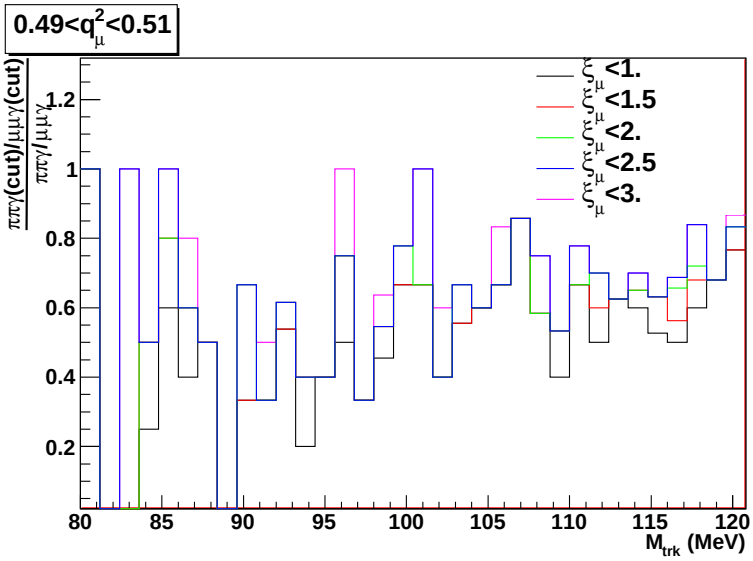

Figure 6.54: $\varepsilon_{\pi\pi\gamma}/\varepsilon_{\mu\mu\gamma}$ for all the applied cuts on ξ_μ for events with $0.49 < q_\mu^2 < 0.51$ in the region $M_{trk} < 120\ MeV$.

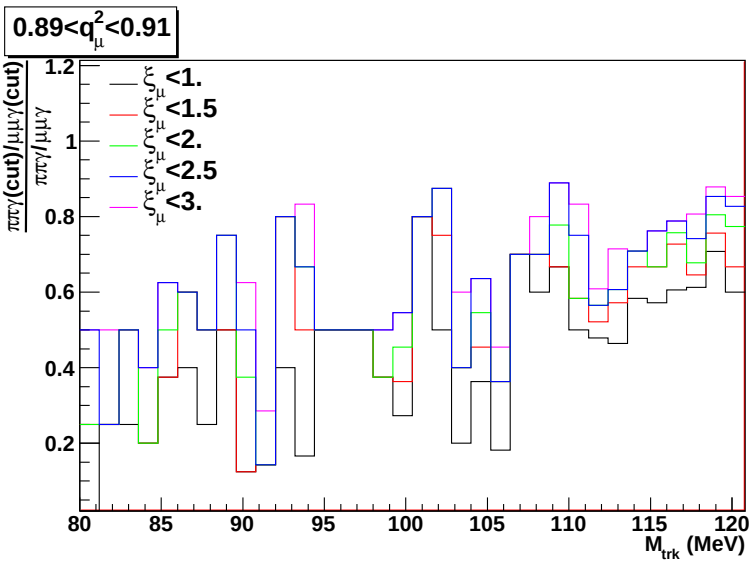

Figure 6.55: $\varepsilon_{\pi\pi\gamma}/\varepsilon_{\mu\mu\gamma}$ for all the applied cuts on ξ_μ for events with $0.89 < q_\mu^2 < 0.91$ in the region $M_{trk} < 120\ MeV$.

6.3.5 Conclusions

From the analysis of the selection efficiency and the rejection power, the best cut was chosen to be $\xi_\mu < 2.5$ as a function of q_μ^2 computed from the MC $\mu\mu\gamma$. The cut has been studied to be very effective and it will be implemented in the final selection of $\mu\mu\gamma$ sample, which is currently on going.

Chapter 7

Conclusions

This work is related to the study of the Inner Tracker for the KLOE-2 experiment and the data analysis with the KLOE experiment.
The Inner Tracker module-0 was intensively tested with cosmic rays, X-rays and 10 GeV pion beam at CERN test facility (2008). Many results have been achieved: the gain measurements as a function of the gas gaps electric field to set the working point of the chamber, the validation of the cylindrical GEM construction method, the measured spatial resolution ($\sim 200\ \mu m$ at $|\vec{B}| = 0\ T$) matches the KLOE-2 design requirements that improve the decay vertex reconstruction capability, the track momentum resolution and the geometrical acceptance for low momentum tracks. The behaviour of a planar triple GEM equipped with the final IT readout ($X - V$) was studied in magnetic field at CERN test beam facility (2009). The results suggest that at the value of the KLOE magnetic field ($|\vec{B}| = 0.5\ T$) the drop of the detection efficiency is negligible and the spatial resolution is $\sim 250\ \mu m$. Moreover, the distance (Δx) between the hitted strips and the impact point of the incoming particle, was measured for different values of $|\vec{B}|$ field and at $0.5\ T$ (KLOE-2) we found $\Delta x \sim 900\ \mu m$. The displacement of the reconstructed impact point is due to the Lorentz strength that acts orthogonal to the plane formed by the electric field and the magnetic one on the electrons produced in the gas ionization process.
For what concerns the data analysis, the work is focused on the selection of a pure $\mu\mu\gamma$ sample where the photon is emitted by the electron (positron) at small polar angle ($\theta_\gamma < 15°$). The study is devoted to search for the signature of the light boson (U) belonging to a secluded gauge sector. The particle identification criteria is based on the so called variable *trackmass*. To determine the selection power for pions, a dedicated study has been performed on the 3π sample. A cut on the trackmass statistical uncertainty ($\sigma_{M_{trk}}$), related to the charged tracks momenta covariance matrix, has been applied

and the efficiency is $\sim 96\%$. The same cut has been applied to the sample made of two charged tracks with opposite charge and no cluster prompt, and it rejects about 70% of the events. Since this selection criteria holds a not acceptable pions contamination into the $\mu\mu\gamma$ sample, a set of new cuts has been studied. The correlation between the $\sigma_{M_{trk}}$ and the invariant mass of the two charged tracks (q_x^2) allows to apply a cut on the $\sigma_{M_{trk}}$ variance as a function of the q_x^2. The best compromise has been provided by the $\sigma_{M_{trk}}$ vs q_μ^2 correlation computed from the MC $\mu\mu\gamma$ sample and it corresponds to the following cut: $\frac{\sigma_{M_{trk}}\left(q_\mu^2\right)-\bar{\sigma}_{M_{trk}}\left(q_\mu^2\right)}{\sigma_{\sigma_{M_{trk}}}\left(q_\mu^2\right)} < 2.5$. This selection significantly improves the rejection power of the background events ($\pi\pi\gamma$).

Appendix A

GARFIELD

GARFIELD is a program for detailed simulations of two-dimensional drift chambers consisting of thin wires and infinite equipotential planes. The input to the program is divided in sections, that should be written with a specific order: for instance the cell and the gas sections must be appear before the sections using their data. Some routines can be called everywhere and more than once: they are the *Call procedures*.
The geometry of the cell is defined in the &CELL section. GARFIELD provides some tools to build an elementary cell of the detector to be simulated. The use of these tools has been recently improved with the introduction of the neBEM environment. For more complicated cells, GARFIELD can read the outputs of programs like Ansys, Maxwell or Tosca.
The &GAS section interfaces two programs: MAGBOLTZ and MIX. The first was written by S. Biagi, while the second uses traditional Schultz-Gresser approach with less functionality than MAGBOLTZ. The gas mixture can be easily defined listing the components (with their fractions) and setting the temperature and the pressure. In this section can be called the programs that simulate primary ionization in the defined gas mixture: HEED or SRIM. The first must be called if in the following section the HEED model is required for the primary ionisation; it is written by I. Smirnov and it simulates the energy loss through ionisation of a particle that traverses the gas. SRIM computes the stopping of ions by matter.
The &DRIFT section is part of the program devoted to displaying the behaviour of the electrons and ions in the chamber. A volume of the chamber must be defined, where the GARFIELD will simulate the desired processes. In this section should be called the procedures related to the electron drift:

- *Call drift_electron* (*Call drift_electron_3*): it uses the Runge-Kutta-Fehlberg integration method. This procedure computes an electron

drift line in a 2-D (3-D) cell. It needs the coordinates of the starting point of the electron

- *Call drift_MC_electron*: it performs a Monte-Carlo simulation of an electron drift line, taking diffusion into account on a step-by-step basis. The step should be previously defined. It requires the coordinates of the starting point of the electron

- *Call drift_microscopic_electron*: it mades a microscopic simulation of the movement of an electron through the gas. This is a more detatiled simulation and it requires many parameters to be defined: the step of the integration, the maximum of the kinetic energy of the electron (provided by MAGBOTLZ), the kinetic energy of the starting electron, the direction of the velocity of the electron. This routine provides a very detailed simulation.

Bibliography

[1] *Measurement of the K_L meson lifetime with the $K_L \to \pi^0\pi^0\pi^0$*, S. Bocchetta, PhD Thesis.

[2] *Handbook on neutral kaon interferometry at a $\phi-$factory*, A. Di Domenico ed., Frascati Physics Series **43**, INFN-LNF, Frascati, 2007.

[3] *PDG*, Particle Data Group 2006

[4] *Precision Kaon and Hadron Physics with KLOE*, F. Bossi et al., Rivista del Nuovo Cimento, vol. **31**, n° 10

[5] *Novel type of CPT violation for correlated Einstein-Podolsky-Rosen states of neutral mesons*, J. Bernabeu et al., Phys. Rev. Lett. **92** (2004) 131601

[6] *Intrinsic CPT violation and decoherence for entangled neutral mesons*, J. Bernabeu et al., Nucl. Phys. B **744** (2006) 180

[7] *Physics with the KLOE-2 experiment at the upgraded DAΦNE*, G. Amellino-Camelia, G. Morello et al., submitted to EPJ, arXiv:1003.3868v1

[8] *Early SPI/INTEGRAL measurements of the 511 keV line emission from the 4^{th} quadrant of the Galaxy*, P. Jean et al. Astron. Astrophys. **407**, L55 (2003)

[9] *Observation of an anomalous positron abundance in the cosmic radiation*, O. Adriani et al., Nature, **458**, 607 (2009)

[10] *Production and propagation of cosmic-ray positrons and electrons*, Astrophys. J. **493**, 694-707 (1998)

[11] *Probing dark forces and light hidden sectors at low-energy e^+e^- colliders*, R. Essig et al., Phys. Rev. **D80** 015003 (2009)

[12] *Probing a secluded $U(1)$ at B factories*, B: Batell et al., Phys. Rev. **D79** 115008 (2009)

[13] *Searching for the light dark gauge boson in GeV-scale experiments*, M. Reece, L.T. Wang, JHEP **07**, 051 (2009)

[14] *Introduction to elementary particles*, D. Griffiths, John Wiley and Sons, Ed. 1987

[15] *Quarks and leptons: an introductory course in modern particle physics*, F. Halzen, A. Martin, John Wiley and Sons, Ed. 1984

[16] *The tracking detector of the KLOE experiment*, A. Adinolfi et al., Nuclear Instrum. Methods, **A 488** (2002)

[17] *The KLOE electromagnetic calorimeter*, A. Adinolfi et al., Nuclear Instrum. Methids, **A 482** (2002)

[18] *The trigger system of the KLOE experiment*, A. Adinolfi et al., Nuclear Inrtum. Methods, **A 492** (2002)

[19] *The Low Energy Tagger for the KLOE-2 experiment*, D. Babusci et al., Proceeding of the 11^{th} ICATPP Conference on Astroparticle, Particle, Space Physics, Detectors and Medical Physics Applications, World Scientific

[20] *The High Energy Tagger for the $\gamma\gamma$ physics at KLOE-2*, F. Archilli et al., Proceeding of the 11^{th} ICATPP Conference on Astroparticle, Particle, Space Physics, Detectors and Medical Physics Applications, World Scientific

[21] *Technical Design Report of the Inner Tracker for the KLOE-2 experiment*, KLOE Collaboration, LNF-10/3(P) 2010

[22] *Measurement of the branching ratio and search for a CP violating asymmetry in the $\eta \to \pi^+\pi^-e^+e^-$ decay KLOE*, KLOE coll., Phys. Lett. B **675** (2009) 283

[23] *Micro-pattern gaseous detectors*, L. Shektmann, Nuclear Instrum. Methods **A 494** (2002) 128

[24] *Charge amplification and transfer processes in the gas electron multiplier*, S. Bachmann et al., Nuclear Instrum. Methods, **A 438** (1999) 376.

[25] *Development of the Gas Electron Multiplier (GEM)*, J. Benlloch et al., CERN-PPE/97-146 (1997)

[26] *Further development of the Gas Electron Multiplier (GEM)*, J. Benlloch et al. CERN-EP/98-50 (1998)

[27] *Particle Detection with Drift Chambers*, W.Blum, W. Riegler, L. Rolandi, Springer, Ed. 2008.

[28] *GEM: A new concept for electron amplification in gas detectors*, F. Sauli, Nuclear Instrum. Methods, **A 386** (1997), 531.

[29] *Triple-GEM detectors for the innermost region of the muon apparatus at the LHCb experiment*, M. Poli Lener, PhD thesis.

[30] *Studio e sviluppo di un rivelatore a GEM per la zona centrale delle camere per muoni di LHCb*, M. Alfonsi, Diploma thesis, Univ. La Spienza, Rome, 2002/2003

[31] *Principle of operation of multiwire proportional and drift chamber*, F. Sauli, Yellow Report, CERN 77-09, 1977

[32] *Currents induced in electron motion*, S. Ramo, Proc. IRE 27 (1934) 584

[33] *Progress on large area GEMs*, S. Duarte Pinto et al., arXiv :0909.5039v2

[34] *An ultra-light cylindrical GEM detector as inner tracker at KLOE-2*, G. Bencivenni, D. Domenici, Nuclear Instrum. Methods **A 581** (2007), 221

[35] *A novel idea for an ultra-light cylindrical GEM based vertex detector*, G. Bencivenni et al., Nuclear Instrum. Methods **A 572** (2007), 168

[36] *The full scale prototype of the cylindrical-GEM detector as inner tracker in KLOE2*, G. Bencivenni et al., NSS Conference Record 2007 IEEE

[37] *Performance of the cylindrical GEM prototype for the KLOE-2 Inner Tracker*, G. Bencivenni et al., NSS Conference Record 2008 IEEE

[38] *Status of the cylindrical-GEM project for the KLOE-2 Inner Tracker*, G. Bencivenni et al., NSS Conference Record 2009 IEEE

[39] *http://consult.cern.ch/writeup/garfield/help/* R. Veenohf

[40] *http://consult.cern.ch/writeup/magboltz/* S. Biagi

[41] *http://consult.cern.ch/writeup/heed/* I. Smirnov

[42] *Status of the cylindrical-GEM project for the KLOE-2 Inner Tracker* D. Domenici et al., submitted to Nuclear Instrum. Methods

[43] *Activity of CERN and LNF groups on Large Area GEM Detectors* M. Alfonsi et al., Nuclear Instrum. Methods **A 617** (2010) 151

[44] *Status of the cylindrical-GEM project for the KLOE-2 Inner Tracker* E. De Lucia et al., http://dx.doi.org/10.1016/j.nima.2010.06.315

[45] *Determination of* $\sigma\left(e^+e^- \to \pi^+\pi^-\right)$ *from radiative processes at DA*Φ*NE*, KLOE coll., KLOE note n° 189

[46] *The Event Classification procedures*, F. Ambrosino et al., KLOE memo n° 225

[47] *Event Classification of non-k* ϕ *decays*, KLOE memo n° 171

[48] *Modification to the PPGTAG event classification routine*, S. Mueller, G. Venanzoni, KLOE memo n° 305

[49] *A particle identification method for pion-electron discrimination*, B. Valeriani, KLOE memo n° 295

[50] *Analysis of the dynamics of the decay* $\phi \to \pi^+\pi^-\pi^0$, C. Bini, KLOE memo n° 274

[51] *Probabilità Statistica e Simulazione*, A. Rotondi, P. Pedroni, A. Pievatolo, Springer Verlag, ED. 2005

[52] *Measurement of the* $\sigma\left(e^+e^- \to \pi^+\pi^-\gamma(\gamma)\right)$ *using initial state radiation and extraction of* $a_\mu^{\pi\pi}$ *between* 0.35 *and* 0.95 GeV^2 *with the KLOE experiment (small angle analysis)*, P. Beltrame et al., KLOE memo n° 349

Acknoledgements

My dear friends,
it's time to leave and to find my way far from here and from you. I want to sincerely thank you since: you helped me when I was in trouble, you made me laugh when I was sad, you made me understand my mistakes when I was wrong (quite often), you listened to me when I complained (again, quite often), you shared your special moments with me and you gave me the right suggestions when I needed them. I will always keep you in my heart and in my mind, remembering these years
when I always had my family by my side (my parents, Tommaso, Miyuki, Eleonora, Ilenia, my grandparents),
when I found many examples to imitate (Marco, Gianni, Graziano, Antonio, Daniela, Evelin, etc.) although I didn't do it,
when I met many nice colleagues and friends in Cosenza (Sandro, Beatrice, Denise, Giuseppe, Francesco, Vincenzo, Gabriele, Melissa, Domenica, etc.),
when I met many nice colleagues and friends in Frascati (Danilo, Erika, Salvatore, Antonio, Flavio, JJ, Marek, Jing, Marco, Federico, etc.),
when I had to say goodbye to a friend leaving to Lund (Simona) and to another leaving to Paris (Sara),
when I saw some friends of mine getting married (Angelica, Teresa, Concetta),
when I lost others because they work far from me (Angela, Gerarda, Vicky),
when I laughed with nice guys (Pasquale, Pasquale, Pasquale, Pasquale (it's not a mistake, they come from the same town), Cristina, Stefano, Assunta, Maria, Fabio, Alessandra, Francesca, Valeria, Laura, Vanessa),
when I dreamt of a smile from Rosanna, Maya and other girls already cited,
when I met new friends (Monica, Alessandra, Oscar, Giulia, Vladimir)
and when I asked myself why I was lucky enough to have you by my side.

I would like to thank all the people I cited and all the people I forgot to cite although they shared a part of their life with me. Thank you so much and don't worry: a day will come when your efforts to let me be a better person will achieve the goal.
Farewell, my dear.

Gianfranco